TECHNICAL PHYSICS LETTERS VOLUME 25, NUMBER 3 MARCH 1999

Limitation of a giant amplification surge by photoinduced space charge accompanying an increase in the concentration of recombination centers in intrinsic threshold photoresistors with extracting contacts

V. A. Kholodnov and A. A. Drugova

State Scientific Center of the Russian Federation, State Enterprise NPO ''Orion,'' Moscow

(Submitted August 10, 1998)
Pis'ma Zh. Tekh. Fiz. **25**, 1–8 (March 12, 1999)

An analysis is made of the dependence of $\hat{G}$ on V under conditions of a giant surge of the photoelectric gain G as the concentration of recombination impurities N increases, where V is the applied voltage and $\hat{G}$ is the value of G at the maximum point of the function $G(N)$. It is shown that as a result of the space charge induced by the optical radiation the function $\hat{G}(V)$ exhibits strongly nonmonotonic behavior. The optimum voltage V_{opt} applied to the sample is determined for which $\hat{G}(V)$ reaches the maximum $\hat{G}_{\max}$. This nonmonotonic dependence of $\hat{G}$ on V does not correlate with heating of carriers or the lattice or by injection of charge from the contacts. © *1999 American Institute of Physics.* [S1063-7850(99)00103-2]

In papers[1] at an international symposium (USA) we reported that by increasing the concentration N of recombination impurities, saturation of the photoelectric gain G with increasing electric field V can be avoided[2–6] in intrinsic threshold photoresistors with impurity recombination of photocarriers[7–12] and extracting contacts (at these contacts the concentrations of nonequilibrium electrons Δn and holes Δp are zero[2–6]). We then put forward a better argued justification for this possibility.[13]

This suppression of the saturation of $G(V)$ is based on a giant surge[14] in the value of $G \equiv I_{\text{ph}}/(qWg)$ (Ref. 10) as N increases (Fig. 1a), where I_{ph} and g are the photocurrent densities and the rates of carrier photogeneration, W is the distance between the contacts ($x=0$ and $x=W$, inset to Fig. 1a), and q is the electron charge. This effect occurs first because the lifetimes of the nonequilibrium electrons τ_n and holes τ_p increase rapidly as the concentration N increases in a certain range[15–17] (Fig. 1c), if

$$\xi_1 \equiv \frac{3}{\theta B} \ll 1, \quad \xi_2 \equiv \frac{4B}{A^2} \ll 1,$$

$$\xi_3 \equiv \frac{1}{\sqrt{A}} \ll 1, \quad \xi_4 \equiv \frac{1}{2}\sqrt{\xi_2} \ll 1. \tag{1}$$

Here

$$A = 2\frac{N_D}{n_t}, \quad B = 4\frac{p_t}{n_t}, \quad \theta = \frac{w_p}{w_n}, \tag{2}$$

where w_n and w_p are the probabilities of electron and hole capture by a deep level and n_t and p_t are their equilibrium concentrations when the energies of the Fermi level and the recombination level are the same. In Refs. 13–17 we used a model consisting of shallow, completely ionized donors having the concentration N_D together with neutral and minus-one charged deep acceptors[9,18,21] where the semiconductor parameters deviate slightly from the equilibrium values (for example, in threshold photoresistors[2–6]). We also assumed that the spin degeneracy factor of the acceptor state is 1/2 (Refs. 19–22). In the present paper we use the same model.

An increase in the lifetimes τ_n and τ_p with increasing N is caused by weakly nonequilibrium filling of a recombination level, as a result of which the lifetimes are determined not only by capture of nonequilibrium carriers at equilibrium traps but also by thermal ejection of electrons and holes from nonequilibrium centers, converting them from a bound to a free state, and by the capture of equilibrium carriers at nonequilibrium traps. For this reason the lifetimes of nonequilibrium carriers may be either longer or shorter than their times of capture at equilibrium traps and may be highly nonmonotonic functions of the concentration of recombination centers N (Refs. 15–17) (Fig. 1c). Note that $\tau_n(N)$ and $\tau_p(N)$ may also be highly nonmonotonic functions for two-level recombination impurities, as was shown in Refs. 23 and 24, and also in the presence of auxiliary (phonon) carrier trapping centers.

Another factor causing a gain surge is that when the conditions (1) are satisfied, the ambipolar mobility μ vanishes for a certain value of N which, to lowest order in the small parameters (1), is the same as $N = N_D$ for which the functions $\tau_n(N)$ and $\tau_p(N)$ reach the maximum values $\hat{\tau}_n$ and $\hat{\tau}_p$ (Refs. 13–17) (Figs. 1b and 1c), where[16,17]

$$\hat{\tau}_n = \frac{\sqrt{A+B}}{2w_nN_D}, \quad \hat{\tau}_p = \frac{2A + \theta B\sqrt{A+B}}{2w_pN_D(A+B)}. \tag{3}$$

Under these conditions μ vanishes in an n-type material[14] but not for an intrinsic carrier concentration n_i (Refs. 3,6–8, 21, and 25). Physically this is because of the positive sign of the photoperturbation bound at a deep charge impurity ($N_- - N_-^e < 0$, where N is the concentration of recombination centers of charge minus-one and N_-^e is its equilibrium value).

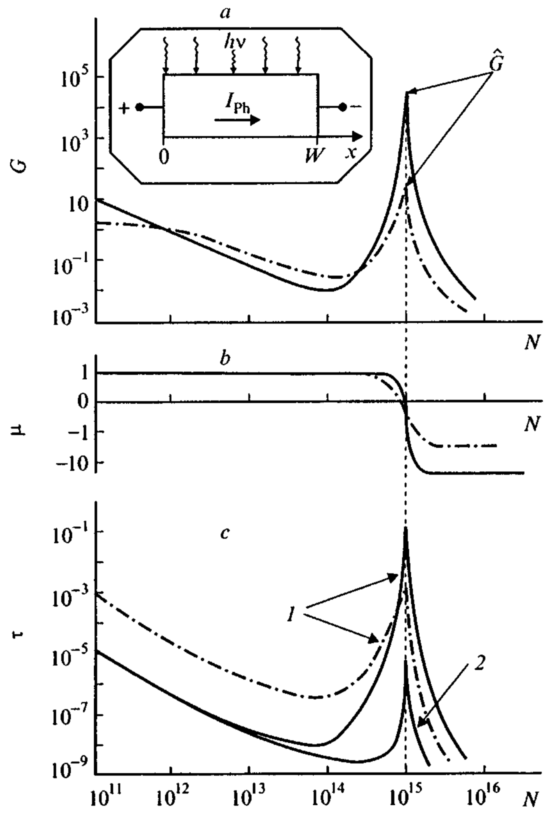

FIG. 1. Photoelectric gain $G\equiv I_{\mathrm{ph}}/qgW$ in GaAs (solid curve) and Si (dot-dash curve) (a), the ambipolar mobility μ in units of the hole mobility μ_p (b), and the electron τ_n (*1*) and hole lifetimes τ_p (*2*) in seconds (c) plotted as functions of the concentration of recombination centers N per cubic centimeter at room temperature. The following parameters are assumed: intrinsic concentration of free carriers $n_i=1.79\times10^6\,\mathrm{cm}^{-3}$, electron mobility $\mu_n=8500\,\mathrm{cm}^2/\mathrm{V}\cdot\mathrm{s}$, $\mu_p=400\,\mathrm{cm}^2/\mathrm{V}\cdot\mathrm{s}$, dielectric constant $\varepsilon=13.1$ (in GaAs from Ref. 26); $n_i=1.45\times10^{10}\,\mathrm{cm}^{-3}$, $\mu_n=1500\,\mathrm{cm}^2/\mathrm{V}\cdot\mathrm{s}$, $\mu_p=450\,\mathrm{cm}^2/\mathrm{V}\cdot\mathrm{s}$, $\varepsilon=11.9$ (in Si from Ref. 26); the ratio of the probability of hole capture to the probability of electron capture is $\theta=w_p/w_n=10^2$, $w_n=10^{-8}\,\mathrm{cm}^3/\mathrm{s}$ (Refs. 9 and 21), $n_i/n_t=10^4$, $N_D=10^{15}\,\mathrm{cm}^{-3}$, $W=10^{-1}$, cm, and $E_0=10$ V/cm. The inset shows the photoresistor circuit.

The result of Ref. 13 was obtained in the quasilinear approximation normally used for moderate fields when divΔE is neglected in the Poisson equation[2–4,7–12,18–22]

$$\mathrm{div}\,\Delta E+\frac{4\pi q}{\varepsilon}(\Delta n+N_- - N_-^e-\Delta p)=0 \qquad (4)$$

where ΔE is the deviation of the electric field from its value E_0 in the absence of illumination, caused by the absorption of radiation, and ε is the dielectric constant. However, even for moderate fields ($E_0\simeq 1$–10 V/cm) the quasilinear approximation is by no means always permissible, as was shown in Ref. 14. The possible inaccuracy of this approximation was also noted in Ref. 13.

Using Refs. 13–17 we can derive the following expression:

$$\hat G=\left\{1-2\frac{\hat L_{\mathrm{eff}}}{W}\tanh\left(\frac{W}{2\hat L_{\mathrm{eff}}}\right)\right\}(\mu_n\hat\tau_n+\mu_p\hat\tau_p)\frac{E_0}{W}. \qquad (5)$$

This determines the value of G at the maximum of the dependence $G(N)$ for uniform photogeneration (Fig. 1a) allowing for the term divΔE in the Poisson equation (4). Here μ_n and μ_p are the mobilities of the electrons and holes, $\hat L_{\mathrm{eff}}=(\hat L_0^2+\hat L_E^2)^{1/2}$ is the effective ambipolar diffusion length of the carriers[14] when $G=\hat G$, where

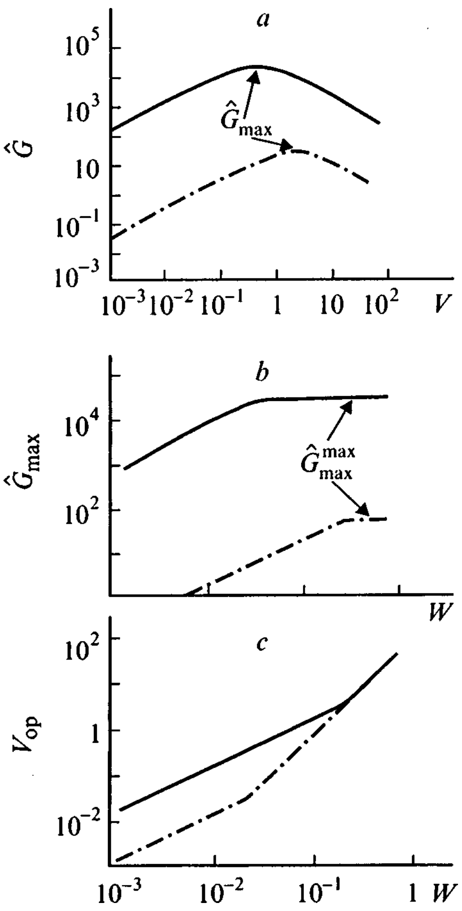

FIG. 2. Dependences in GaAs (solid curves) and Si (dot-dash curves) at $T=300$ K: a — $\hat G$ as a function of the applied voltage V in volts at $W=10^{-1}$ cm, where $\hat G$ is the value of the photoelectric gain G at the maximum point of the function $G(N)$ (Fig. 1a); b — $\hat G_{\mathrm{max}}$ as a function of the distance W in cm between the current contacts, where $\hat G_{\mathrm{max}}$ is the maximum of $\hat G$ for a given value of W (Fig. 2a); c — optimum voltage V_{op} in volts as a function of W in centimeters, which gives the maximum $\hat G=\hat G_{\mathrm{max}}$ for a given value of W (Fig. 2b). The semiconductor parameters are the same as in Fig. 1.

$$\hat L_0^2=\frac{A/\theta+B\sqrt{A+B}}{(A+B)D_n+BD_p}\,\frac{D_nD_p}{w_nN_D}, \qquad (6)$$

$$\hat L_E^2=\frac{\varepsilon}{8\pi q}\,\frac{2A+(B+1)\theta\sqrt{A+B}}{w_pN_Dn_t\sqrt{A+B}}\,\frac{\mu_n\mu_pE_0^2}{(A+B)\mu_n+B\mu_p}, \qquad (7)$$

$\hat L_0$ is the normal (calculated using the quasilinear approximation) ambipolar diffusion length of the carriers when $G=\hat G$, and D_n and D_p are the diffusion coefficients of the electrons and holes. It follows from expression (5) that as the photoresistor voltage $V=WE_0$ increases, $\hat G$ initially increases and then drops (Fig. 2a). This behavior of $\hat G(V)$ is caused by an increase in $\hat L_{\mathrm{eff}}$ as V increases and leads to an increased loss of photocarriers because of their more rapid diffusion influx to current contacts, at which $\Delta n=\Delta p=0$. An increase in

$L_{\mathrm{eff}}=\sqrt{D_{\mathrm{eff}}(E_0)\,\tau_n}$ with increasing V is caused by an increase in the effective ambipolar diffusion coefficient D_{eff} of the carriers as the field E_0 increases[13,14] [D_{eff} is the coefficient of the second derivative in the fourth-order linear equation which, to first order in g, describes the spatial distribution $\Delta n(x)$ (Ref. 14)]. The monotonically increasing behavior of the dependence $D_{\mathrm{eff}}(E_0)$ is then attributed to the space charge induced by the optical radiation $\rho=(\varepsilon/4\pi)\operatorname{div}\Delta E$. An analysis of Eqs. (5)–(7) shows that $\hat{G}(V)$ reaches its maximum (Fig. 2b)

$$\hat{G}_{\max}(W)\cong\begin{cases}\dfrac{25}{72}\dfrac{W}{\hat{L}_0}\hat{G}^{\max}_{\max}, & \text{if } W<2L_0,\\[2ex] \hat{G}^{\max}_{\max}, & \text{if } W>2L_0,\end{cases} \tag{8}$$

at the optimum photoresistor voltage (Fig. 2c)

$$V_{\mathrm{opt}}(W)\cong\begin{cases}\tilde{E}W, & \text{if } W<2\hat{L}_0,\\[2ex] \dfrac{\tilde{E}W^2}{2\hat{L}_0}, & \text{if } W>2\hat{L}_0.\end{cases} \tag{9}$$

Here the highest possible photoelectric gain $\hat{G}^{\max}_{\max}$ (for the given physical parameters of the semiconductor) and the electric field strength $E_0=\tilde{E}$ for which $\hat{L}_{\mathrm{eff}}=\sqrt{2}\hat{L}_0$ holds are given by

$$\hat{G}^{\max}_{\max}=(\mu_n\hat{\tau}_n+\mu_p\hat{\tau}_p)\frac{3\tilde{E}}{25\hat{L}}, \tag{10}$$

$$\tilde{E}=\sqrt{\frac{8\pi}{\varepsilon}kTn_i}\left(1+\frac{A}{B}\right)^{1/4}, \tag{11}$$

where k is the Boltzmann constant and T is the temperature.

Thus, the photoinduced space charge substantially limits the value of $G=\hat{G}$ (Fig. 2a) at the maximum of $G(N)$ (Fig. 1a). Nevertheless, for $W>2\hat{L}_0$ and the optimum voltage (9) (Fig. 2c), $\hat{G}$ may be several orders of magnitude (Fig. 2b).

We are grateful to the Russian Fund for Fundamental Research for financially supporting this work.

[1] A. A. Drugova and V. A. Kholodnov, in *Proceedings of the International Semiconductor Device Research Symposium*, Charlottesville, USA, 1995, Vol. 1, pp. 197–200.

[2] *Optical and Infrared Detectors*, edited by R. J. Keyes (Springer-Verlag, New York, 1977; Radio i Svyaz', Moscow, 1985, 326 pp.)

[3] A. Rogalski *et al.*, *Infrared Photon Detectors* (SPIE Optical Engineering Press, Bellingham, Washington, 1995), 644 pp.

[4] H. Beneking, IEEE Trans. Electron Devices **ED-29**, 1420 (1982).

[5] D. L. Smith, F. K. Lo, and J. D. Genova, J. Vac. Sci. Technol. **21**, 259 (1982).

[6] C. T. Elliott, in *Handbook on Semiconductors*, edited by C. Hilsum (North-Holland, Amsterdam, 1982), Vol. 4, p. 727.

[7] S. M. Ryvkin, *Photoelectric Effects in Semiconductors*, Consultants Bureau, New York, 1964) [Russ. original, Fizmatgiz, Moscow, 1963, 496 pp.]

[8] R. H. Bube, *Photoconductivity of Solids* (Wiley, New York, 1960; IL, Moscow, 1962, 558 pp.)

[9] A. G. Milnes, *Deep Impurities in Semiconductors* (Wiley, New York, 1973; Mir, Moscow, 1977, 562 pp.)

[10] A. Rose, *Concepts in Photoconductivity and Allied Problems* (Interscience, New York, 1963; Mir, Moscow, 1966, 192 pp.)

[11] R. Loepfe, A. Schaelin, M. Blaser *et al.*, Appl. Phys. Lett. **52**, 2130 (1988).

[12] P. M. Downey, R. J. Martin *et al.*, Appl. Phys. Lett. **46**, 396 (1985).

[13] V. A. Kholodnov and A. A. Drugova, Pis'ma Zh. Tekh. Fiz. **23**(2), 80 (1997) [Tech. Phys. Lett. **23**, 82 (1997)].

[14] V. A. Kholodnov, JETP Lett. **67**, 685 (1998).

[15] A. A. Drugova and V. A. Kholodnov, Pis'ma Zh. Tekh. Fiz. **18**(1) 23 (1992) [Tech. Phys. Lett. **18**, 8 (1992)].

[16] A. A. Drugova and V. A. Kholodnov, Solid-State Electron. **38**(6), 1247 (1995).

[17] V. A. Kholodnov, Fiz. Tekh. Poluprovodn. **30**, 1011 (1996) [Semiconductors **30**, 538 (1996)].

[18] S. M. Sze, *Physics of Semiconductor Devices*, Book 1 (Wiley, New York, 1969; Mir, Moscow, 1984, 455 pp.)

[19] J. S. Blakemore, *Semiconductor Statistics* (Pergamon Press, Oxford, 1962; Mir, Moscow, 1964, 392 pp.

[20] P. S. Kireev, *Semiconductor Physics* [in Russian], Vysshaya Shkola, Moscow (1969), 590 pp.

[21] R. A. Smith, *Semiconductors* (Cambridge University Press, Cambridge, 1959; Russ. transl., later ed., Mir, Moscow, 1982, 600 pp.)

[22] J. S. Blakemore, *Solid State Physics*, 2nd ed. (Cambridge University Press, Cambridge, 1985; Mir, Moscow, 1988, 608 pp.)

[23] V. A. Kholodnov and P. S. Serebrennikov, Pis'ma Zh. Tekh. Fiz. **23**(7), 39 (1997) [Tech. Phys. Lett. **23**, 268 (1997)].

[24] V. A. Kholodnov and P. S. Serebrennikov, Pis'ma Zh. Tekh. Fiz. **23**(24), 58 (1997) [Tech. Phys. Lett. **23**, 969 (1997)].

[25] V. L. Bonch-Bruevich and S. G. Kalashnikov, *Semiconductor Physics* [in Russian], Nauka, Moscow (1990), 688 pp.

[26] S. M. Sze, *Physics of Semiconductor Devices*, Book 2 (Wiley, New York, 1969; Mir, Moscow, 1984, 455 pp.)

Translated by R. M. Durham

TECHNICAL PHYSICS LETTERS VOLUME 25, NUMBER 3 MARCH 1999

Influence of traps on avalanche triggering during breakdown of gallium phosphide *p–n* junctions

S. V. Bulyarskiĭ, Yu. N. Serezhkin, and V. K. Ionychev

Moscow State University, Saransk Ulyanovsk State University, Ulyanovsk

(Submitted November 5, 1998)
Pis'ma Zh. Tekh. Fiz. **25**, 9–13 (March 12, 1999)

Deep centers are found to strongly influence the statistical delay of microplasma breakdown in gallium phosphide red LEDs. It is postulated that this effect is caused by Shockley electrons triggering an avalanche or by subthreshold mechanisms of impact ionization. It is shown that the statistical delay in the microplasma breakdown can be used to determine the parameters of the deep centers if the charge state of the deep centers is varied by reducing the $p-n$ junction voltage. © *1999 American Institute of Physics.* [S1063-7850(99)00203-7]

As we know, the avalanche breakdown of real $p-n$ junctions exhibits microplasma behavior and microplasmas possess a statistical breakdown delay.[1] Various authors[2–4] have studied the influence of deep centers on the breakdown delay of microplasmas. In these studies a change in the charge state of the deep centers was caused by the flow of avalanche current. Thus, both electrons and holes are trapped in the microplasma channels. In this case, the charge state of the deep centers changed over the entire microplasma channel, including the region of maximum electric field. Consequently, the Frenkel–Poole effect and tunneling could have some influence during the emission of trapped carriers. All these factors made it very difficult to interpret the experimental data.

In the present study the deep centers were filled by partially reducing the bias voltage across the $p-n$ junction. In this case, the deep centers are only filled by majority carriers (electrons from the *n*-base or holes from the *p*-base). Moreover, the filling can only occur in that part of the space-charge region where the electric field strength is relatively low.

Breakdown delay was investigated using commercial AL102 gallium phosphide red LEDs. The breakdown voltage of the first microplasma U_M at room temperature was 18–19 V. The capacitance–voltage characteristics, particularly at low voltages, revealed an approximately linear dependence $C_B^{-3} = f(U)$ with a concentration gradient of around $2.5 \times 10^{22}\,\mathrm{cm}^{-4}$. Capacitance methods revealed no deep centers.

After the diode voltage had been reduced to U_m, a voltage U was applied, a few percent higher than the microplasma breakdown voltage. After a time t_d a microplasma started and an avalanche current began to flow. Then the voltage again dropped to U_m. In order to eliminate the aftereffects of the avalanche current, including thermal effects, the diode was held at U_m for 1–5 s depending on the temperature.

Figure 1 shows distribution functions of the duration of the microplasma breakdown delay. The curves are plotted for 1000 pulses. Curve *1* gives the distribution function with no additional filling of deep centers. As might be expected in the classical case,[1] this is an exponential distribution. Curve *2* shows the distribution function with filling of deep centers and curve *3* is the difference. It is assumed that the contribution of all other avalanche triggering mechanisms is eliminated. In most cases, the difference curve is accurately approximated by

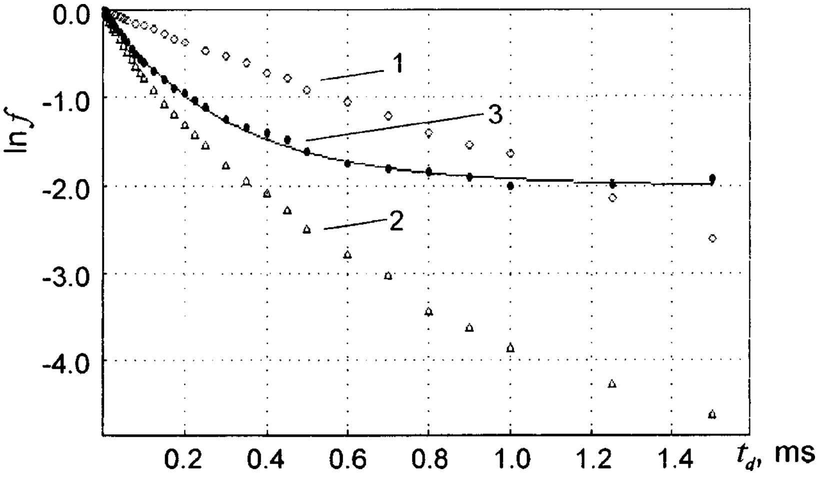

FIG. 1. Distribution function of the duration of the microplasma breakdown delay: $T = 271.3$ K, $U_M = 17.65$ V, $U - U_M = 0.3$ V, and $U_m = 13.5$ V. The solid curve gives the approximation from Eq. (1).

1063-7850/99/25(3)/2/$15.00

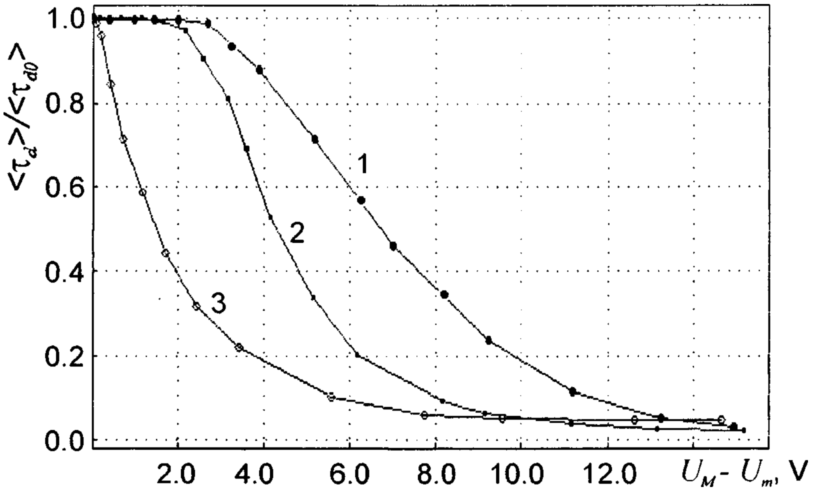

FIG. 2. Average breakdown delay time as a function of filling voltage: $\langle \tau_d \rangle$ — average delay time with filling of deep centers, $\langle \tau_{d0} \rangle$ — average delay time without filling of deep centers, $U - U_M = 0.65$ V; T, K: *1* — 382, *2* — 305, and *3* — 224.

$$\ln f = A\left[\exp\left(-\frac{t_d}{\tau}\right) - 1\right]. \tag{1}$$

In some cases, it may be approximated by the sum of two exponential functions. Curve *3* agrees with the theoretical distribution[5] if the avalanche is triggered by remission of majority carriers from traps. In this case, τ is the average confinement time for trapped carriers at a trap and

$$\tau = e_n^{-1} \quad \text{or} \quad \tau = e_p^{-1}, \tag{2}$$

where e_n and e_p are the coefficients of thermal emission of electrons and holes, respectively. If e_n and e_p are represented as Arrhenius curves their temperature is accurately described by a linear dependence. For instance, in the temperature range 290–330 K the influence of a single deep level with the activation energy 0.35 ± 0.01 eV is observed. The influence of six levels is only observed at 100–400 K. Since capacitance methods reveal no deep levels in these diodes, we can postulate that these deep centers are mainly situated in microplasma channels.

The calculations show that for normal values of the coefficients of impact ionization of electrons and holes, the parameter A in Eq. (1) only differs appreciably from zero when the triggering carriers start from deep regions of the space-charge zone. However, this requires the filling voltage U_m to be several tens of volts lower than the microplasma breakdown voltage.[6] It was unexpectedly found that this is not the case with these gallium phosphide diodes. Figure 2 gives the average breakdown delay time as a function of the filling voltage. The delay time begins to decrease even for low values of $U_M - U_m$. In the case shown this difference is only 2–3 V at 382 K. As the temperature decreases, the width of the plateau decreases and at $T \leqslant 250$ K it almost disappears. This behavior is typical of all the deep levels observed. Note that measurements in silicon diodes with $U_M = 32$ V gave a 12 V plateau at 177 K.

The usual assumptions that the threshold ionization energy is reduced in the microplasma region or the electric field is increased do not explain the observed temperature dependence of the effect. The high concentration of deep centers in the microplasma channel is also problematical, because in this case a relaxation breakdown delay should be observed.[1]

We assume that in gallium phosphide the electron energy distribution function in strong electric fields is spherically symmetrical, whereas in silicon it is elongated in the direction of the electric field, which can be attributed to the different mechanisms responsible for the carriers acquiring the threshold ionization energy in these materials. In gallium phosphide however, there are a few electrons which can avoid collisions with phonons before impact ionization (Shockley electrons), and we can postulate that these mainly trigger the avalanche. The influence of subthreshold mechanisms such as tunnel-impact ionization must also be taken into account.[7] In these cases, the probability of an avalanche being triggered cannot be calculated using the normal values of the ionization coefficients. However, these investigations open up new possibilities for studying impact ionization processes in semiconductors.

This work was supported by the Russian Fund for Fundamental Research (Grant No. 98-02-03334).

[1] I. V. Grekhov and Yu. N. Serezhkin, *Avalanche Breakdown of a p–n Junction in Semiconductors* [in Russian], Énergiya, Leningrad (1980) 152 pp.

[2] C. Kimura and J. Nishizawa, J. Phys. Soc. Jpn. **7**, 1453 (1968).

[3] G. Ferenczi, Solid-State Electron. **17**, 903 (1974).

[4] K. I. Nutall and M. W. Nield, Solid-State Electron. **18**, 13 (1975).

[5] S. V. Bulyarskiĭ, V. K. Ionychev, and Yu. N. Serezhkin, in *Proceedings of the International Conference on "Centers with Deep Levels in Semiconductors and Semiconducting Structures,"* Ul'yanovsk, Russia, 1997 [in Russian], pp. 77–78.

[6] A. S. Kyuregyan and Yu. N. Serezhkin, Fiz. Tekh. Poluprovodn. **15**, 689 (1981) [Sov. Phys. Semicond. **15**, 392 (1981)].

[7] A. S. Kyuregyan, Fiz. Tekh. Poluprovodn. **10**, 690 (1976) [Sov. Phys. Semicond. **10**, 410 (1976)].

Translated by R. M. Durham

TECHNICAL PHYSICS LETTERS VOLUME 25, NUMBER 3 MARCH 1999

Estimate of the amplitude of a doubled period in the solutions of a system of Rössler equations

V. A. Dvinskikh

N. G. Chernyshevskiĭ State University, Saratov

(Submitted September 16, 1998)
Pis'ma Zh. Tekh. Fiz. **25**, 14–17 (March 12, 1999)

A description is given of a method of calculating the parameters of periodic components in discrete data which can also be used to calculate the levels of constant and variable components. The amplitude of a doubled period is estimated by isolating the fundamental oscillation component and subtracting its spectrum. *© 1999 American Institute of Physics.* [S1063-7850(99)00303-1]

Anishchenko[1] examined a procedure for constructing bifurcation lines of the repetition period of cycles of one of the Rössler model systems

$$\dot{x}=-y-z,\quad \dot{y}=x+ey,\quad \dot{z}=b+xz-\mu z \tag{1}$$

with the parameters $e=b=0.2$. Then for $\mu=2.5$ a stable limit cycle exists with the period T_0, but for $\mu\sim 2.83$ this cycle undergoes a period doubling bifurcation.

This system of equations is solved by a fourth-order Runge–Kutta method with a step of 0.1 for $x_0=2.5$, $y_0=z_0=0$ for $\mu=2.83$. Figure 1 gives the dependence of x on the number of readings in the solution and clearly shows period doubling in addition to the fundamental oscillation.

The aim of the present paper is to estimate the amplitude of the doubled period when there is a bounded solution interval.

It is known[2] that the classical method of calculating the parameters of the spectral components of digital signals based on using a discrete Fourier transform has poor resolution. The bounded interval of observation leads to distortion of the calculated spectrum because of the interpenetration of its components. Various windows having a broader smooth lobe compared with a rectangular window are used to reduce the level of the side lobes, which lowers the frequency selectivity. Parametric methods[2] having a higher selectivity have recently come into use, although at a negligible noise level. When these methods are used, the constant component must be preliminarily eliminated from the data. In addition to making the treatment process more complicated, this may also lead[3] to additional error in calculations of the level of the variable components.

We shall analyze the series of readings $x(n)$; $n=1,2,\dots,N$ containing P periodic components. Their number and frequencies are unknown, but we can indicate the predicted frequency range. We shall divide this into L inter-

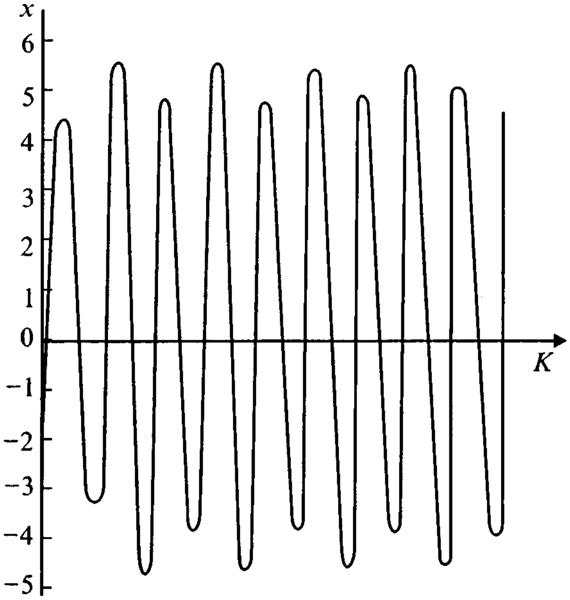

FIG. 1. Dependence of a series of oscillations on the number of readings.

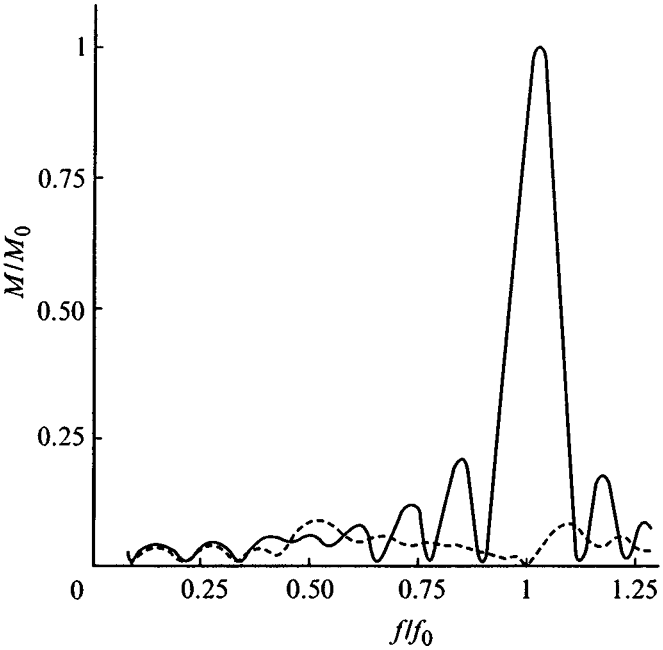

FIG. 2. Frequency dependences of the spectra in relative form: solid curve — initial spectrum, dashed curve — difference between the initial spectrum and the spectrum calculated from the action of the isolated fundamental oscillation.

vals in each of which we approximate the signal by the trigonometric polynomial[4]

$$y_j(n)=G_j+S_j\sin(h_jn)+C_j\cos(h_jn),\quad j=1,2,\ldots,L\gg P,$$

where $h_j=2\pi/N_j$ is the calculation step for the boundary of the jth interval, with N_j the number of data points per period of this boundary. Unlike a Fourier transformation, this step can have fractional values which can reveal fine details of the spectrum.

The method of least squares is used to calculate the values of the coefficients S_j, C_j, $j=1,2,\ldots,L$. For a frequency step of 0.0025 the dependence of the absolute value

$$M_j=\sqrt{S_j^2+C_j^2},\quad j=1,2,\ldots,L$$

is plotted in relative form in Fig. 2 (solid curve) which clearly shows the strong influence of the side lobes of the fundamental oscillation.

Approximating expressions which can reduce the influence of the side lobes near a high-intensity oscillation are given in Ref. 5. In this particular case, it is best to isolate the fundamental oscillation

$$q_k=G_k+S_k\sin(b_ki)+C_k\cos(b_ki),$$

where G_k, S_k, and C_k are coefficients, b_k is the frequency factor, and i is a variable which varies in the same range as the initial process.

We then determine the dependence of the absolute value

$$MK_j=\sqrt{Z1_j^2+Z2_j^2},\quad j=1,2\ldots,L$$

where $Z1$ and $Z2$ are levels of the spectral components of the action of the fundamental oscillation. We then make the systematic subtraction

$$W1_j=S_j-Z1_j,\quad W2_j=C_j-Z2_j,\quad j=1.2,\ldots,L$$

and calculate the dependence of the absolute value

$$MR_j=\sqrt{W1_j^2+W2_j^2},\quad j=1,2,\ldots,L.$$

Figure 2 (dashed curve) gives the dependence of the difference between the spectra from which the level of the doubled period can easily be calculated. The fact that this dependence exhibits some nonuniformity is attributable to the finite frequency step and the influence of rounding errors.

[1] V. S. Anishchenko, *Complex Oscillations in Simple Systems* [in Russian], Nauka, Moscow (1990), 312 pp.

[2] S. L. Marple, *Digital Spectral Analysis with Applications* (Prentice-Hall, Englewood Cliffs, N.J., 1987; Mir, Moscow, 1990, 535 pp.)

[3] R. W. Hamming, *Digital Filters* (Prentice-Hall, Englewood Cliffs, N.J, 1977; Nedra, Moscow, 1987, 221 pp.]

[4] V. A. Dvinskikh, Zh. Tekh. Fiz. **62**(12), 168 (1992) [Sov. Phys. Tech. Phys. **37**, 1213 (1992)].

[5] V. A. Dvinskikh, Radiotekh. Elektron. **37**, 1129 (1992).

Translated by R. M. Durham

TECHNICAL PHYSICS LETTERS VOLUME 25, NUMBER 3 MARCH 1999

Investigation of the action of ultrahigh pressures on carbon nanotubes

A. M. Germanskiĭ, G. A. Dyuzhev, D. V. Novikov, V. M. Oĭchenko, and Yu. P. Udalov

St. Petersburg State Technological Institute (Technical University)
A. F. Ioffe Physicotechnical Institute, Russian Academy of Sciences, St. Petersburg
A. M. Bonch-Bruevich State University of Telecommunications, St. Petersburg

(Submitted September 3, 1998)
Pis'ma Zh. Tekh. Fiz. **25**, 18–21 (March 12, 1999)

An investigation is made of the possibility of obtaining technical-grade diamonds in ultrahigh-pressure apparatus by using the cathode deposits formed during fullerene production in an arc discharge as raw material. It is shown that carbon nanostructures present in the cathode deposit increase the number of diamond crystallization centers compared with standard graphite. © *1999 American Institute of Physics.* [S1063-7850(99)00403-6]

One of the potentially useful practical applications of fullerenes is the production of technical-grade diamonds. We know that the addition of fullerenes to a standard graphite mixture used to synthesize diamonds at ultrahigh pressures enhances the diamond yield and shifts the particle size distribution curve towards ultradisperse.

Carbon nanotubes, which were observed experimentally[1] in 1991, immediately attracted increased interest among researchers because of their unique electrical[2] and mechanical properties.[3,4]

The aim of the present paper is to study the prospects for using nanotubes to produce artificial diamonds.

The main method of producing nanotubes of practical value is by evaporation of graphite in an arc discharge. Nanotubes and other nanostructures form a constituent part of a so-called cathode deposit (or cathode ''fungus'') which ''grows'' on the cathode during the discharge burning process. These structures are formed from atomized carbon[5,6] at high cathode surface temperatures (above 4000 K) under intensive bombardment by ions impinging on the cathode from the plasma and accelerated at the cathode potential drop.

For our study we used cathode deposits obtained from commercial fullerene production systems of the ''Fullerene Technologies'' Company (St. Petersburg). The discharge parameters were as follows: current 180 A, helium pressure 90 Torr, and electrode gap 5 mm. The deposits were ground in a ball mill to give a powder with particle size less than 100 μm. The results of an x-ray structural analysis and electron microscopy indicate that the nanostructures formed a considerable part of the ground powder.

The powder was treated in an ultrahigh-pressure apparatus with temperature 1400 °C, pressure 5 GPa, and treatment time 30 s.

The initial powders and products obtained at high temperatures and ultrahigh pressures were analyzed using a Super SEM scanning electron microscope (Asahi), an ÉMV-100L transmission electron microscope, and a DRON-04 x-ray diffractometer using Cu K_α radiation at 40 kV and 20 mA.

Several typical nanostructures contained in the initial powder are shown in Fig. 1.

Figure 2 shows x-ray diffraction patterns of samples of different carbon materials.

Curve *1–1* was obtained for ÉG-15 electrode graphite and contains a set of reflexes from the (002), (101), and (004) planes typical of the hexagonal and orthorhombic forms of the graphite structure.

Curve *2–2* was obtained for the initial powder of the cathode deposit. It can be seen that the principal reflexes characteristic of the graphite crystal structure remain. The observed broadening of the reflexes suggests that the regions of coherent scattering are small (calculations using the half-width of the lines give 3.2 nm).

Curve *3–3* gives an x-ray diffraction pattern of the cathode deposit powder after treatment in an ultrahigh-pressure apparatus, which shows that no structural changes occurred

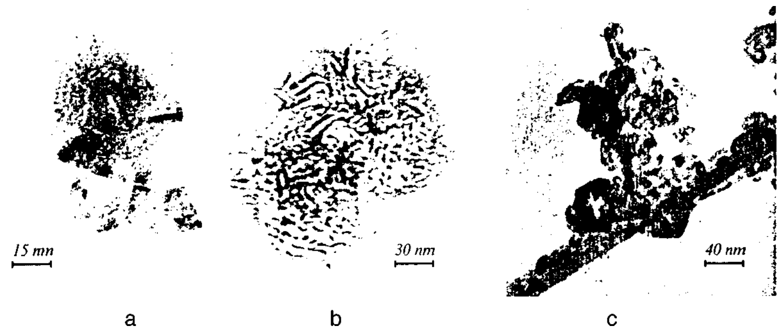

FIG. 1. Electron photomicrographs of various nanostructures in cathode deposit: a — polyhedral structures, b — nanotube accumulation, and c — nanotube with outgrowth.

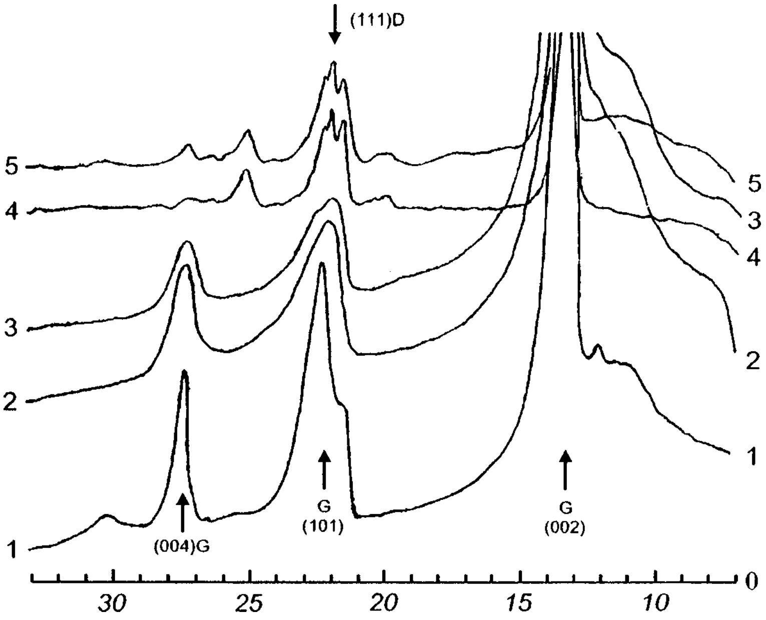

FIG. 2. X-ray diffraction patterns of samples of various carbon materials: *1–1* — ÉG-15 electrode graphite, *2–2* — initial powder of graphite deposit, *3–3* — cathode deposit after treatment at 1400 K and 5 GPa for 30 s, *4–4* — cathode deposit after treatment in regime *3–3* in the presence of a manganese–nickel catalyst, and *5–5* — ÉG-15 graphite mixed with manganese–nickel catalyst after treatment in regime *3–3*.

in the sample. This suggests that the nanostructures possess high mechanical and thermal strength, which agrees with the results reported by Treacy *et al.*[3] and Yakobson *et al.*[4]

In industrial technology, artificial diamonds are usually produced using graphite powder mixed with a manganese–nickel alloy as a catalyst. Curve *4–4* gives the result of treating powdered cathode deposit mixed with a commercial manganese–nickel catalyst in an ultrahigh-pressure apparatus. The (111) diamond reflex can be clearly distinguished. The quantity of diamonds formed is around 20 wt.% and the maximum size of the crystallites is 20–50 μm.

In parallel experiments the cathode deposit was replaced by ÉG-15 graphite (curve *5–5*). In this case the size of the diamond crystals was 150–200 μm and the total diamond content in the sinter was around 20% by mass.

These results suggest that carbon nanostructures in contact with a manganese–nickel melt effectively interact to form carbides of these metals. In this case, the activity of the nanostructures has the effect of increasing the number of diamond crystallization centers compared with standard graphite, which reduces the sizes of the diamond crystallites.

[1] S. Iijima, Nature (London) **354**, 56 (1991).
[2] M. S. Dresselhaus, G. Dresselhaus, and P. C. Eklund, *Science of Fullerenes and Carbon Nanotubes* (Academic Press, New York, 1995).
[3] M. M. J. Treacy, T. N. Ebbesen, and J. M. Gibson, Nature (London) **381**, 678 (1996).
[4] B. I. Yakobson, C. J. Brabec, and J. Bernholc, Phys. Rev. Lett. **76**, 2511 (1996).
[5] R. Pallaser, L. S. K. Pang, L. Prochazka, D. Rigby, and M. A. Wilson, J. Am. Chem. Soc. **115**, 11 634 (1993).
[6] G. Dyuzhev, Mol. Mater. **7**, 61 (1996).

Translated by R. M. Durham

Determination of the parameters of deep levels using the differential coefficients of the current–voltage characteristics

S. V. Bulyarskiĭ, M. O. Vorob'ev, N. S. Grushko, and A. V. Lakalin

Ulyanovsk State University

(Submitted September 4, 1998)
Pis'ma Zh. Tekh. Fiz. **25**, 22–27 (March 12, 1999)

Deep levels were determined in GaP light-emitting diodes using the differential coefficients of the current–voltage characteristics. The parameters determined by different methods showed agreement. The measurement conditions are such that the measurements can be made using wafers, which makes the proposed methods extremely promising. © *1999 American Institute of Physics.* [S1063-7850(99)00503-0]

The classical work carried out by Sah, Noyce, and Shockley[1] provided the impetus for studying recombination processes in the space charge region. Later theoretical studies refined the form of the current–voltage characteristics. Experimental studies were generally confined to confirming the current transport mechanism in a particular range of forward bias. Only in Refs. 2–4 did we develop methods of analyzing the current–voltage characteristics based on separating overall recombination processes into individual components and then calculating the parameters of the deep levels involved in the recombination. Here we use new differential techniques of determining the activation energy of deep levels.[4]

Differential techniques can reveal characteristics which are barely detectable on the overall characteristics. In particular, the parameters of deep levels can be calculated using the current–voltage characteristics under forward bias. Here we investigate the properties of nitrogen-doped GaP diodes emitting in the green as an example of this technique.

At low levels of injection, the recombination currents in the space charge region of the $p-n$ junction of a wide-gap semiconductor usually exceed the diffusion currents. The current–voltage characteristic is typically described by the expression

$$J = A(U)\exp(qU/\beta kT), \tag{1}$$

where β has values between 1 and 2 (for diffusion currents $\beta = 1$). The physical processes of recombination in the space charge region of a $p-n$ junction were described in detail in Refs. 1–8. The coefficient of proportionality $A(U)$ depends on the deep level parameters. The extrema of the derivative of the gradient of the current–voltage characteristic (β) are given by

$$\beta = \frac{qJ_r}{kT}\left(\frac{\partial J_r}{\partial U}\right)^{-1}. \tag{2}$$

The recombination current (J_r) in the space-charge region of the $p-n$ junction, with the participation of several deep doubly-charged levels, is[5]

$$J_r = \sum_{m=1}^{s} \frac{qwc_{nm}c_{pm}n_i^2(e^{qU/kT}-1)N_{tm}}{2n_i\sqrt{c_{nm}c_{pm}e^{qU/2kT}}+c_{nm}n_{1m}+c_{pm}p_{1m}} \times x\frac{2kT}{q(V_d-U)}, \tag{3}$$

where q is the electron charge, w is the width of the space charge region, s is the number of deep levels, $n_{1m}=N_c \times \exp(-E_{tm}/kT)$, $p_{1m}=N_v\exp(-E_{tm}/kT)$, c_n and c_p are the coefficients of electron and hole capture by a particular center, averaged over all states, N_t is the concentration of deep levels, E_t is the position of the deep level in the band gap, $E_{tn}=E_c-E_t$, $E_{tp}=E_t-E_v$, and V_d is the diffusion potential.

Formula (2) differs slightly from the expressions given in Ref. 1. This difference was analyzed in detail in Ref. 6 and we shall not discuss it here. The limits of validity of expression (3) were established in Refs. 2–5.

It follows from formula (2) that the differential gradient of the current–voltage characteristic, β, contains the parameters of the deep levels (their thermal activation energies), which can be determined. From the maxima U_{0m} of the dependence of the derivative (β) with respect to the forward bias voltage we find

$$E_{tn} = \frac{E_g - qU_{0m}}{2} + \delta. \tag{4}$$

We shall assume that the deep level lies above the middle of the band gap and $c_pp_1 \ll c_nn_1$, $\delta=(kT/2)\ln(c_nN_c/c_pN_v)$. This value, like the capture coefficients, is generally unknown. However, the ratios of the capture coefficients can be determined by measuring the temperature dependence of the forward current.[2,3] Assuming that $c_n/c_p=100$, then at $T=300$ K the systematic error is $\delta \approx 0.04$ eV for GaP. Figure 1 (curves *1* and *2*) gives the experimental dependences of ($d\beta/dU$) measured for green light-emitting diodes. The measurements were made using a pc-controlled system. The forward bias voltage was varied with a step of 0.01 V. In this case, several experimental points can be obtained at the peaks of the derivative. Repeated measurements showed

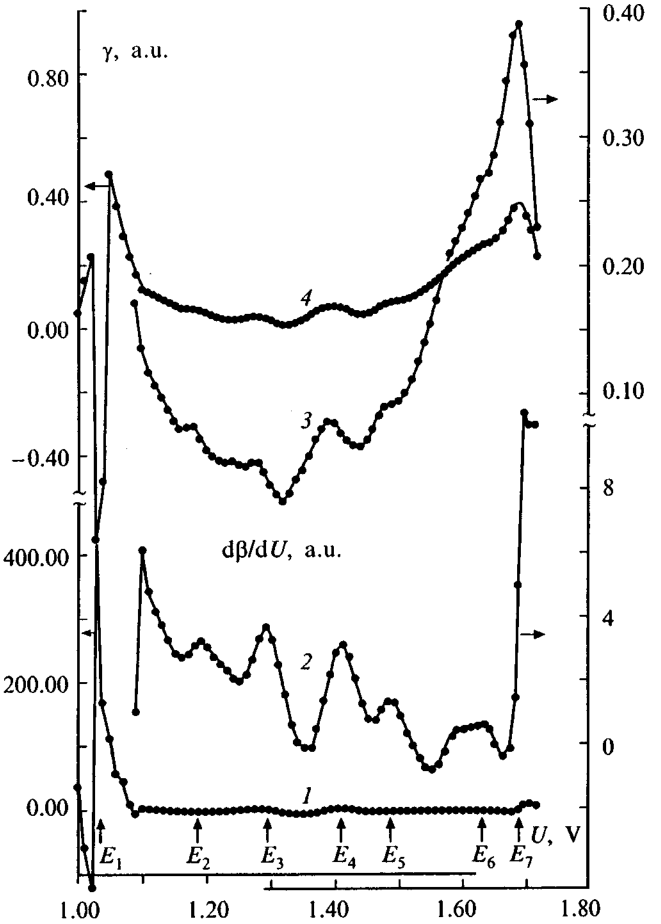

FIG. 1. Differential coefficients of current–voltage characteristic. The number of the extremum corresponds to the level number (see Table I).

good reproducibility. Light-emitting diodes in the same series showed the same results. Thus, these experimental curves can be considered to be reliable. The curves are plotted on different scales, since different centers do not make equal contributions to the recombination process. It can be seen from curve *1* that E_1 makes the largest contribution to the recombination, while the E_7 level and the other recombination levels make a considerably smaller contribution. The activation energies determined using formula (4) are shown in Table I.

A disadvantage of this method is the need to calculate the second derivative of the experimental data which necessitates using special numerical techniques. Thus, it is more convenient to use another differential coefficient for which we only need to calculate the first derivative:

$$\gamma=\left(\frac{\partial R_{np}}{\partial U}\right)\frac{2kT}{q}\,\frac{1}{R_{np}}. \tag{5}$$

The reduced recombination velocity R_{np} is calculated from the experimental data and is given by the following formula:[4]

$$R_{np}=\frac{J}{qwSn_i\left[\exp\left(\frac{qU}{2kT}\right)-1\right]}\,\frac{q(V_d-U)}{2kT}. \tag{6}$$

The relationship between this quantity and the deep level parameters is given by[2,3]

$$R_{np}=\frac{c_nc_pn_iN_t\left[\exp\left(\frac{qU}{2kT}\right)+1\right]}{2n_i\sqrt{c_nc_p}\exp\left(\frac{qU}{2kT}\right)+n_1c_n+p_1c_p}. \tag{7}$$

The voltage at which the coefficient (5) has a minimum (see Fig. 1, curves *3* and *4*) can be used to determine the activation energy of the deep levels using formula (4). In this case, certain conditions obtained in Ref. 4 must be satisfied. For deep levels formed during the fabrication of commercial semiconductor devices these conditions are satisfied. The function (4) has minima at the points U_{0m}. The amplitude of each minimum will differ, depending on the contribution of the specific deep level to the total recombination current. It can be seen from Fig. 1 (curves *3* and *4*) that the main contribution to the recombination process is made by levels E_1, E_3, E_6, and E_7. The activation energies of these levels are given in Table I.

The results of determining the activation energies using the differential parameters are compared in Table I with the capacitance spectroscopy data and the method of separating the recombination velocity into components which was described in Refs. 2–4. The results of independent experiments show good agreement, suggesting that the deep level parameters obtained using differential techniques are reliable. The measurements are made at constant temperature, usually room temperature. The measurement conditions are such that measurements can be made directly using wafers before these are separated and assembled. These undoubted advantages make the techniques described here extremely promising.

TABLE I. Activation energies of deep levels determined by various methods for GaP light-emitting diodes (sample 5–2).

Method	E_7, eV	E_6, eV	E_5, eV	E_4, eV	E_3, eV	E_2, eV	E_1, eV	E_8, eV	E_9, eV	E_{10}, eV
TCE		0.35				0.53	0.63	0.66	0.81	1.0
R_{np}	0.29	0.33			0.48	0.56	0.61			
$\frac{d\beta}{dU}$	0.27	0.32	0.38	0.42	0.48	0.52	0.61			
γ	0.26	0.30	0.37	0.41	0.46	0.54	0.61			

---

[1] C. T. Sah, R. N. Noyce, W. Shockley, Proc. IRE **45**, 1228 (1957).

[2] S. V. Bulyarskiĭ and N. S. Grushko, in *Physical Principles of the Functional Diagnostics of p–n Junctions with Defects* [in Russian], Shtiintsa, Kishinev (1992), p. 235.

[3] S. V. Bulyarskiĭ and N. S. Grushko, in *Generation-Recombination Processes in Active Elements* [in Russian], Moscow State University Press, Moscow (1995), p. 399.

[4] S. V. Bulyarskiĭ, N. S. Grushko, and A. V. Lakalin, Zavod. Labor. No. 7, 25 (1997).

[5] S. V. Bulyarskiĭ, N. S. Grushko, and A. V. Lakalin, in *Abstracts of the International Conference on Centers with Deep Levels in Semiconductors and Semiconducting Structures*, Ul'yanovsk, Russia, 1997 [in Russian], pp. 65–66.

[6] S. V. Bulyarskiĭ, N. S. Grushko, A. I. Somov, and A. V. Lakalin, Fiz. Tekh. Poluprovodn. **31**, 1146 (1997) [Semiconductors **31**, 983 (1997)].
[7] S. V. Bulyarskiĭ and S. I. Radautsan, Fiz. Tekh. Poluprovodn. **15**, 1443 (1981) [Sov. Phys. Semicond. **15**, 836 (1981)].
[8] S. V. Bulyarskiĭ, I. V. Stratan, and N. S. Grushko, Fiz. Tekh. Poluprovodn. **21**, 1730 (1987) [Sov. Phys. Semicond. **21**, 1047 (1987)].

Translated by R. M. Durham

TECHNICAL PHYSICS LETTERS VOLUME 25, NUMBER 3 MARCH 1999

Possible emission of supermodes in a free electron laser with a transversely developed interaction space

N. S. Ginzburg, N. Yu. Peskov, A. S. Sergeev, A. V. Arzhannikov, and S. L. Sinitskiĭ

Institute of Applied Physics, Russian Academy of Sciences, Nizhniĭ Novgorod Institute of Nuclear Physics, Siberian Branch of the Russian Academy of Sciences, Novosibirsk

(Submitted October 26, 1998)
Pis'ma Zh. Tekh. Fiz. **25**, 28–34 (March 12, 1999)

A theoretical analysis is made of the formation of the transverse field profile in a free electron laser with an oversize planar-geometry Bragg cavity driven by a ribbon electron beam. It is shown that cw spatially coherent lasing may be achieved with an oversize parameter of the order of 50 with the excitation of supermodes comprising a set of ''cold'' waveguide modes. © *1999 American Institute of Physics.* [S1063-7850(99)00603-5]

A free-electron laser (FEL) with a planar one-dimensional Bragg cavity and a ribbon relativistic electron beam was developed in the course of experimental investigations using the U-2 accelerator (Institute of Nuclear Physics, Siberian Branch of the Russian Academy of Sciences).[1,2] The highest output power yet recorded in the 4 mm range, 200 MW, with a stored energy of up to 200 J per microwave pulse was achieved in this oscillator. The width of the ribbon relativistic electron beam with a particle energy of 1 MeV and total current of 4 kA was 8–12 cm. The transverse dimension (width) of the cavity l_x was 20 cm, i.e., the oversize parameter l_x/λ for this oscillator was of the order of 50. In this context, the transverse mode composition of the radiation and thus its spatial coherence is a very important topic requiring further theoretical and experimental investigation.

Here we report a theoretical analysis and numerical simulation of the formation of the transverse structure of the emitted radiation. We assume that the cavity consists of two parallel plates (Fig. 1) and the end sections of the plates are corrugated so that these sections form Bragg mirrors of length $l_{1,2}$. Between the mirrors there is a regular section of cavity of length l_0, and we assume that the cavity is closed by metal plates at the ends.

In order to investigate the space–time dynamics of a FEL oscillator with this type of cavity, the field therein can be represented as a set of two counterpropagating quasioptical wave beams:

$$\mathbf{E}=\mathbf{E}_0(y)[\mathcal{A}_+e^{i\omega t-ihz}+\mathcal{A}_-e^{i\omega t+ihz}]. \tag{1}$$

Here $\mathbf{E}_0(y)$ is a function which defines the field distribution between the plates (along the y axis), which is the same as one of the natural modes of the planar waveguide, and $\mathcal{A}_\pm(x,z,t)$ are functions which determine the evolution of the field profile in the (x,z) plane. We assume that the wave beam $\mathcal{A}_+$ copropagating with the particles is amplified by the electron flux. With allowance for the diffraction of the fields, the evolution of the wave beams in the transverse direction (along the x axis) is described by parabolic equations.[3] Allowance for diffraction spreading is fundamentally important for this FEL system because the relative influence of the various parts of the electron flux is only achieved via this effect. The wave beams undergo a mutual transformation inside the Bragg mirrors, which is described by the coupled-wave approximation for weak corrugation. As a result, having selected the Bragg frequency $\omega=\overline{\omega}=\pi c/d$ (where d is the corrugation period) as the carrier frequency, we have for the amplitudes of the wave beams

$$i\frac{\partial^2}{\partial X^2}A_+ +\left(\frac{\partial}{\partial Z}+\beta_{\mathrm{gr}}^{-1}\frac{\partial}{\partial\tau}\right)A_+ + i\alpha(Z)A_- = J,$$

$$i\frac{\partial^2}{\partial X^2}A_- -\left(\frac{\partial}{\partial Z}-\beta_{\mathrm{gr}}^{-1}\frac{\partial}{\partial\tau}\right)A_- + i\alpha(Z)A_+ = 0. \tag{2}$$

The excitation factor $J=(1/\pi)\int_0^{2\pi}e^{-i\theta}d\theta_0$ on the right-hand side of Eq. (2) may be determined by solving the averaged equations for the electron motion

$$\left(\frac{\partial}{\partial Z}+\beta_\parallel^{-1}\frac{\partial}{\partial\tau}\right)^2\theta=\mathrm{Re}(A_+e^{i\theta}). \tag{3}$$

The following dimensionless notation was used for Eqs. (2) and (3): $Z=z\overline{\omega}C/c$, $X=x\overline{\omega}\sqrt{2C}/c$, $\tau=tC\overline{\omega}$, $A_\pm=\mathcal{A}_\pm e\kappa\mu/\gamma mc\overline{\omega}C^2$; $\kappa\approx\beta_\perp/\beta_\parallel$ is the electron–wave coupling parameter, $\mu\approx\gamma^{-2}$ is the inertial bunching parameter,[4] γ is the relativistic mass factor of the electrons, $\beta_\parallel$ is the particle translational velocity, β_{gr} is the group velocity of the phase-matched wave,

$$C=\left(\frac{eI_0}{mc^3}\frac{\lambda^2\mu\kappa^2}{8\pi\gamma S}\right)^{1/3}$$

is the gain parameter (Pierce parameter), I_0 is the beam current, S is the wave norm, and $\alpha(z)$ is the coefficient of wave coupling at Bragg structures[4,5] ($\alpha=\alpha_0$ inside the mirrors and $\alpha=0$ in the regular part of the cavity).

For an initially unmodulated electron beam we have for the boundary conditions on entry to the interaction space at $Z=0$

$$\theta(Z=0)=\theta_0\in[0;2\pi),\qquad \left(\frac{\partial}{\partial Z}+\beta_\parallel^{-1}\frac{\partial}{\partial\tau}\right)\theta(Z=0)=-\Delta, \tag{4}$$

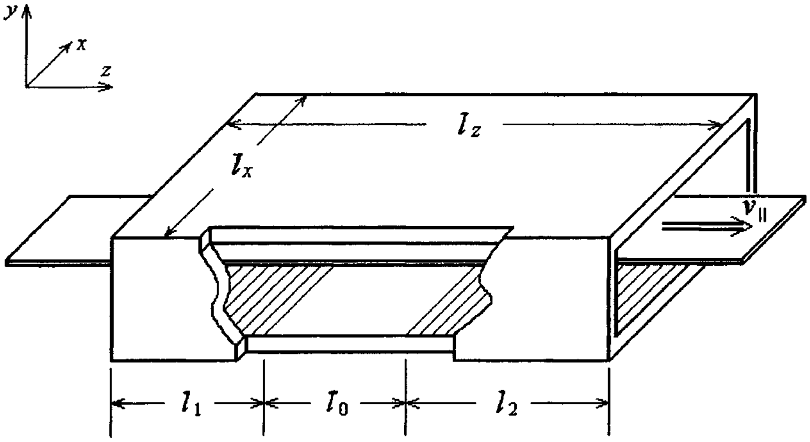

FIG. 1. Schematic of free electron laser with two-mirror Bragg cavity (*1*) and ribbon electron beam (*2*).

where $\Delta=(\bar{\omega}-h(\bar{\omega}))v_\parallel-\Omega_b)/\bar{\omega}C$ is the initial mismatch between the electrons and the wave, and Ω_b is the bounce frequency of the electron oscillations.

As the boundary conditions for the partial wave fields, we have the absence of any external electromagnetic energy fluxes incident on the system:

$$A_+(Z=0)=0,\quad A_-(Z=L_z)=0, \tag{5}$$

$L_z=(l_1+l_0+l_2)\bar{\omega}C/c$, and also the constraint that the electric field at the metal side walls of the cavity is zero:

$$A_\pm(X=0)=0,\quad A_\pm(X=L_x)=0. \tag{6}$$

This last constraint allows us to expand the fields as Fourier series,

$$A_\pm(X,Z,\tau)=\sum_{m=1}^{\infty} a_m^\pm(Z,\tau)\sin(2\pi mX/L_x),$$

and to consider each term in the series as the mode of a rectangular waveguide with a corresponding number of variations of the field over the transverse index.

The results of simulating the evolution of the transverse profile of the radiation field for various normalized cavity widths and electron fluxes are given in Figs. 2 and 3. In these calculations we assumed that the electron flux occupies half the cavity width. The cavity width was varied with the current density per unit length kept constant and was given by the dimensionless parameter L_x. For the oscillator system investigated experimentally the gain parameter is $G\approx 0.003$. All the other geometric dimensions of the systems are close to the experimental conditions.[1,2] The simulation shows that when the width of the system is fairly small, $L_x\leqslant 5$ (Fig. 2a), the output profile and spectrum of the radiation correspond to the excitation of a dominant mode with one transverse variation of the field. As the transverse dimensions of the cavity increase but the longitudinal dimensions and the wave coupling parameter remain constant, the radiation spectrum becomes more complicated. In addition to the dominant mode, this spectrum also contains a fairly significant component caused by the excitation of other modes with a large number of variations along the transverse coordinate. Nevertheless,

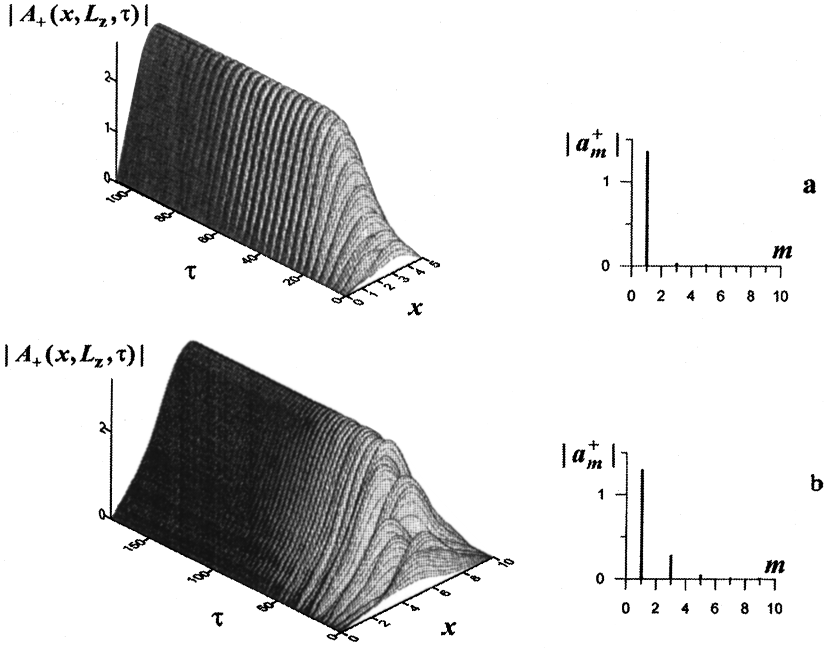

FIG. 2. Evolution of the spatial distribution of the amplitude of the output signal $|A_+(x,L_z,\tau)|$ and the mode composition of the radiation a_m^+ in the cw lasing regime for $L_x=5$, $\Delta=1$ (a) and $L_x=10$, $\Delta=0.8$ (b) ($L_1=1.4$, $L_0=2.4$, $L_1=0.8$, and $\alpha=0.5$).

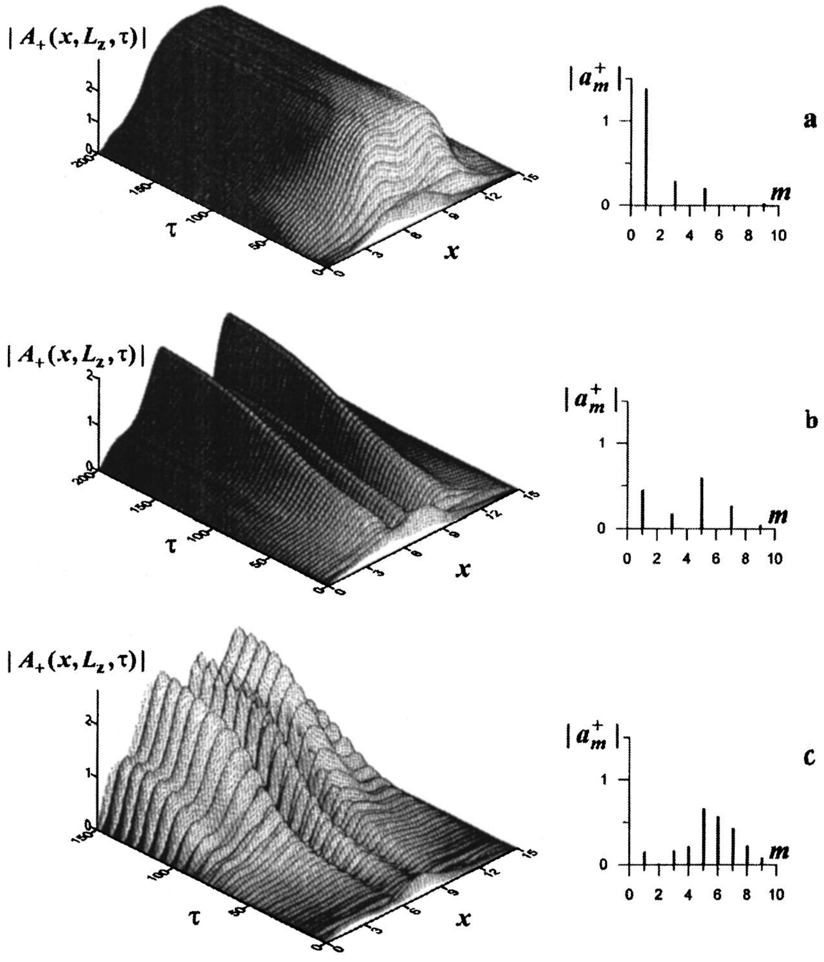

FIG. 3. As Fig. 2 for $L_x = 15$ and various mismatches: a — $\Delta = 0.8$, b — $\Delta = 1.5$, and c — $\Delta = 2$.

in a certain range of parameters the spectrum and output profile of the radiation exhibit steady-state behavior (Figs 2, 3a, and 3b). In this range of parameters we can talk of the excitation of a supermode, i.e., a mode composed of several cold waveguide modes. Since the phases of the modes are intercorrelated, this radiation can be regarded as spatially coherent. We also note that if the mismatch parameter Δ is fixed, a completely fixed phase distribution $\varphi = \arg(A_+)$ is established over the cavity exit aperture.

The transverse radiation profile was varied by varying the mismatch parameter, i.e., by varying the average particle energy in the electron beam. For example, for $\Delta = 0.8$, as can be seen from Fig. 3a, most of the energy is concentrated in a mode with a single longitudinal variation of the field and the radiation output profile is single-humped. However, increasing this parameter Δ to 1.5 has the result that the profile becomes more complicated, for example three-humped (Fig. 3b). In this case, the radiation spectrum clearly reveals the $m = 5$ mode for which the drift angle is more favorable for this Δ. Note also that there is a range of mismatches in which periodic self-modulation of the output radiation profile occurred for a given injection current and system geometry (Fig. 3c). An increase in the wave coupling coefficient at the Bragg gratings also gave rise to self-modulation. For example, for the coupling coefficient $\alpha = 1.3$ self-modulation was observed when the dimensionless width of the system was $L_x = 10$.

Summarizing the results of this analysis, we can conclude that it is fundamentally possible to obtain cw spatially coherent lasing for the oversize parameter $l_x/\lambda \approx 50$ obtained under the experimental conditions, which can be achieved by optimizing the wave coupling coefficient at the Bragg grating and selecting the mismatch. The output radiation will take the form of a supermode, which may be represented as a set of cold cavity modes with fixed amplitudes and phases. In this connection, it is relevant to carry out detailed experimental investigations of the radiation profile of the FEL oscillator mentioned at the beginning. This should allow us to make a comparison with the results of the simulation and determine the degree of spatial coherence of the radiation.

[1] M. A. Agafonov, A. V. Arzhannikov, N. S. Ginzburg, N. Yu. Peskov, S. L. Sinitsky, and A. V. Tarasov, in *Proceedings of the 11th International Conference on High Power Particle Beams*, Prague, Czech Republic, 1996, Vol. 1, p. 213.

[2] M. A. Agafonov, A. V. Arzhannikov, N. S. Ginzburg, V. G. Ivanenko, P. V. Kalinin, S. A. Kuznetsov, N. Yu. Peskov, and S. L. Sinitsky, IEEE Trans. Plasma Sci. **26**, 531 (1998).

[3] N. S. Ginzburg, N. Yu. Peskov, A. D. R. Phelps, G. R. M. Robb, and A. S. Sergeev, IEEE Trans. Plasma Sci. **24**, 770 (1996).

[4] V. L. Bratman, G. G. Denisov, N. S. Ginzburg, and M. I. Petelin, IEEE J. Quantum Electron. **QE-19**, 282 (1983).

[5] N. F. Kovalev, I. M. Orlova, and M. I. Petelin, Izv. Vyssh. Uchebn. Zaved. Radiofiz. **11**, 783 (1968).

Translated by R. M. Durham

TECHNICAL PHYSICS LETTERS VOLUME 25, NUMBER 3 MARCH 1999

Influence of charged particles on the fullerene formation process

D. V. Afanas'ev, G. A. Dyuzhev, and V. I. Karataev

A. F. Ioffe Physicotechnical Institute, Russian Academy of Sciences, St. Petersburg

(Submitted October 27, 1998)
Pis'ma Zh. Tekh. Fiz. **25**, 35–40 (March 12, 1999)

The influence of charged particles on the process of fullerene formation is determined. Systematic experiments are used to show that the presence of carbon ions in the fullerene formation zone substantially increases the fullerene content in the soot. *© 1999 American Institute of Physics.* [S1063-7850(99)00703-X]

In many respects, the reasons for the highly efficient formation of fullerenes in an arc discharge remain unclear,[1] and thus some systematic experiments are needed to obtain the information that will stimulate new ideas about this problem. The aim of the experiments described in the present paper was to identify the influence of charged particles in the fullerene formation process. Many authors hold the view that this influence is insignificant and consider an arc discharge merely as an efficient source of carbon vapor. Accordingly, direct experiments to determine the influence of charged particles on the fullerene formation process seem to us to be highly relevant.

It has long been known[2] that direct heating of a graphite rod to temperatures at which appreciable vaporization occurs is extremely difficult because of combustion of the rod. For our experiments, rf heating of graphite in a helium atmosphere is also unsuitable because of the possible formation of an rf discharge. Thus, we prepared a special apparatus shown schematically in Fig. 1.

A long graphite container *1* with a thermal bridge *2* was screwed into a water-cooled current inlet *3*. A movable 6 mm diameter graphite rod *4* was positioned inside the container on the axis. An arc discharge was struck between the rod *4* and the bottom of the container *1*, with the latter acting as the anode. The arc heated part of this bottom surface to temperatures at which a considerable amount of graphite vaporized from its outer surface. The vaporized material was collected at a water-cooled collector *5*. A water-cooled baffle *6* was provided to completely eliminate any carbon vapor from the inner cavity of the container *1* from reaching the collector *5*.

The device was placed in a vacuum chamber which was evacuated before the discharge and then filled with helium at 70 Torr. The soot collected from the collector *5* was analyzed using a high-resolution, time-of-flight mass spectrometer.[3]

Three types of experiments were carried out:

1. No potential difference was applied between the container *1* and the collector *5*, i.e., the graphite underwent purely thermal vaporization in unionized helium.
2. A low-current discharge was struck between the container and the collector, with the collector *5* as the anode and the bottom of the container as the cathode.
3. A low-current discharge was struck between the container and the collector with the container *1* as the anode.

In all these experiments the bottom of the container was heated by an "internal" arc discharge with a current $I=240$ A at a voltage of ~ 24 V. Thus, in all cases the rate of vaporization of the carbon was approximately the same.

The first experiments were carried out with the distance between the container *1* and the collector *5* equal to $d \sim 7$ mm. Under these conditions the mass spectrometric data for the experiments indicate that the content of all types of fullerenes in the soot was less than 10^{-3}–10^{-2}%. This result agrees with the results report ed in Refs. 4 and 5, where it was demonstrated experimentally that in both an arc discharge and in a gas burner the fullerene formation zone is separated from the carbon vapor source by a quite specific distance.

Thus, in the subsequent experiments the distance between the container and the collector was set at 20 mm to obtain the following results.

In the first type of experiments, the graphite vaporized purely thermally, as we have noted. The area of the heat spot on the bottom of the container which appeared at an internal arc current of 240 A, was $\sim 0.5\,\mathrm{cm}^2$ and the erosion rate was $\sim 5\times 10^{-6}$ g/s which corresponded to a graphite surface temperature $T \sim 3000$ K. Under these conditions, a run of several minutes sufficed to obtain soot of adequate mass for analysis without the bottom of the graphite container burning through.

Figure 2a shows a mass spectrum of this soot sample. The presence of fullerene C_{60} can be reliably identified from the spectrum, but it is difficult to determine the absolute values of the fullerene content α in the soot by means of mass-spectrometric techniques. All we can safely say is that $\alpha \sim 0.1\%$.

Keeping the heating of the graphite container constant, we struck a low-current ($I=10$ mA) discharge between the bottom of the container (cathode) and the soot collector (anode). In this case, the discharge current was provided by thermal emission from the heated cathode. Thus, the discharge voltage was $U \sim 60$ V. No changes in the mass spectra were identified compared with pure thermal vaporization. The spectra clearly show a C_{60} peak and the content is $\alpha \sim 0.1\,\%$. This result would seem to indicate that the presence of charged particles in the bulk has no influence on the fullerene formation process, but this is not the case.

In the third series of experiments the polarity of the electrodes was reversed so that the anode was now the bottom of

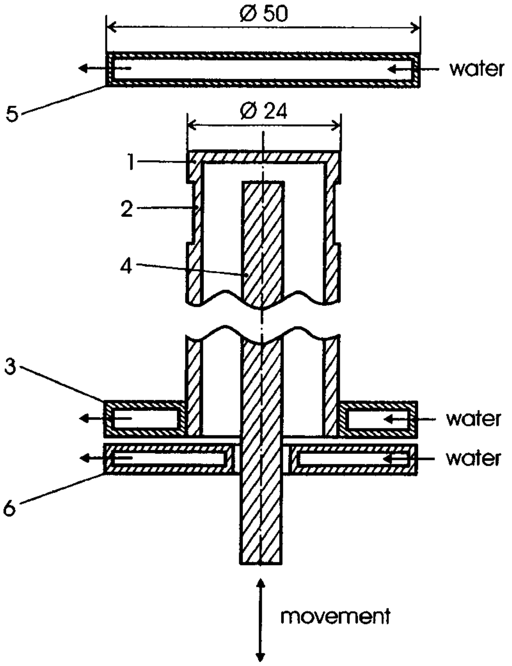

FIG. 1. Schematic of apparatus: *1* — graphite container, *2* — thermal bridge, *3* — water-cooled current inlet, *4* — graphite rod, *5* — water-cooled soot collector, and *6* — water-cooled baffle.

the container from which the carbon vaporized. For this case the low-current discharge ($I\sim 10$ mA) is a classical glow discharge (voltage between electrodes $U=230$ V) complicated by the vaporization of carbon from the anode. A mass spectrometric analysis of the soot showed that the intensity of the C_{60} peak increased substantially (Fig. 2b) and the content of fullerenes in the soot reached $\alpha\sim$ 2–3%.

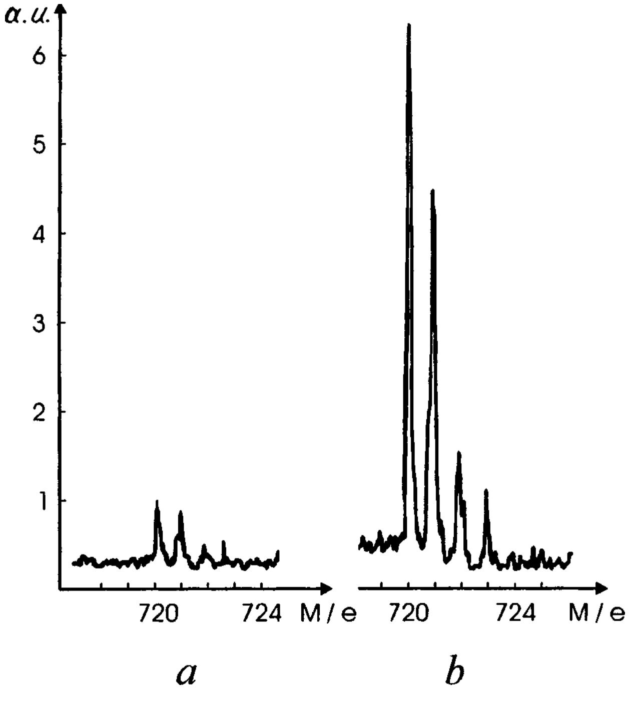

FIG. 2. Typical mass spectra of soot samples: a — pure thermal vaporization of graphite, b — vaporization of graphite from anode of glow discharge.

This substantial difference between the experimental results can be explained if we recall the characteristics of the potential distribution in low-current discharges. If carbon vaporizes from the cathode, some of the vaporized carbon atoms (in low-current discharges the degree of ionization is usually $\sim 10^{-5}$–10^{-7}) are ionized near the cathode by electrons emitted from the cathode and accelerated by the cathode potential drop. Most of the carbon ions formed in the cathode layer are returned to the cathode by the electric field and recombine at the surface. In addition, carbon ions formed in the discharge column as a result of volume ionization also diffuse to the cathode under the action of the electric field. Thus, in the anode region of the plasma where the fullerenes are mainly formed, the concentration of carbon ions is low and they do not have any significant influence on the fullerene formation process.

The situation is different when carbon vaporizes from the anode. A positive anode potential drop is usually established in a glow discharge, which accelerates the electron flux from the plasma to the anode. In helium with a copper cathode the normal cathode drop is $U_c=177$ V (Ref. 6). The experimental voltage between the electrodes was $U_a=230$ V. Since the potential drop across the plasma of a positive column is usually low, in our case the positive anode drop is clearly fairly large, $U_a\sim 50$ V. The carbon atoms vaporized from the anode are ionized by the electron flux accelerated at the anode drop. The product ions are delayed by the electric field of the anode layer, and all enter the plasma where the electric field forces them to diffuse to the soot collector. Thus, in this case the concentration of ions in the fullerene formation zone should be substantially higher.

These experiments have therefore demonstrated fairly convincingly that if the fullerene formation zone contains a sufficient quantity of charged particles, the fullerene formation efficiency is enhanced substantially.

Note that in all these experiments the carbon vapor concentration was low (erosion rate $\sim 10^{-5}$ g/s). In an arc discharge the carbon concentration is several orders of magnitude higher (the rate of anode erosion under optimum conditions for fullerene formation is usually $\sim 10^{-3}$ g/s) but in an arc the plasma concentration is substantially higher than in a glow discharge. Thus, in our view, the presence of charged particles must be taken into account when studying the various mechanisms for fullerene formation in an arc plasma.

We also note that in an arc discharge the fullerene formation process was found to depend markedly on whether the carbon vapor originated from the cathode ($\alpha\sim 0$) or from the anode ($\alpha\sim 8\%$) (Ref. 7).

The authors thank A. A. Bogdanov for assistance with the experiments and discussions on the reasons for these results.

This work was carried out as part of the Russian Scientific-Technical Program ''Fullerenes and Atomic Clusters,'' Project No. 98056.

[1] G. Dyuzhev, Mol. Mater. **7**, 61 (1996).

[2] E. Ryschkewitsch, Z. Electrochem. Ang. Phys. Chem. **3**(2), 54 (1925).

[3] B. A. Mamyrin, V. I. Karataev, D. V. Shmikk, and V. A. Zagulin, Zh. Éksp. Teor. Fiz. **64**, 82 (1973) [Sov. Phys. JETP **37**, 45 (1973)].

[4] G. A. Dyuzhev and V. I. Karataev, Fiz. Tverd. Tela. (St. Petersburg) **36**, 2795 (1994) [Phys. Solid State **36**, 1528 (1994)].

[5] K. N. Homann, Lambda Highlights No. 43 (1994).

[6] Yu. P. Raĭzer, *Gas Discharge Physics* (abridged transl., Springer-Verlag, New York, 1991; Russ. original, Nauka, Moscow 1987).

[7] D. V. Afanas'ev, I. O. Blinov, A. A. Bogdanov *et al.*, Zh. Tekh. Fiz. **67**(2), 125 (1997) [Tech. Phys. **42**, 234 (1997)].

Translated by R. M. Durham

TECHNICAL PHYSICS LETTERS VOLUME 25, NUMBER 3 MARCH 1999

Topological birefringence and combined Rytov–Magnus effect

A. V. Volyar, V. Z. Zhilaĭtis, T. A. Fadeeva, and V. G. Shvedov

Simferopol State University

(Submitted July 3, 1998)
Pis'ma Zh. Tekh. Fiz. **25**, 41–46 (March 12, 1999)

It is shown that the symmetry properties of the locally isotropic inhomogeneous medium of an optical fiber cause circular and linear topological birefringence. The circular birefringence δn_C in graded-index fibers is $\sim(\lambda/\rho)^2$ (where λ is the wavelength and ρ is the core radius), while the linear birefringence is $\delta n_L \sim (\lambda/\rho)^3$. This topological birefringence is characterized not only by the polarization basis (as in crystals for example) but also by the magnitude and sign of the topological charge of the guided vortex. This topological birefringence forms the basis of the instability of the fiber *IV* vortex and is observed experimentally as the combined Rytov–Magnus effect. © *1999 American Institute of Physics.* [S1063-7850(99)00803-4]

The birefringent properties of a locally isotropic layered medium, i.e., shape birefringence,[1] are caused by a difference in the boundary conditions for the normal and tangential components of the TE and TM modes. In the guiding medium of stepped multimode optical fibers, shape birefringence is observed as a difference in the polarization corrections $\delta\beta$ to the propagation constants $\tilde{\beta}$ of the azimuthally symmetric, linearly polarized TE and TM modes.[2] However, for optical fibers with a smooth (graded) refractive index profile $n(r)$, in particular for parabolic fibers, the polarization corrections $\delta\tilde{\beta}_{\mathrm{TE}}$ and $\delta\tilde{\beta}$ are the same in the first approximation of perturbation theory.[2] This gives the impression that no shape birefringence occurs in graded-index fibers. Nevertheless, Liberman and Zel'dovich[3] used WKB methods to analyze the propagation of rays in a locally isotropic, smoothly varying medium and showed that the linear birefringence is of the order $\delta n_L \sim (\lambda/a)^2$ (where a is the characteristic scale of the variations), whereas the circular birefringence is given by $\delta n_C \sim \lambda/a$. In what follows we wall assume that during the propagation process linear birefringence transforms right circular polarization with the helicity $\sigma_z = +1$ into left circular polarization with $\sigma_z = -1$. Circular birefringence does not change the circular polarization state ($\sigma_z = \mathrm{const}$), but the propagation velocities of the $\sigma_z = +1$ and $\sigma_z = -1$ waves are different. This discrepancy between the results forces us to conclude that: 1) either the approximation used in Ref. 2 is inadequate to describe linear birefringence (shape birefringence) or 2) the processes in optical fibers are not described using WKB methods. The aim of the present paper is to study linear and circular birefringence processes in few-mode fibers.

We shall first analyze the propagation of guided *CV* vortices, TE and TM modes in optical fibers with a graded refractive index profile $n^2(R) = n_{\mathrm{co}}^2(1-2\Delta f(R))$, where Δ is the profile height, $f(R)$ is the profile function, $R = r/\rho$, ρ is the core radius, and n_{co} is the refractive index of the core. In Ref. 4 we showed that the polarization correction $\delta\beta$ to the propagation constant $\tilde{\beta}$ is the average of the spin–orbit interaction operator $\hat{\mathbf{V}}$. For parabolic fibers ($f(R) = R^2$) the polarization corrections to $\tilde{\beta}$ for the TE and TM modes are the same ($\delta\tilde{\beta}_{\mathrm{TE}} = \delta\tilde{\beta}_{\mathrm{TM}}$). However, this result was obtained assuming that in a weakly guiding fiber ($\Delta \to 0$) spin–orbit interaction changes the propagation constant to $\beta = \tilde{\beta} + \delta\beta$, but the fields of the natural modes remain unchanged, $\mathbf{e} = \tilde{\mathbf{e}}$ (where $\tilde{\mathbf{e}}$ is the field of the natural modes in the scalar approximation $\Delta \approx 0$) (Ref. 2).

We expand the electric field of the natural fiber mode $\mathbf{e}$ in powers of Δ:

$$\mathbf{e} = \tilde{\mathbf{e}}_{|\Delta=0} + \Delta \mathbf{e}^{(1)} + \Delta^2 \mathbf{e}^{(2)} + \dots . \tag{1}$$

We can show that if we confine ourselves to the first two terms in expression (1), the polarization correction $\delta\beta$ is given by

$$\delta\beta = \delta\tilde{\beta} + 2\Delta^2 A \int_S\!\!\int [\mathbf{e}^{(1)} \boldsymbol{\nabla} f : \boldsymbol{\nabla} \tilde{\mathbf{e}}^* + \mathbf{e}^{(1)*} \boldsymbol{\nabla} f : \nabla \tilde{\mathbf{e}}] dS, \tag{2}$$

where $A^{-1} = (2V)/(\rho\sqrt{2\Delta}) \int_S\!\!\int (\tilde{\mathbf{e}}^* \cdot \mathbf{e} + \tilde{\mathbf{e}} \cdot \mathbf{e}^*) dS$, S is the area of the fiber cross section, and V is the waveguide parameter. The value of $\delta\tilde{\beta}$ is of order Δ. For an axisymmetric medium ($\partial f/\partial\varphi = 0$) the correction field $\mathbf{e}^{(1)}$ is determined from the equations:

$$\left[\partial_R^2 + \frac{1}{R}\partial_R - \frac{1}{R^2} + \tilde{U}^2 - V^2 f + \frac{1}{R^2}\partial_\varphi^2\right] e_r^{(1)} - \frac{2}{R^2}\partial_\varphi e_\varphi^{(1)}$$
$$= 2\partial_R f \partial_R \tilde{e}_r + 2\partial_R^2 f \tilde{e}_r + \frac{4\rho V}{(\sqrt{2\Delta})^3}\delta\tilde{\beta}\tilde{e}_r ,$$
$$\left[\partial_R^2 + \frac{1}{R}\partial_R - \frac{1}{R^2} + \tilde{U}^2 - V^2 f + \frac{1}{R^2}\partial_\varphi^2\right] e_\varphi^{(1)} + \frac{2}{R^2}\partial_\varphi e_r^{(1)}$$
$$= \frac{2}{R}\partial_R f \partial_\varphi \tilde{e}_r + \frac{4\rho V}{(\sqrt{2\Delta})^3}\delta\tilde{\beta}\tilde{e}_\varphi . \tag{3}$$

The solution of these equations for the fields of *CV* vortices and for the TE and TM modes is given in Table I. It can be

TABLE I. Corrections to the electric fields and propagation constants for CV vortices, and TM and TE modes of an optical fiber.

	$\kappa=+1\,l\geqslant 1$ $\sigma=\pm 1$ $\kappa=-1\,l>1$ $CV^{\kappa\sigma}_{\sigma l}$	$\kappa=-1\,l=1$ TM	$\kappa=-1\,l=1$ TE
$\tilde{e}_r$	$\frac{1}{\sqrt{2}}\tilde{F}_l e^{i\sigma(l+\kappa)\varphi}$	$\tilde{F}_1$	0
$\tilde{e}_\varphi$	$\frac{i\kappa\sigma}{\sqrt{2}}\tilde{F}_l e^{i\sigma(l+\kappa)\varphi}$	0	$\tilde{F}_1$
$e_r^{(1)}$	$\frac{1}{\sqrt{2}}F_l^{(1)} e^{i\sigma(l+\kappa)\varphi}$	$F_1^{(1)}$	0
$e_\varphi^{(1)}$	0	0	0
$\delta\beta(f=R^2)$	$-\kappa(l+\kappa)\frac{(\sqrt{2\Delta})^3}{2\rho V}$	0	0
$\delta\beta^{(1)}(f=R^2)$	$-\kappa(l+1)(l+3\kappa)\frac{(\sqrt{2\Delta})^5}{2\rho V^2}$	$-2\frac{(\sqrt{2\Delta})^5}{\rho V^2}$	0

For the profile $f=R^2$:$\tilde{F}_l=R^l\exp(-VR^2/2)$,
$F_l^{(1)}=R^{l+2}\exp(-VR^2/2)$.

seen that for parabolic fibers the polarization corrections $\delta\beta^{(1)}$ for the TE and TM modes are different ($\delta\beta^{(1)}_{\mathrm{TE}}=0$). This means that the fields of the TE and TM modes in parabolic fibers are phase mismatched. When the fiber is excited by circularly polarized light, the TE and TM modes combine to form a topologically inhomogeneous IV vortex.[5] The field of the IV vortex contains the partial vortices $|+1,-1>$ and $|-1,+1>$, which cannot exist independently. In a parabolic fiber the IV vortex is structurally stable in the $\delta\tilde{\beta}$ approximation. In a stepped fiber the IV vortex is structurally unstable, and during the propagation process beats occur between the $|+1,-1>$ and $|-1,+1>$ partial vortices.

The results given in Table I imply that in a parabolic fiber ($V=3.6$ and $\rho=3.5\,\mu$m) the signs of the topological charge and the helicity in a IV vortex are transformed over the distance $\Lambda\approx 67$ m. This change in the state of the IV vortex field is equivalent to the action of the effective linear topological birefringence of the TE and TM modes:

$$\delta n_L=\frac{(\sqrt{2\Delta})^3}{4\pi^3 n_{\mathrm{co}}^2}\left(\frac{\lambda}{\rho}\right)^3. \tag{4}$$

For the parameters of a parabolic fiber given above the linear birefringence is $\delta n_L\approx 2.35\times 10^{-8}$.

The difference in the signs of the topological charge and the helicity of the partial IV vortices was taken into account in the derivation of Eq. (4). In classical crystal optics the linear birefringence δn_L is characterized only by the polarization basis (by the sign of σ or the orientation of the x and y components of the vector **e**). For locally isotropic optical fibers the value of δn_L is characterized by two indices l and σ and generally has a topological nature.[4] Thus, the linear birefringence of locally isotropic few-mode fibers may be called topological birefringence.

It can be seen from Table I that the zeroth polarization correction $\delta\tilde{\beta}$ for circularly polarized CV vortices is almost two orders of magnitude higher than the first polarization correction. However, the correction only changes the phase of the CV vortex, while the topological charge and the polarization remain constant. In addition, the polarization corrections $\delta\tilde{\beta}$ for homogeneous $|\sigma l,\sigma>$ and inhomogeneous $|\sigma l,-\sigma>$ vortices differ. Consequently, these vortices are subjected to circular birefringence. From Table I we find that the topological circular birefringence of CV vortices is given by

$$\delta n_C=\frac{\sigma l\Delta}{8\pi^2 n_{\mathrm{co}}}\left(\frac{\lambda}{\rho}\right)^2. \tag{5}$$

For parabolic fibers with the parameters given above we find $\delta n_L\approx 2.7\times 10^{-6}$. Thus, in parabolic fibers the circular and linear birefringence differs by two orders of magnitude.

On the basis of the experimental results reported in Ref. 5 from the beat length of the IV vortex field we find that the linear topological birefringence in stepped fibers is $\delta n_L\approx 1.4\times 10^{-6}$, i.e., the linear birefringence and circular birefringence in stepped fibers are of the same order of magnitude.

Note that when the circularly polarized CP_{11} mode is excited in stepped fibers, conversion of the orbital and spin angular momenta is observed,[6] which shows up experimentally as a systematic replacement of the Rytov–Vladimirskiĭ effect by the Magnus optical effect (the combined Rytov–Magnus effect). In this case, the linear and circular birefringence mechanism acts simultaneously. Thus, the combined Rytov–Magnus effect is based on the topological birefringence of light in optical fibers.

Topological birefringence has already been observed in essentially multimode fibers,[7] having an order of magnitude of 10^{-6}, and appearing experimentally as angular splitting of the wave caustics. In the field of a linearly polarized LP mode in a few-mode fiber topological birefringence[8] is manifest in the creation and annihilation of circularly polarized C^+ and C^- disclinations.

[1] M. Born and E. Wolf, *Principles of Optics*, 4th ed. (Pergamon Press, Oxford, 1969; Nauka, Moscow, 1973, 720 pp.)

[2] A. W. Snyder and J. D. Love, *Optical Waveguide Theory* (Methuen, London, 1984; Radio i Svyaz, Moscow, 1987, 656 pp).

[3] V. S. Liberman and B. Ya. Zel'dovich, Phys. Rev. E **49**, 2389 (1994).

[4] A. V. Volyar, V. Z. Zhilaĭtis, and V. G. Shvedov, Pis'ma Zh. Tekh. Fiz. **24**(20), 87 (1998) [Tech. Phys. Lett. **24**, 827 (1998)].

[5] A. V. Volyar, T. A. Fadeeva, and Kh. M. Reshitova, Pis'ma Zh. Tekh. Fiz. **23**(5), 70 (1997) [Tech. Phys. Lett. **23**, 198 (1997)].

[6] A. V. Volyar and T. A. Fadeeva, Pis'ma Zh. Tekh. Fiz. **23**(23), 59 (1997) [Tech. Phys. Lett. **23**, 927 (1997)].

[7] A. V. Volyar, Yu. N. Mitsaĭ, V. I. Myagkov, and T. A. Fadeeva, Pis'ma Zh. Tekh. Fiz. **20**(3), 48 (1994) [Tech. Phys. Lett. **20**, 111 (1994)].

[8] A. V. Volyar and T. A. Fadeeva, Pis'ma Zh. Tekh. Fiz. **23**(2), 20 (1997) [Tech. Phys. Lett. **23**, 57 (1997)].

Translated by R. M. Durham

TECHNICAL PHYSICS LETTERS VOLUME 25, NUMBER 3 MARCH 1999

Dielectric properties of single crystals of lead barium scandoniobate solid solutions

I. P. Raevskiĭ, V. V. Eremkin, V. G. Smotrakov, E. S. Gagarina, and M. A. Malitskaya

Research Institute of Physics, Rostov State University, Rostov-on-Don

(Submitted September 2, 1998)
Pis'ma Zh. Tekh. Fiz. **25**, 47–52 (March 12, 1999)

It has been established that the concentration dependence of the temperature T_m of maximum permittivity ε corresponding to the ferroelectric phase transition in crystals of $\mathrm{Pb}_{1-x}\mathrm{Ba}_x\mathrm{Sc}_{0.5}\mathrm{Nb}_{0.5}\mathrm{O}_3$ solid solutions does not saturate in the range $0<x<0.6$, unlike in the ceramic. However, the broadening of the maximum of ε is similar in both crystals and ceramics. The frequency dependence of T_m is described by the Vogel–Fulcher law, which can relate the strong broadening of the phase transition in solid solutions to the appearance of properties typical of dipole glasses. © *1999 American Institute of Physics.* [S1063-7850(99)00903-9]

The ferroelectric solid solution ceramics of lead barium scandoniobate $\mathrm{Pb}_{1-x}\mathrm{Ba}_x\mathrm{Sc}_{0.5}\mathrm{Nb}_{0.5}\mathrm{O}_3$ (PBSN) have recently attracted increasing attention both as a potentially useful base for developing electrooptic and capacitor materials[1,2] and as a model for studying the broadening of phase transitions.[3,4] However, available data on the $T-x$ phase diagram and the nature of the phase transition broadening in these solid solutions are incomplete and very contradictory. In particular, no clear explanation has been given for the abrupt suppression of the concentration dependence of the temperature T_m of maximum permittivity ε observed for $x>0.3$–0.4, which corresponds to the ferroelectric phase transition. The extremely strong broadening of the maxima of $\varepsilon(T)$ observed for compositions with a high Ba content is also unexplained. One possible reason for this may be the presence of a concentration gradient of the components in the ceramic grains[2] as a result of the difficulty of fabricating ceramics of equilibrium PBSN solid solutions because of the substantial difference in the reactivities of $\mathrm{PbSc}_{0.5}\mathrm{Nb}_{0.5}\mathrm{O}_3$ (PSN) and $\mathrm{BaSc}_{0.5}\mathrm{Nb}_{0.5}\mathrm{O}_3$ (BSN). In order to achieve an equilibrium state, the temperature and firing time of the ceramic must be increased, which increases the probability of vacancy formation in the lead. The aim of the present paper is to study the dielectric properties of single crystals of PBSN solid solutions and compare these with the properties of ceramics fabricated by hot pressing at high temperatures[2] for which departure from euilibrium of the composition, and lead defects are considerably less likely to have any influence than in ceramics prepared by the usual firing process.

Transparent yellow crystals of $\mathrm{Pb}_{1-x}\mathrm{Ba}_x\mathrm{Sc}_{0.5}\mathrm{Nb}_{0.5}\mathrm{O}_3$ with $0\leqslant x\leqslant 0.58$ (from data obtained using a Camebax-Micro scanning microscope microanalyzer) of predominantly isometric shape and measuring 1–2 mm were grown by mass crystallization. The method of growing and analyzing the crystals was similar to that described in Ref. 5. An x-ray structural analysis showed that the reduced parameter of the rhombohedrally distorted perovskite crystal cell increases approximately linearly with increasing x. Unlike the ceramic,[2] the x-ray diffraction patterns showed no line broadening compared with PSN, which indirectly indicates that these solid solutions are in equilibrium.

As in ceramics, an increase in the Ba content decreases the temperature T_m corresponding to maximum $\varepsilon(T)$ in PBSN crystals, increases its degree of broadening, and reduces the maximum ε_m (Figs. 1 and 2). The $\varepsilon_m(x)$ and $T_m(x)$ dependence for the crystals and the ceramic is fairly similar. The saturation of $T_m(x)$ observed in the ceramic for $x>0.4$ is evidently attributable to the nonequilibrium of the

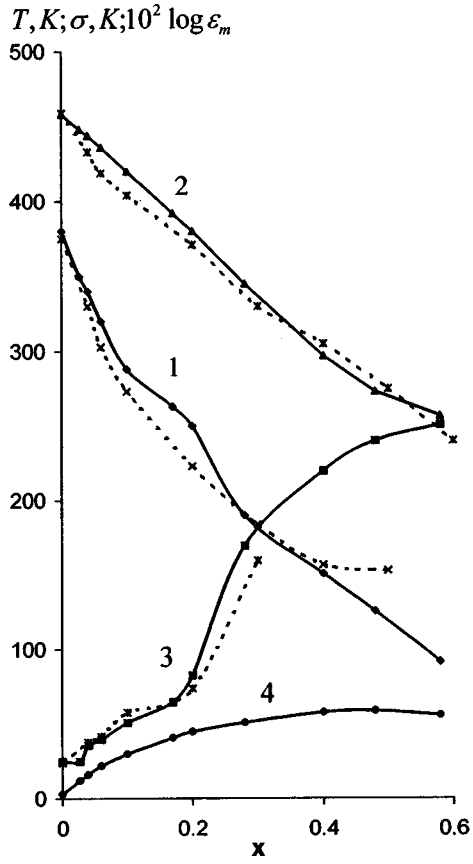

FIG. 1. Concentration dependence of the temperature T_m of maximum permittivity ε (*1*), maximum permittivity ε_m (*2*), the phase broadening parameter σ (*3*), and the difference between T_m at 1 kHz and the Vogel–Fulcher temperature T_0 (*4*) for $\mathrm{Pb}_{1-x}\mathrm{Ba}_x\mathrm{Sc}_{0.5}\mathrm{Nb}_{0.5}\mathrm{O}_3$ solid solutions. Solid curves — crystals and dashed curves — ceramics (from data given in Ref. 2).

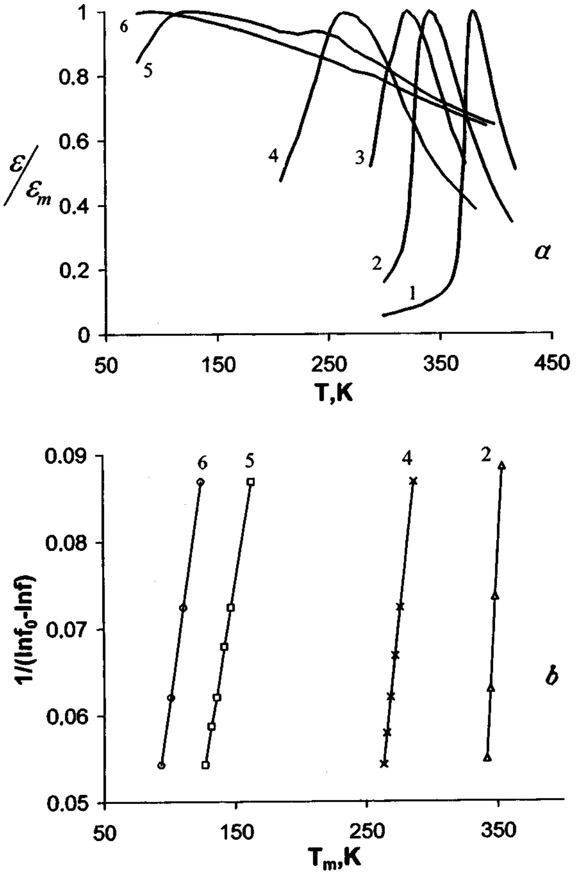

FIG. 2. Temperature dependence of $\varepsilon/\varepsilon_m$ (ε_m is the maximum of ε) for crystals of $Pb_{1-x}Ba_xSc_{0.5}Nb_{0.5}O_3$ solid solutions, measured at 1 kHz: *1* — $x=0$, *2* — $x=0.04$, *3* — $x=0.06$, *4* — $x=0.17$, *5* — $x=0.48$, and *6* — $x=0.58$; b — dependence of $(\ln f_0-\ln f)^{-1}$ on T_m for $Pb_{1-x}Ba_xSc_{0.5}Nb_{0.5}O_3$ crystals, illustrating the Vogel–Fulcher law. The notation is the same as in Fig. 2a.

ceramic samples. The curves of $\varepsilon(T)$ for some crystals with a high Ba content reveal small additional anomalies above the temperature of the principal maximum. These may well be caused by the formation of a thin surface layer containing a larger quantity of PSN compared with the bulk at the instant when the mother flux combines. The existence of similar layers was noted previously for crystals of other solid solutions.[5]

Above T_m the temperature dependence of ε for most crystals is accurately described by[6]

$$\frac{1}{\varepsilon}=\frac{1}{\varepsilon_m}+\frac{(T-T_m)^2}{2\varepsilon_m\sigma^2}. \tag{1}$$

It can be seen from Fig. 1 that the transition broadening parameter σ for the crystals is similar to that for ceramics determined using data from Ref. 1.

The values of T_m for the crystals increased as the frequency f of the measuring field increased. The dependence of T_m on f is accurately described by the Vogel–Fulcher law:

$$f=f_0\exp[-E/k(T_m-T_0)], \tag{2}$$

where f_0 is the frequency of attempts to overcome the potential barrier E, k is the Boltzmann constant, and T_0 is the Vogel–Fulcher temperature, which is interpreted as the temperature for ''static freezing'' of the electric dipoles or a transition to the dipole glass state.[7,8] In PBSN crystals we find $f_0=(0.5\text{–}1)\times10^{11}$ Hz, which is similar to the values observed in other ferroelectric relaxors.[8–10] For pure PSN the values of T_0 are close to T_m (Refs. 9 and 10) but as x increases, the difference T_m-T_0 increases, reaching ≈ 60 K for $x\approx 0.4$ and then remaining approximately constant. Note that approximately the same difference T_m-T_0 is observed in crystals of the classical ferroelectric relaxor $PbMg_{1/3}Nb_{2/3}O_3$ (Ref. 8).

Thus, the saturation of the dependence $T_m(x)$ observed in ceramics of PBSN solid solutions for $x>0.4$ is evidently caused by the presence of concentration inhomogeneities. However, the strong broadening of the phase transition observed both in the ceramic and in the crystals is probably caused by the appearance of properties typical of dipole glasses (frustration in the crystal lattice of the ferroelectric in which nonferroelectric material is dissolved[2,11]). This explanation is also supported by the results of studying the thermal conductivity of PBSN ceramics.[3]

This work was partially supported by the Russian Fund for Fundamental Research, Project No. 96-02-17463.

[1] M. Ya. Dambekalne, K. Ya. Borman, A. R. Sternberg *et al.*, Izv. Ross. Akad. Nauk, Ser. Fiz. **57**(3), 78 (1993).

[2] I. P. Pronin, T. Ayazbaev, N. V. Zaĭtseva *et al.*, Neorg. Mater. **32**, 1528 (1996).

[3] M. Fahland, G. Mattausch, and E. Hegenbarth, Ferroelectrics **168**, 9 (1995).

[4] C. Malibert, B. Dkhil, J. M. Kiat *et al.*, J. Phys.: Condens. Matter **9**, 7485 (1997).

[5] V. Eremkin, V. Smotrakov, E. Gagarina *et al.*, J. Korean Phys. Soc. **32**, S1597 (1998).

[6] V. V. Kirillov and V. A. Isupov, Izv. Akad. Nauk SSSR, Ser. Fiz. **35**, 2602 (1971).

[7] K. H. Fisher, Phys. Status Solidi B **116**, 357 (1983).

[8] D. Viehland, S. Jang, L. E. Cross *et al.*, Philos. Mag. B **64**, 335 (1991).

[9] F. Chu, N. Setter, and A. K. Tagantsev, J. Appl. Phys. **74**, 5129 (1993).

[10] F. Chu, I. M. Reaney, and N. Setter, Ferroelectrics **151**, 343 (1994).

[11] V. A. Isupov, Izv. Akad. Nauk SSSR, Ser. Fiz. **54**, 1131 (1990).

Translated by R. M. Durham

Some new possibilities for using waves from cylindrical emitters

I. A. Kolmakov

(Submitted April 17, 1998)
Pis'ma Zh. Tekh. Fiz. **25**, 53–56 (March 12, 1999)

An analysis is made of a new principle for flow rate measurements based on using cylindrical emitters, which has significant advantages over known methods. The advantages of using these emitters in waveguide technology are discussed. © *1999 American Institute of Physics.* [S1063-7850(99)01003-4]

The present paper examines two aspects of using cylindrical acoustic waves: in flow metering and in waveguide information transmission technology, where the scope of these fields of applied acoustics can be expanded considerably.

In order to determine the flow rate accurately, it is necessary to know the flow velocity simultaneously at all points in the radial cross section of a channel (pipe) containing the medium being measured, and equally importantly the initial information on the flow must be measured with a high degree of accuracy. Satisfying the first condition can eliminate the fundamental procedural error inherent in all known methods of measuring the flow rate. The importance of the second condition requires no explanation.

Below we analyze a new principle for measuring flow rates using waves generated by a cylindrical emitter, which eliminates the first error and also satisfies the second condition, since the measured quantity is the frequency, which can be measured extremely accurately. For conciseness this new measurement principle is demonstrated for a specific flow meter, shown schematically in Fig. 1 together with the wave field formed in the medium inside the channel.

A short exciting pulse is supplied from an electric signal generator *G* to a cylindrical wave emitter *R*, causing the emission of a cylindrical wave. As the wave propagates, the wavefront section near the end becomes curved and forms a cone near the *Z* longitudinal axis. This conical wavefront is responsible for the formation of a longitudinal component of the momentum (or depending on the wave amplitude, of the motion of the medium as an entity), which excites plane waves traveling from the region with the cylindrical waves along the *Z* axis. After being reflected from the *Z* axis, a diverging cylindrical wave forms, which after reaching the channel wall and being reflected from it, again travels toward the *Z* axis. At the instant of reflection from the longitudinal axis, two plane waves again form, traveling in opposite directions, and so on. Thus, as a result of a single external pulse, a series of cylindrical reverberation (damped) waves forms in the medium inside the channel accompanied by the same number of plane waves traveling in the same direction. If the medium in the channel is stationary, the end plane of the cylindrical wave a_1Oa_1 is also stationary. If the medium moves with the velocity *U*, the end plane a_1Oa_1 will move at the same velocity.

In Fig. 1 the trajectories of the cylindrical waves in the a_1Oa_1 plane are shown arbitrarily for $U=0$ by the line Oa_1; for $U\neq 0$ they are shown by the lines $a_1 1$, $1a_2$, $a_2 2$, $\ldots$, where the point *O* corresponds to the time $t_0=0$, *1* corresponds to t_1, and so on, i.e., $t_1=R_0(c+U)^{-1}$, $t_2=t_1+2R_0(c+U)^{-1}$, $\ldots$, where R_0 is the channel radius and *c* is the velocity of sound in the medium. Thus, a detector *A* will record the signal frequency Doppler-modified by the flow of the medium, that is, the source of information-carrying signals, i.e., the region with the cylindrical waves which generates plane waves along *Z*, moves with the flow at the velocity *U* relative to the signal detector *A*. The frequency recorded by the detector is

$$\nu=\frac{c}{2R_0}\left(1+\frac{U}{c}\right), \tag{1}$$

and the volumetric flow rate through the channel with allowance for Eq. (1) is given by

$$Q=\pi R_0^3(2\nu-\nu_0), \quad \nu_0=cR_0^{-1}. \tag{2}$$

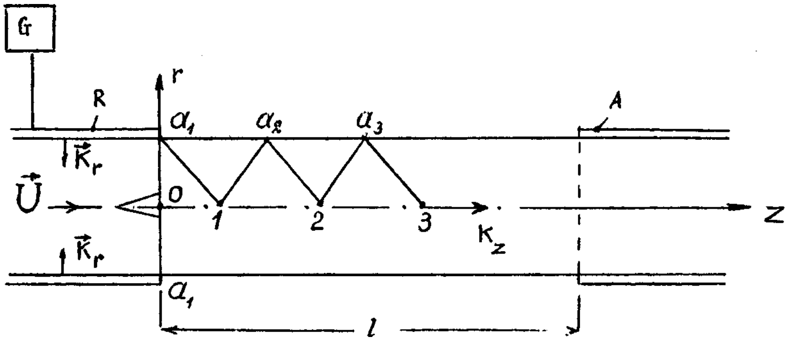

FIG. 1.

The mass flow[1] $Q_m = Q\rho$ can also be measured at the same time as the volumetric flow rate. In this case, the frequency ν is used to determine c and the amplitude of the acoustic pressure P' at the transducer (which acts alternately as emitter and detector of the cylindrical waves) is used to determine ρ' as $c = (P\rho^{-1})^{1/2}$. The most important advantage of using cylindrical waves is that for each single propagation of a cylindrical wave from the channel wall to the longitudinal axis the velocities are automatically integrated at all points in the radial cross section of the flow channel, since at any point in the cross section the wave deflection is exactly equal to the instantaneous value of the flow velocity at this point. Consequently, the time of arrival of the cylindrical wave on the axis will correspond to the exact value of the flow velocity U (flow rate) and the frequency recorded by the detector will therefore determine the exact value of the flow rate. The feasibility of this principle of flow rate measurements has been confirmed experimentally.

Another efficient application of cylindrical transducers is in information transmission technology using acoustic waveguides. We shall briefly discuss the advantages in these cases. As we know,[2,3] the use of normal waves as information carriers is impeded by the existence of sets of critical frequencies in waveguides. Plane waves excited by cylindrical emitters are not normal, and so critical frequencies do not exist for these waves (as was also confirmed experimentally). Thus, by using cylindrical emitters it is possible to transmit information in any frequency range. The motion of the medium in the waveguide creates an additional channel for frequency control. Moreover, some experiments can be carried out exclusively using cylindrical emitters, for example, in cases where counterpropagating plane waves interact when trains of primary waves occupy the entire inner region of the channel between the emitters.

[1] L. D. Landau and E. M. Lifshits, *Fluid Mechanics*, 2nd ed. (Pergamon Press, Oxford, 1987) [Russ. original, later ed., Nauka, Moscow 1988, 733 pp.]

[2] M. A. Isakovich, *General Acoustics* [in Russian], Nauka, Moscow (1973), 495 pp.

[3] M. B. Vinogradova, O. V. Rudenko, and A. P. Sukhorukov, *Wave Theory* [in Russian], Nauka, Moscow (1979), 387 pp.

Translated by R. M. Durham

TECHNICAL PHYSICS LETTERS VOLUME 25, NUMBER 3 MARCH 1999

Flexural vibrations of semiconductor wafers in the presence of a pulsed thermal excitation source

A. M. Orlov, A. A. Skvortsov, A. V. Pirogov, and V. A. Frolov

Ulyanovsk State University

(Submitted April 16, 1998)
Pis'ma Zh. Tekh. Fiz. **25**, 57–63 (March 12, 1999)

An analysis is made of the action of current pulses on a metal film lying on a semiconductor wafer. It is shown that the passage of current pulses of amplitude $(1–7)\times 10^{10}$ A/m^2 and duration 50–200 μs across aluminum tracks excites sound. Experimental dependences of the energy of the flexural vibrations as a function of the duration and amplitude of the pulsed action were obtained. It was observed for the first time that the melting of a metal–semiconductor contact is accompanied by an abrupt increase in the energy of the flexural vibrations of the wafer. © *1999 American Institute of Physics.* [S1063-7850(99)01103-9]

The operation of semiconductor devices and integrated circuits is usually associated with increased thermal and mechanical loads which reach critical values[1,2] at elevated current densities. Any abrupt changes in the current loads give rise to thermal shocks which excite various types of mechanical vibrations. However, the influence of contact heating and degradation processes on the spectrum and energy of the vibrations has been very little studied, and as devices become more highly integrated further attention must be given to this issue. Thus, in the present paper we analyze the spectra and energy of the flexural vibrations of silicon wafers when metallized layers of special test structures are subjected to current heating.

Acoustic signals were excited by impacting a 3–10 g steel ball against the surface of the wafer and passing rectangular current pulses of varying amplitude $j=(1–7)\times 10^{10}$ A/cm^2 and duration $\tau=50–200$ μs through aluminum tracks deposited on the surface of a silicon wafer.[3] The substrates were [111]-oriented, phosphorus-doped silicon wafers of resistivity 30 $\Omega\cdot$m. Aluminum films 3.2 μm thick were deposited by electron-beam evaporation at a rate of 2 nm/s at a residual pressure of 4×10^{-4} Pa and substrate temperature 373 K.

The flexural vibrations were detected by a piezocrystal transducer mounted at the edge of the wafer near the main base cut. The transducer was a TsTS-19 piezoceramic wafer of thickness $d=300$ μm and diameter 13 mm, whose natural frequencies ($f_i \geqslant 4$ MHz) were higher than the spectral composition of the signal response. This allowed the frequency characteristic of the medium to be determined using the electrical response $U(t)$ from the transducer, which was fed to an S9-8 storage oscilloscope connected to a computer to record and store the data. The signal was frequency-filtered using a standard fast Fourier transform algorithm in order to expand it into its elementary components. This allowed us to analyze the behavior of isolated harmonics and of the energy W of the flexural vibrations of the wafer, which are related by[4]

$$W=\frac{m}{4}\sum_n A_n^2\omega_n^2, \tag{1}$$

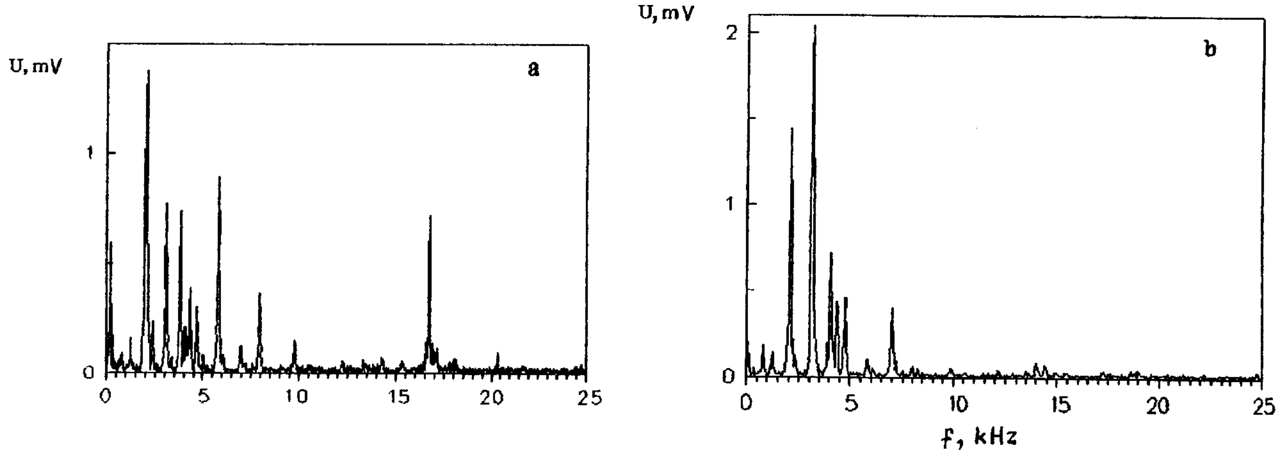

FIG. 1. Spectra of flexural vibrations of a wafer exposed to mechanical (a) and thermal (b) action.

TABLE I. Comparison between theoretical and experimental values of the natural vibration frequencies of a wafer with a clamped edge exposed to mechanical and thermal influences.

Calculated value f_n	981	1836	2356	3216	3904	4189	5543	7138	7836	9695	16098
Mechanical action f_n, Hz	1270	2051	2393	3076	3809	4321	5786	6960	7935	9741	16750
Thermal action f_n, Hz	1270	2051	2344	3174	3857	4297	5859	6980	7788	–	–

where m is the mass of the wafer, and ω_n and A_n are all the natural frequencies and amplitudes of the wafer vibrations.

The numerical values of ω_n for a wafer with a clamped edge can easily be calculated using the equation[4]

$$\omega_n = 2\pi f_n = \frac{\pi^2 h}{b^2}\beta_n^2\left[\frac{E}{3\rho(1-\sigma^2)}\right]^{0.5}, \tag{2}$$

if we know the half-thickness h, radius b, density ρ, Young's modulus E, Poisson ratio σ, and the roots of the corresponding characteristic equation β_n.

An analysis of the parameters of the recorded signal under mechanical action revealed a direct proportional relationship between $U(t)$ and the velocity of the vibrations $v(t)$ (Ref. 5). Thus, in our case the energy of the flexural vibrations is proportional to $W \sim \Sigma_n U_n^2$, where U_n are the amplitudes of the harmonics of the experimental spectrum.

For comparison Fig. 1 shows spectra of the signals under mechanical (a) and thermal (current) impact (b) for a wafer with a clamped edge. It can be seen that signals are excited at frequencies between 0.5 and 20 kHz which corresponds to the flexural vibration modes. A comparison between the experimental spectrum and the natural frequencies of the flexural vibrations calculated using Eq. (2) shows good agreement over the entire spectral range (see Table I). This indicates that even negligible current pulses applied to the metallization layers lead to the excitation of flexural vibrations in the wafer. In this case, the generation of sound is caused by the rate of expansion of the heated sections of the medium and is of a thermal nature.[7]

We shall analyze some characteristic features of this process for this particular system. If the power density of the heat sources is given by[7]

$$Q(x,y,z,t) = \mu J(x,y)\exp(-\mu z) f(t), \tag{3}$$

when a silicon wafer is heated by current pulses of duration τ, the inequality $\tau > \tau_a, \tau_\chi$ is satisfied,[6,8] and the components of the stress tensor σ_{RR} have the form[7]

$$\sigma_{RR} = \frac{(4/n^2-3)\alpha a^2 J}{4}(M(\theta) f'(t-R/C_L) + \tau_\mu K(\theta) f''(t-R/C_L)). \tag{4}$$

In Eqs. (3) and (4) $J(x,y)$ is the power released at the contact in watts per square meter per second, μ is the absorption coefficient in reciprocal meters, $f(t)$ is a function of time which determines the pulse shape, R is the distance between the sound source and the observation point, χ is the thermal diffusivity of the semiconductor, C_L and C_t are the propagation velocities of the longitudinal and transverse waves, $n = C_L/C_t$, $\tau_a = a/C_L$, and $\tau_\chi = \chi/C_L$ are the characteristic delay times of the acoustic waves, and a is the contact area.

It is easy to see that the shape of the acoustic pulse depends on the envelope of the current pulse and on the power of the radiation pulse. Thus, the switchon and switchoff times of the current pulse when the rates of change in the temperature of the heated volume are greatest, should be determining factors for the onset of vibrations. Moreover,

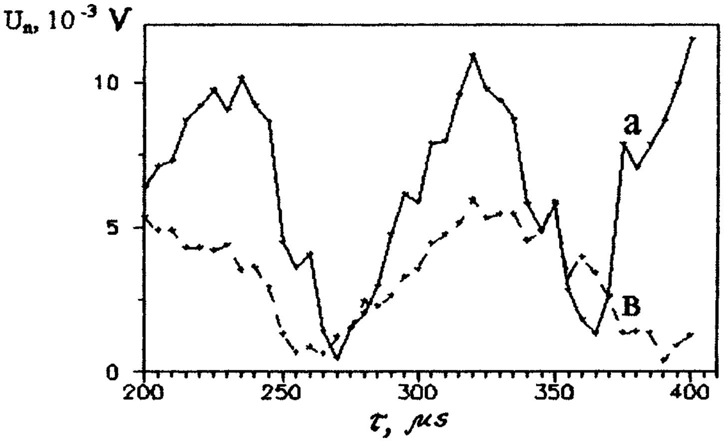

FIG. 2. Amplitude of the harmonics (a — 11.25 kHz, b — 7.788 kHz) as a function of the duration τ of a current pulse of amplitude $j = 3\times10^{10}$ A/m^2.

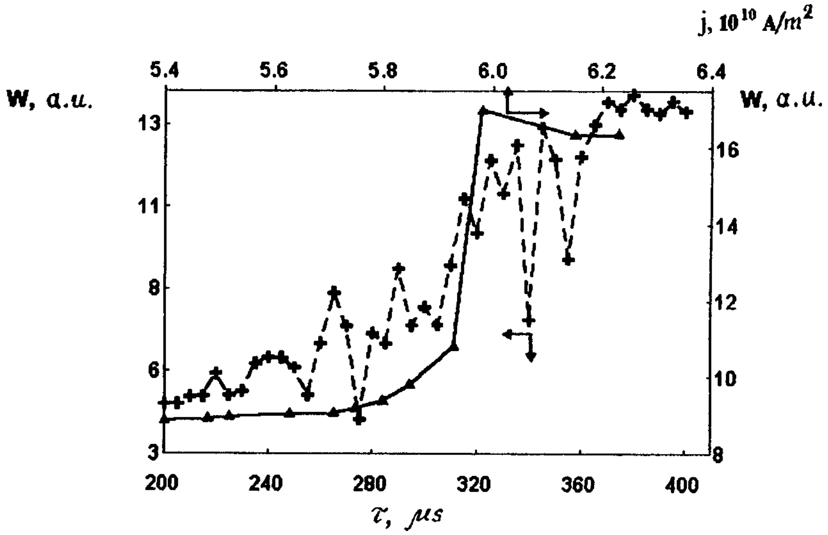

FIG. 3. Energy of flexural vibrations as a function of the current pulse duration for constant $j=3\times10^{10}$ A/m^2 (dashed curve) and as function of the pulse amplitude for a constant duration $\tau=110\,\mu$s (solid curve).

the interaction between the wave packets at the instants of heating and cooling for various τ should have a substantial influence on the amplitude of the harmonic components forming the signal.

A detailed analysis of the spectra under the action of current pulses in the range $\Delta\tau=170$–$420\,\mu$s confirms this. Moreover, the dependence is periodic with a characteristic time $T_i=1/f_i$ (Fig. 2). Extreme values of the amplitude of the fixed harmonic f_i are observed for durations $\tau_i=(k+1)/(2f_i)$, where $k=1,3,5,\dots$ correspond to minima and $k=2,4,6,\dots$ correspond to maxima. Thus, as a result of a change in the contribution of the corresponding harmonics, the dependence of the flexural vibration energy on τ should be oscillatory. This is clearly confirmed by the experimental curve $W(\tau)$ (dashed curve in Fig. 3) in the range of durations $\Delta\tau=250$–$380\,\mu$s. A general increase in W with increasing τ is clearly caused by changes in the power density of the heat sources Q.

An increase in Q as far as critical values must affect the vibration energy. In fact, when $j=6\times10^{10}$ A/m^2 is reached the curve of $W(j)$ (solid curve in Fig. 3) shows an abrupt increase in the energy W. Independent investigations of the degradation process of aluminum–silicon contacts[3] show that at current densities $j\geqslant j_\kappa$ (τ is fixed) the aluminum film fuses and contact melting occurs in an Al–Si system.[9] This promotes an abrupt increase in the energy of the flexural vibrations as a result of a stepwise change in the electrical resistivity of the metallized Al layer during fusion.[10] The higher the current density $j_\kappa\sim1/(\tau_\kappa)^{0.25}$, the earlier the metallized layer begins to be damaged.

This work was financed by a grant from the State Committee for Higher Education ''Degradation processes in multilayer thin-film silicon structures.''

[1] A. S. Oates, J. Appl. Phys. **70**, 5369 (1991).
[2] H. J. Frost, Mater. Charact. Mater. Charact. No. 4, 257 (1994).
[3] A. M. Orlov, B. M. Kostishko, and A. A. Skvortsov, Poverkhnost': Rentgen. Sinkhrotron. Neĭtron. Issl., No 1, 80 (1997).
[4] V. I. Lependin, *Acoustics* [in Russian], Nauka, Moscow (1978), 342 pp.
[5] V. I. Domarskas and R.-I. Yu. Kazhis, *Piezoelectric Transducers for Control and Measurement* [in Russian], Mintis, Vilnius (1975), 255 pp.
[6] *Handbook of Physical Quantities*, edited by I. S. Grigor'ev and E. Z. Meĭlikhov [in Russian], Energoatomizdat, Moscow (1991), 1232 pp.
[7] L. M. Lyamshev, *Radiation Acoustics* [in Russian], Nauka, Moscow (1989), 240 pp.
[8] A. S. Okhotin, A. S. Pushkarskiĭ, and V. V. Gorbachev, *Thermophysical Properties of Semiconductors* [in Russian], Atomizdat, Moscow (1972), 187 pp.
[9] A. M. Orlov, B. M. Kostishko, and A. A. Skvortsov, Neorg. Mater. **31**, 668 (1993).
[10] D. R. Vilson, *Structure of Liquid Metals and Alloys* [in Russian], Metallurgiya, Moscow (1972), 246 pp.

Translated by R. M. Durham

TECHNICAL PHYSICS LETTERS VOLUME 25, NUMBER 3 MARCH 1999

Self-developing, glycerin-containing, thick-layer bichromated gelatin as a medium for recording volume holograms

Yu. N. Denisyuk, N. M. Ganzherli, I. A. Maurer, and S. A. Pisarevskaya

A. F. Ioffe Physicotechnical Institute, Russian Academy of Sciences, St. Petersburg

(Submitted July 16, 1998)
Pis'ma Zh. Tekh. Fiz. **25**, 64–69 (March 12, 1999)

The synthesis of layers of glycerin-containing, self-developing bichromated gelatin between 100 and 500 μm thick is described and the holographic characteristics of this light-sensitive material are discussed. Experimental data obtained by measuring the diffraction efficiency of holograms of two plane waves recorded using a symmetric system for layers of different thickness and various ammonium bichromate concentrations showed that the optimum layers for hologram recording are around 200 μm thick and have an ammonium bichromate concentration of 2–2.5% by weight of dry gelatin. The sensitivity of these layers is 5–10 J/cm^2. © *1999 American Institute of Physics.* [S1063-7850(99)01203-3]

Thick volume holograms, i.e., holograms recorded in light-sensitive layers on the order of a few millimeters thick, have many properties which can be widely used in the development of optical elements for modern optical information processors, in optical memory systems with multiplex recording of information, and so on. Here we report results of experiments to study a thick-layer, self-developing light-sensitive material using glycerin-containing bichromated gelatin.[1]

A type of self-developing layer of bichromated gelatin with glycerin added up to 95% by weight of dry gelatin, having a thickness on the order of 5–10 μm after drying has been described in the literature.[2] The glycerin in these layers acts as a plasticizer and is also used to maintain a certain quantity of water molecules which can develop a latent image because hydrogen bonds are present.

We prepared and investigated self-developing, glycerin-containing layers of bichromated gelatin having a layer thickness of between 100 and 500 μm after drying. The preparation process was similar to the well-known technology for fabricating layers of bichromated gelatin.[3] A melted solution of 6% gelatin was poured onto a glass substrate at 40°C; to this we added up to 95% glycerin and 0.5–4% of ammonium bichromate by weight of dry gelatin. After gelling in a refrigerator for 24 h, the layers were then left for a few days at room temperature, their thickness decreasing by a factor of five or six.

The main holographic characteristics of the layers were determined by recording holograms of two plane waves formed from helium–cadmium laser radiation. The interfering beams propagated symmetrically relative to the normal to the surface of the layers, intersecting at an angle of 14°. The power density of the radiation in the plane of the hologram was on the order of 10 mW/cm^2. The reconstructed wave formed in the first few seconds of recording the hologram. By periodically covering one of the interfering beams and measuring the intensity of the light reconstructed by the hologram, we were able to measure the hologram diffraction efficiency versus the exposure time by reading out holograms at 0.44 μm directly during the recording process.

Figure 1 gives results of measurements of the hologram diffraction efficiency when holograms are read out by helium–cadmium laser radiation during the exposure time for various concentrations of ammonium bichromate and layers of order 200 μm thick. Similar behavior was obtained for layers between 100 and 500 μm thick. Figure 2 gives the maximum attainable diffraction efficiency of holograms of two plane waves plotted as a function of the ammonium bichromate concentration for layers of different thickness when the holograms are read out by 0.44 μm helium–

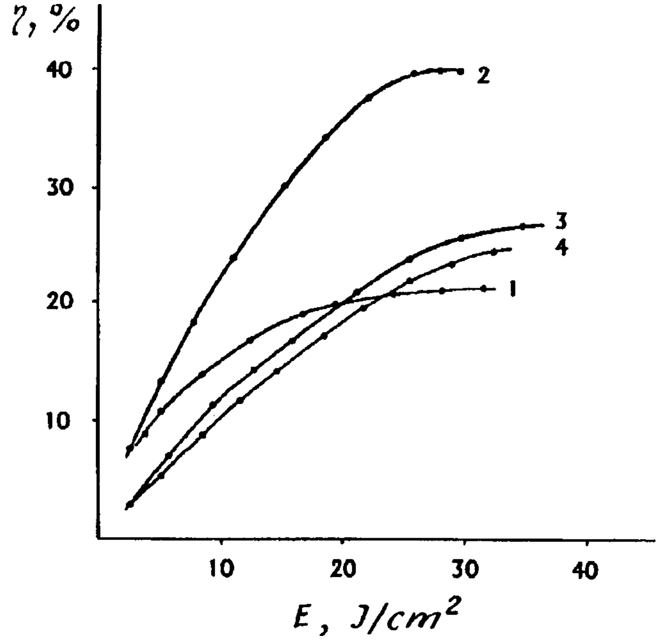

FIG. 1. Diffraction efficiency η of holograms of two plane waves as a function of the exposure E to helium–cadmium laser radiation for layers of bichromated gelatin around 200 μm thick containing various concentrations of ammonium bichromate (percent by weight of dry gelatin): *1* — 1.25, *2* — 2.5, *3* — 3.0, and *4* — 4.0.

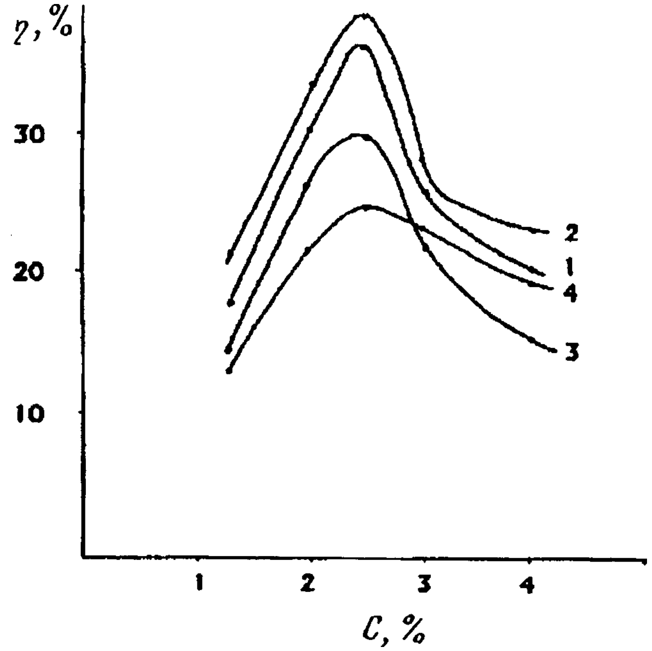

FIG. 2. Maximum attainable diffraction efficiency η as a function of the ammonium bichromate concentration C for layers of varying thickness (in microns): *1* — 150, *2* — 200, *3* — 300, and *4* — 400.

cadmium laser radiation. The highest diffraction efficiencies were obtained for layers of order 200 μm thick. The maximum diffraction efficiency is close to 40% for an average exposure of 30 J/cm^2. From this we can estimate the sensitivity of this thick-layer, glycerin-containing bichromated gelatin to be approximately 5 J/cm^2, which is close to the sensitivity of thick-layer reoxane materials[4] and the gel-like bichromated gelatin proposed by us earlier.[5,6] Applying the Kogelnik coupled wave theory,[7] we can use the experimental data on the hologram diffraction efficiency and the transmissivity and thickness of the layers to estimate the change in the refractive index in layers of bichromated gelatin exposed to the action of helium–cadmium laser radiation. The largest changes in the refractive index for these layers were 0.0001–0.0004.

Helium–neon laser radiation was also used to read out holograms at the Bragg angle during the hologram recording process. Figure 3 gives the maximum attainable hologram diffraction efficiency as a function of the ammonium bichromate concentration for samples of order 200 μm thick using helium–neon (curve *1*) and helium–cadmium (*2*) readout radiation.

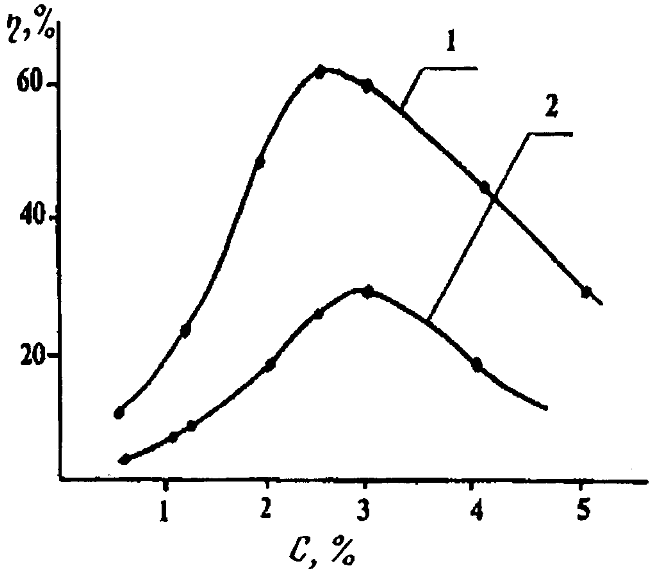

FIG. 3. Maximum attainable hologram diffraction efficiency η as a function of ammonium bichromate concentration C using helium–neon (curve *1*) and helium–cadmium readout radiation (curve *2*) for layers 300 μm thick.

Increasing the angle of intersection of the interfering beams during the hologram recording process reduces the maximum attainable diffraction efficiency to 20%, 6%, and 2% for angles of 20, 30, and 40°, respectively, between the interfering beams. Assuming that a diffraction efficiency of 1% is sufficient, the resolution of the self-developing thick-layer bichromated gelatin may be taken to be 1200 mm^{-1}.

In addition to having the property that a latent image is self-developing because the dried layer of gelation retains some water molecules in complexes with glycerin, the proposed thick-layer light-sensitive material can also store recorded holograms of two plane waves for an almost unlimited time without any significant deterioration in the diffraction efficiency. This light-sensitive material is inexpensive and fairly simple to fabricate.

This work was supported by the Russian Fund for Fundamental Research (Grant No. 97-02-18285) and by the CRDF fund (Grant No. RE2-162).

[1] Yu. N. Denisyuk, N. M. Ganzherli, I. A. Maurer, and S. A. Pisarevskaya, Pis'ma Zh. Tekh. Fiz. **23**(7), 62 (1997) [Tech. Phys. Lett. **23**, 279 (1997)].

[2] V. P. Sherstyuk, A. H. Malov, S. M. Maloletov, and V. V. Kalinkin, Proc. SPIE **1238**, 2101 (1989).

[3] T. A. Shankoff, Appl. Opt. **7**, 2101 (1968).

[4] Yu. N. Denisyuk, N. A. Savost'yanenko, and E. I. Vasil'eva, Opt. Spektrosk. **65**, 244 (1988) [Opt. Spectrosc. **65**, 146 (1988)].

[5] Yu. N. Denisyuk, N. M. Ganzherli, and I. A. Maurer, Pis'ma Zh. Tekh. Fiz. **21**(17), 51 (1995) [Tech. Phys. Lett. **21**, 703 (1995)].

[6] Yu. N. Denisyuk, N. M. Ganzherli, and I. A. Maurer, Opt. Spektrosk. **83**, 341 (1997) [Opt. Spectrosc. **83**, 320 (1997)].

[7] H. Kogelnik, Bell Syst. Tech. J. **48**, 2909 (1969).

Translated by R. M. Durham

Multielement hypersonic piezotransducers with slowly varying parameters for acoustooptic devices

I. S. Nefedov and V. V. Petrov

Saratov State University

(Submitted April 10, 1997; resubmitted November 13, 1998)
Pis'ma Zh. Tekh. Fiz. **25**, 70–75 (March 12, 1999)

The frequency bands of acoustooptic devices can be extended appreciably by using multielement transducers in the form of multielement chains with variable parameters such as the grating step, phase shift per cell, piezolayer thickness, cell impedance, and electrode length of a single element. When the optimum law of variation of the parameters along the transducer length has been found, the law of variation of the angle of inclination of the acoustic wavefront can be accurately matched with the law of variation of the Bragg condition with frequency, which can increase the working frequency band of an acoustooptic device (in particular, a deflector) while maintaining a high diffraction efficiency. In the present paper a relationship obtained earlier to determine the frequency dependence of the structure step, which ensures accurate self-tuning to the Bragg angle, and also a solution of the dispersion equation obtained for one variant of a multielement structure are used to analyze the frequency dependence of the length of isolated electrodes, which determines the inductance of the element, and also the impedance of isolated cells contained in the multielement structure. © *1999 American Institute of Physics.* [S1063-7850(99)01303-8]

In an earlier study Petrov[1] proposed a method of increasing the frequency band of Bragg acoustooptic cells by using multielement transducers with variable parameters including the grating pitch l, electrode length H, which determines the inductance of the elements, phase shift per cell φ_0, cell impedance Z, and also the thickness of the piezoelectric layer. The expression derived by Petrov[1] to calculate the frequency dependence of the structure pitch l, which ensures exact self-tuning of the acoustic beam to the Bragg angle, is given by

$$l=\varphi_m V/2\pi f \sin\{\Theta_{0i}+(-1)^i \arcsin(\lambda_0 f/2n_0 V)\}, \qquad (1)$$

where $\varphi_m=\varphi_0+2\pi m$, m is the number of the spatial harmonic of the acoustic field, V is the velocity of sound in the crystal, Θ_{0i} is the angle of incidence of the optical beam relative to the transducer plane, and i is an index corresponding to one of the two possible directions of incidence of the optical beam relative to the acoustic wavefront. The dependence (1) removes the constraint on the length of the multielement transducer imposed by the need to create a given beam divergence in a particular frequency band to compensate for the mismatch between the frequency variation of the Bragg angle and the angle of inclination of the acoustic wavefront when periodic structures are used. Consequently, a high diffraction efficiency can be achieved over a broad band of acoustooptic interaction frequencies.

For a given frequency dependence of the phase shift per cell $\varphi_0(f)$ we used the dispersion equation obtained with allowance for expression (1) to analyze the behavior of the impedance Z in the frequency band and the electrode length H of each cell in the multielement structure.

A multielement microstripe transducer with variable parameters is analyzed assuming that the pitch of the system varies negligibly over a certain section of the transducer length L, so that in this section the system can be regarded as periodic. This approach allows us to use methods developed in the widely used theory of retarding systems in vacuum electronic devices with extended interaction.[2]

Figure 1 gives a schematic top view of the multielement piezotransducer showing the variable parameters analyzed in the present study. A metal underlayer *1*, a piezoelectric film *2*, and a metal overlayer in the form of a comb structure *3* with varying parameters are successively deposited at the end of a lithium niobate crystal. The thickness of the piezoelectric film varies (increases) from the high-frequency edge of the structure (input to which a microwave signal is applied) toward its low-frequency edge, so that there is a certain range of transducer length L (a moving window) in which the electroacoustic conversion efficiency is highest and which moves along the transducer length L as the working frequency varies within the pass band. This window at each frequency corresponds to the region of the multielement structure which gives exact tuning of the acoustic wavefront at the Bragg angle. The sections of overlap between the underlayer and the comb electrodes comprise plane-parallel capacitors filled with piezoelectric and form isolated transducer elements which excite acoustic vibrations, while the comb electrodes of length H form inductances. Thus, this electrodynamic structure may be represented as a multielement filter chain or a retarding system.

The problem of calculating the characteristics of this type of system can be solved in two stages. In the first stage, a strict electrodynamic formulation and the Fourier–Galerkin method[3] are used to calculate the parameters of a periodic stripe line formed by an array of ideally conducting ribbons,

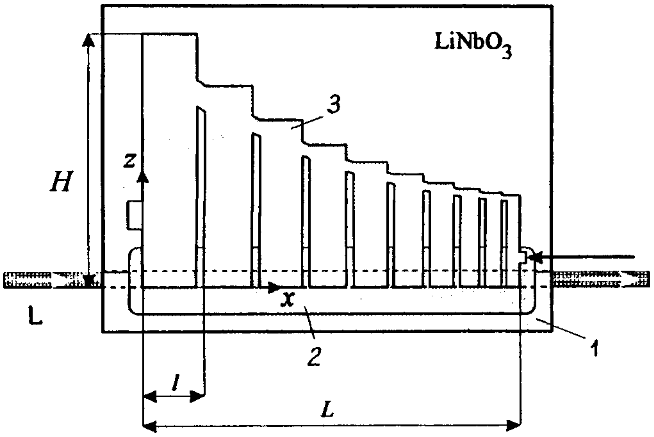

FIG. 1. Multielement electrodynamic structure with variable optimized parameters; X — cut, L — light, HF — microwave signal.

regular along the z axis and periodic along the x axis, located at the interface of the magnetodielectrics.

In the second stage the calculated parameters of the periodic stripe line (quasi-T wave propagation constant $\gamma(\omega,\varphi 0)$ and impedance $Z(\omega,\varphi 0)$) and the conditions at the ends of the pins are used to calculate the behavior of the retarding system using the method of multiconductor lines.[2]

The relationship between the potentials and the currents in the planes $z=0$ and $z=H$ at the ends of pins attached to a busbar ($z=H$) may be written using the transfer matrix of a section of the stripe line (loop) and the input conductance Y of a pin in the periodic stripe line in the plane $z=H$:

$$\begin{bmatrix} U_1(H) \\ I_1(H) \end{bmatrix} = \begin{bmatrix} \cos\gamma_s H & (jZ_s)\sin\gamma_s H \\ (j/Z_s)\sin\gamma_s H & \cos\gamma_s H \end{bmatrix} \times \begin{bmatrix} 1 & 0 \\ Y & 1 \end{bmatrix} \begin{bmatrix} U_2(H) \\ I_2(H) \end{bmatrix}, \tag{2}$$

where γ_s and Z_s are the wave number and the wave impedance of the loop.

Using the Flocquet condition, we obtain from Eq. (2) a system of linear algebraic equations. The condition that its determinant is zero is the equation for the wave dispersion in this periodic structure:

$$\mathrm{Det}\left(\begin{bmatrix} \cos\gamma_s H & (jZ_s)\sin\gamma_s H \\ (j/Z_s)\sin\gamma_s H & \cos\gamma_s H \end{bmatrix} \times \begin{bmatrix} 1 & 0 \\ Y & 1 \end{bmatrix} e^{-j\varphi_0} - \begin{bmatrix} 1 & 0 \\ 0 & 1 \end{bmatrix} \right) = 0. \tag{3}$$

The input impedance $Z(H)=Y^{-1}$ in the plane $z=H$ of a section of the periodic stripe line with wave impedance Z_0 and wave number γ_0 loaded to the resistance $Z_{(0)}$ is given by

$$Z_{(H)} = Z_0 \frac{Z_{(0)} + jZ_0 \tan\gamma_0 H}{Z_0 + jZ_{(0)} \tan\gamma_0 H}, \tag{4}$$

where $Z_{(0)} = -j\,(1/\omega C)$ and C is the capacitance of the piezoelement.

Using the algorithms described above we calculated the electrodynamic characteristics of a quasiperiodic structure with slowly varying parameters. The variation of the phase shift with frequency ($0.5 \geqslant \varphi_0/\pi \geqslant 0.1$) was defined in the frequency range between 7.5 and 11 GHz, and then formula (1) was used to calculate the structure step for which the Bragg condition is satisfied at a given frequency and for a given phase shift. For each step we used a numerical technique to determine the pin length H for which the dispersion equation (3) was satisfied.

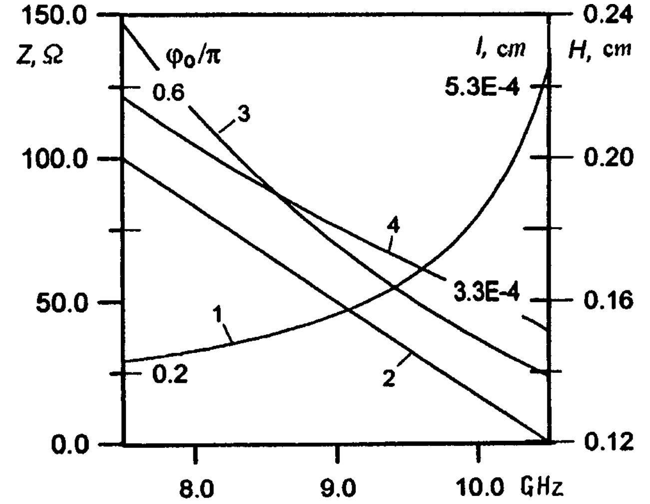

FIG. 2. Frequency dependence of the impedance (*1*), phase shift per cell (*2*), structure step (*3*), and electrode length (*4*).

Figure 2 gives the frequency dependence of the given phase shift per cell φ_0/π and also the dependence of the structure step l, electrode length H, and grating impedance Z calculated for the frequency range 7.5–10.5 GHz. The calculations were made for a zinc oxide piezotransducer located on an X-cut lithium niobate crystal. The angle of incidence of the optical beam was zero relative to the transducer plane (for the index $i=2$, see Ref. 1). However, the variations of the phase shift per cell, which barely influence the shape of the curves $l(f)$ and $H(f)$, may be used to tune the input impedance of the multielement structure to achieve electrical matching between the transducer and the waveguiding line. This calculation example demonstrates the possibility of fabricating a wide-band ($\Delta f = 3$ GHz) acoustooptic Bragg cell in the 3 cm radiowave range using a multielement transducer with variable parameters. In order to make a more comprehensive analysis of the proposed method, it is also interesting to estimate the diffraction efficiency and the possibility of achieving the most planar frequency characteristic by correcting the frequency dependence of the structure step.

---

[1] V. V. Petrov, Pis'ma Zh. Tekh. Fiz. **22**(22), 11 (1996) [Tech. Phys. Lett. **22**, 909 (1996)].

[2] R. A. Silin and V. P. Sazonov, *Retarding Systems* [in Russian], Radio i Svyaz', Moscow (1966).

[3] Yu. V. Gulyaev, A. I. Zhbanov, Yu. F. Zakharchenko *et al.*, Radiotekh. Elektron. No. 12, 2049 (1994).

Translated by R. M. Durham

TECHNICAL PHYSICS LETTERS VOLUME 25, NUMBER 3 MARCH 1999

Size distribution of copper nanoclusters in amorphous carbon

D. V. Kulikov, Yu. V. Trushin, V. S. Kharlamov, and V. I. Ivanov-Omskiĭ

A. F. Ioffe Physicotechnical Institute, Russian Academy of Sciences, St. Petersburg

(Submitted July 16, 1998)
Pis'ma Zh. Tekh. Fiz. **25**, 76–79 (March 12, 1999)

A theoretical analysis is made of the formation of copper nanoclusters in a growing amorphous carbon film. The calculated size distributions of the copper clusters are compared with the experimental data. A numerical estimate is made of various kinetic parameters of copper in amorphous carbon. © *1999 American Institute of Physics.* [S1063-7850(99)01403-2]

Interest in the physics of conducting clusters has been stimulated by their possible application in nano- and microelectronics. Modifying the properties of hydrogenated amorphous carbon (a-C:H) by incorporating metal nanoclusters (such as copper) is of considerable interest because it is possible to vary useful properties of the material. The incorporation of metal nanoclusters also provides additional scope for studying the structure of the amorphous matrix itself.[1,2]

In the present paper we propose a model for the evolution of copper nanoclusters during the growth of a-C:H films by magnetron cosputtering of graphite and copper.[2] This model is used to construct the size distribution function of these clusters which, as will be shown subsequently, agrees satisfactorily with the experimental results.[1,2] A comparison between the model parameters and the experiment can give a numerical estimate of the activation energy for the surface migration of copper.

The fundamental assumptions of the model are as follows:

1. From numerical estimates, we assume that during the film growth process, copper and carbon atoms reach the surface of the film with a low energy insufficient to penetrate inside the sample.

2. Copper atoms can only diffuse over the surface of the film, since the diffusion of copper in the bulk of the sample is negligible. Thus, all the diffusion processes take place during the growth of one or two monolayers of the film.

3. Diffusing copper atoms can form bi-interstitial sites and combine with existing copper clusters, thereby increasing their size. Thus, copper clusters of various sizes exist in the film.

Subject to these assumptions, we can apply the theory of diffusion processes in irradiated solids (see Ref. 3, for example) to write a system of equations which takes these processes into account:

$$\frac{\partial C(t)}{\partial t}=g-\alpha DC^2(t)-\alpha_q DC(t)\int_0^\infty f(R,t)RdR, \qquad (1)$$

$$\frac{dV(t)}{dt}=\frac{d(\pi R^2(t))}{dt}=a^2 I(R)=a^2\alpha_q DR(t)C(t),$$

or

$$\frac{dR(t)}{2}=\frac{a^2}{2\pi}\alpha_q DC(t), \qquad (2)$$

$$\frac{\partial f(R,t)}{\partial t}=W(R)-\frac{\partial}{\partial R}\left[f(R,t)\frac{dR(t)}{dt}\right]$$
$$=\frac{\alpha DC^2(t)}{2a}\bigg|_{R=2a}-\frac{\partial}{\partial R}\left[f(R,t)\frac{a^2}{2\pi}\alpha_q DC(t)\right]. \qquad (3)$$

Here $C(t)$ is the surface concentration of copper, g is the rate at which copper is generated at the surface of the growing film, D is the coefficient of surface diffusion of copper,

$$D=D_0\exp(-\varepsilon^m/kT), \qquad (4)$$

ε^m is the activation energy for surface migration of the copper, $f(R,t)$ is the size distribution function of the copper clusters, i.e., the number of clusters of a particular size per unit volume, V and R are the volume (more accurately, the area, since the clusters are assumed to be planar) and radius of the copper clusters, a is the lattice parameter of the copper, $I(R)$ is the growth rate of the copper clusters, $W(R)$ is the rate of formation of clusters of size R, and α and α_q are geometric parameters for attachment of the copper atoms to clusters.

The system of equations (1)–(3) was solved by computer using the MGEAR program[4] for parameters consistent with those obtained experimentally.[1,2] The unknowns ε^m, α, and α_q were varied during the calculations. As a result, we obtained the size distribution function of the copper clusters for samples with different copper contents (3% and 9%, see Refs. 1 and 2), which are plotted in Fig. 1 together with the experimental results. It can be seen that the calculated and experimental data show satisfactory agreement. The theoretical curves were obtained for the following parameter values: for the sample containing 3% copper — $\alpha_q=2\pi$, $\alpha=2\pi\times0.15\,\text{nm}$, and $\varepsilon^m=0.75\,\text{eV}$; for the sample containing 9% copper — $\alpha_q=6\pi$, $\alpha=6\pi\times0.15\,\text{nm}$, and $\varepsilon^m=0.75\,\text{eV}$. Thus, the geometry of the formation of the copper clusters varies as the copper content in the film varies, which agrees

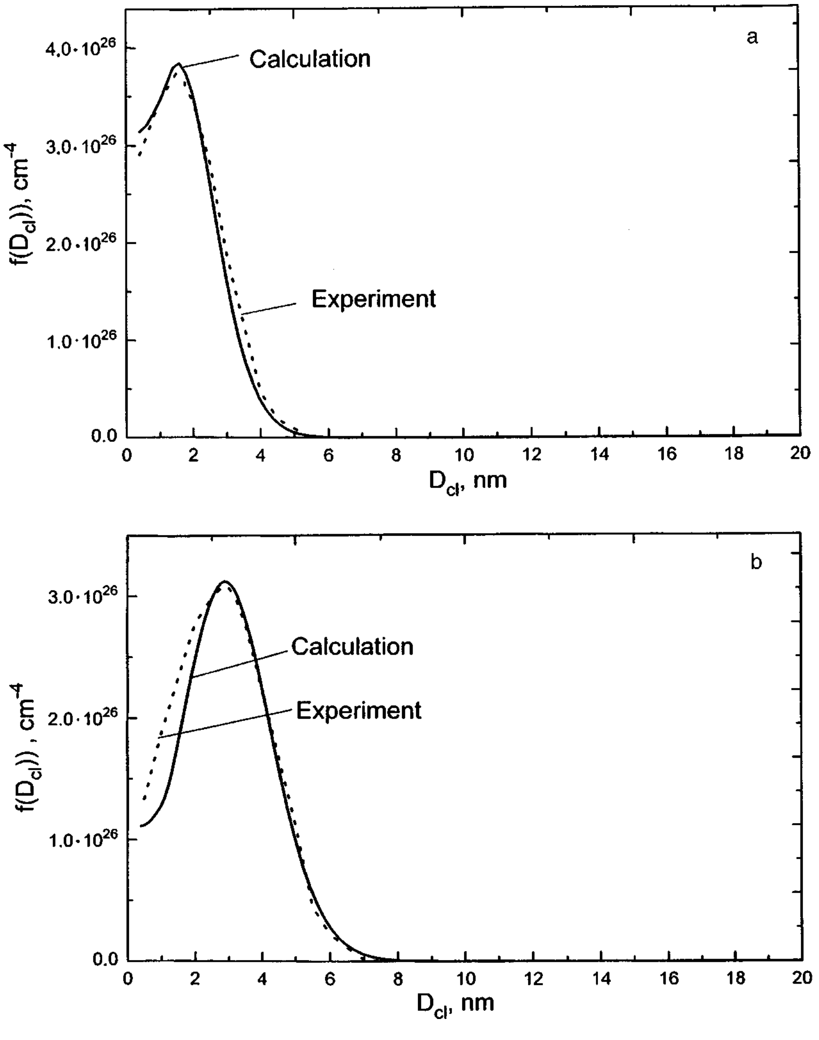

FIG. 1. Calculated and experimental size distribution functions of copper clusters in DLC films with various copper contents: a — 3% and b — 9%.

with the data obtained in Ref. 2, where a fractal dimension was observed for the surface of copper clusters containing more than 4% copper.

To sum up, computer modeling has been used to obtain a size distribution function of copper clusters which agrees satisfactorily with the experimental results. This indicates that the proposed model adequately describes the growth of metal clusters during the formation of an amorphous carbon film by magnetron cosputtering of graphite and copper. The activation energy for the surface migration of copper atoms is estimated numerically.

This work was supported by grants from the Russian Fund for Fundamental Research No. 97-02-18110 and the MNTTs (Project No. 467).

[1] V. I. Ivanov-Omskii, S. G. Yastrebov, A. A. Suvorova, A. A. Sitnikova, and A. V. Tolmachev, J. Chem. Vapor Dep. **5**, 188 (1997).

[2] V. I. Ivanov-Omskii, in *Diamond Based Composites and Related Materials*, edited by M. Prelas *et al.*, NATO ASI Series, Partnership sub-series 3, High Technology, Vol. 38 (Kluwer, Dordrecht, 1997), pp. 171–187.

[3] Yu. V. Trushin, *Theory of Radiation Processes in Metal Solid Solutions* (Nova Science Publishers, New York, 1996, 405 pp.)

[4] D. V. Kulikov, R. A. Suris, and Yu. V. Trushin, Supercond. Sci. Technol. **8**, 303 (1995).

Translated by R. M. Durham

Atomic force/tunneling microscope and its application to the study of dielectric breakdown of a diamond film on silicon

A. V. Ermakov and V. K. Adamchuk

Physics Research Institute, St. Petersburg State University, Petrodvorets

(Submitted August 12, 1997; resubmitted October 12, 1998)
Pis'ma Zh. Tekh. Fiz. **25**, 80–86 (March 12, 1999)

A simple design is proposed for an atomic force microscope where the force of interaction between the tip and the surface of the sample is recorded directly using the piezoceramic of an XYZ-manipulator. The force signal is used as a feedback signal to keep the gap between the tip and the surface constant, and its electrical conductivity is recorded at the same time. Results of modifying the electrical conductivity of a thin diamond film after electrical breakdown are presented. © *1999 American Institute of Physics.* [S1063-7850(99)01503-7]

The scanning tunneling microscope (STM)[1] and the atomic force microscope (AFM)[2] have now been recognized as highly efficient tools for studying surface defects on the atomic scale, although each has its own strictly specific sphere of application.

Tunneling microscopes having a spatial resolution of order 1 Å in the plane of the sample and of order 0.05 Å along the normal to the surface exhibit extremely high sensitivity to point defects on the surface.[3,4] However, the operating principle of the scanning tunneling microscope is based on the electrical conductivity of the surface, and the presence of insulating sections on the surface makes the use of this device completely impossible.

Force microscopes operate on both conducting and dielectric surfaces but are only sensitive to defects substantially larger than point defects, such as steps and multiatomic vacancies.[5,6]

Recently, many different designs of STM and AFM have been developed for specific applications in physics, chemistry, and engineering. Here we propose a principle for a device which can be operated as an AFM or an STM and can also record the tunnel current during scanning when operated as an AFM. The force created between the tip and the surface is recorded by the same piezomanipulator which tracks the Z, Y, and X coordinates. In the practical design of this device, the tip is attached directly to the piezomanipulator and the weak interaction forces between the tip and the surface are recorded using the electrical signal generated in the piezomanipulator as a result of the action of the force.

Figure 1 shows a block diagram of the device. In the AFM mode the device operates as follows. An alternating voltage generator supplies the fundamental mechanical resonance frequency of the piezomanipulator to a piezoceramic plate with the sample attached, which causes weak oscillations of the sample along the Z axis. The oscillations of the tip–sample gap give rise to an oscillating interaction force between the tip and the surface, where the smaller the gap between the sample and the tip, the stronger the interaction force and the oscillation amplitude of this force. Since the tip is rigidly attached to the piezomanipulator, the oscillations of the tip–sample interaction force induce mechanical vibrations at the resonance frequency and an electrical signal in

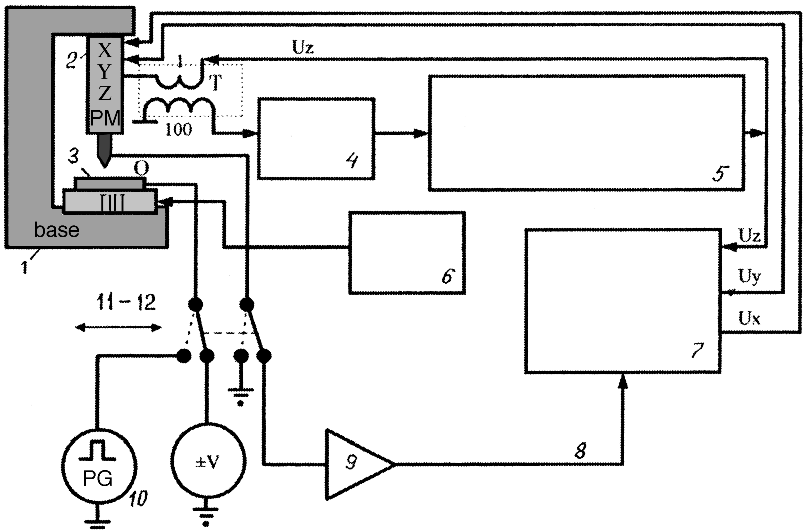

FIG. 1. Block diagram of device: *1* — base, *2* — piezomanipulator, *3* — piezoceramic plate, *4* — low-noise selective amplifier, *5* — unit for controlling displacement along *Z*, *6* — alternating voltage generator, *7* — computer, *8* — tunnel current, *9* — tunnel current amplifier, *10* — pulse generator, *11* — breakdown, and *12* — scanning tunneling microscope.

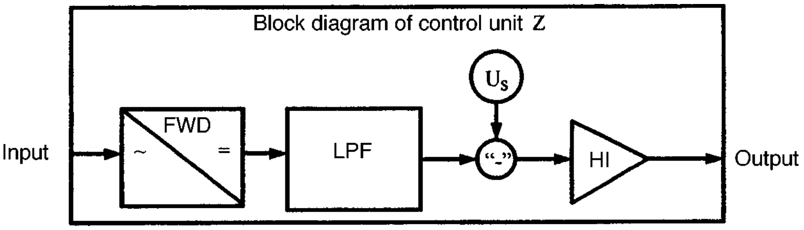

FIG. 2. Block diagram of control unit: FWD – full-wave detector, LPF — low-pass filter, U_s — sample voltage source, "-" — subtraction system, and HI — high-voltage integrator.

the piezomanipulator. This electrical signal is then isolated by a transformer and fed to a unit which controls the displacement of the tip along the *Z* axis.

Depending on the incoming signal, the control unit generates a low-frequency voltage U_Z and supplies this to the piezomanipulator. This voltage controls the tip–sample gap so that the amplitude of the alternating voltage oscillations is kept constant as the tip scans along the surface. In this case, the signal U_Z maps the surface topography. Since the signal generated by the piezoceramic at its resonant frequency is measured in the U_Z signal circuit, frequencies close to the resonant frequency must be eliminated from the U_Z signal. For this purpose, in addition to the usual components of a typical AFM/STM feedback loop (subtraction of a constant level, an integrator, and a high-voltage amplifier), the control unit (Fig. 2) contains an eighth-order low-pass filter with a cutoff frequency of 2 kHz and also uses a full-wave amplitude detector which can suppress the resonant-frequency output signal by several orders of magnitude. In order to distinguish the resonant-frequency signal from the background of the low-frequency signal U_Z, the pass band of the low-noise selective amplifier was limited by a sixth-order bandpass filter in the range 20–30 kHz.

The movement of the tip along the *X* and *Y* coordinates is programmed by computer. When the device is operating in the AFM mode, the tunnel current can be recorded at the same time as scanning. This is accomplished by applying a voltage *V* to the sample from a source. As the tip passes over the electrically conducting sections, a tunnel current is generated which is fed to a computer and used to produce an image. It should be noted that this image will differ from that obtained using a conventional STM design, since the feedback uses the force signal rather than the tunnel current signal. This allows the surface (via the force signal) and the nonuniformities of the electrical conductivity to be recorded simultaneously. If the tunnel current signal is fed to the *Z*-displacement control unit so that the gap between the tip and the sample keeps the tunnel current constant, the device will operate as an STM.

The 2 mm thick piezoceramic plate to which the sample is attached is made of PKR-6 piezoceramic and has a piezoelectric modulus of 2.5 Å/V. The piezomanipulator is a cross-shaped rod 90 mm long made of PKR-7M piezoceramic. The fundamental longitudinal resonance frequency is 25 kHz. The specifications of PKR-7M piezoceramic indicate that its sensitivity to a force at the resonant frequency is 2 V/N. The electrical noise voltage reduced to the transformer input is less than 5 nV, which corresponds to force oscillations of 2.5×10^{-9} N. The maximum scanning field is $200\times200\,\mu$m.

This device was used to modify thin diamond film by dielectric breakdown and to study the resulting surface structure. For this experiment we used 0.2 mm thick silicon wafers with a 200 Å diamond film deposited on the surface. Over the entire scanned area the initial film exhibited no conductivity.

Dielectric breakdown was achieved by connecting the sample to a pulse generator and grounding the tip. We used a tungsten tip fabricated by electrochemical etching. The radius of the tip determined using an electron microscope was $\sim0.3\,\mu$m. The gap between the sample and the tip corresponded to a force of $\sim10^{-8}$ N. By exposing the sample to electrical pulses of varying amplitude and duration and then monitoring the conductivity of the diamond film in a particular section, we established that the threshold breakdown voltage is 60 V, which corresponds to a field of 3×10^6 V/cm. The pulse duration was varied between 0.1 and 10 μs.

It was established by using an electron microscope that the tip shape changes negligibly during breakdown and can be used subsequently for scanning the sample.

Figure 3a shows an image obtained by scanning a section with dielectric breakdowns at four sites in the atomic force mode. The lighter sections of the image are higher. The figure shows that humps ~100 Å high with maximum dimensions of ~800 Å in the *X*–*Y* plane appeared at the breakdown sites.

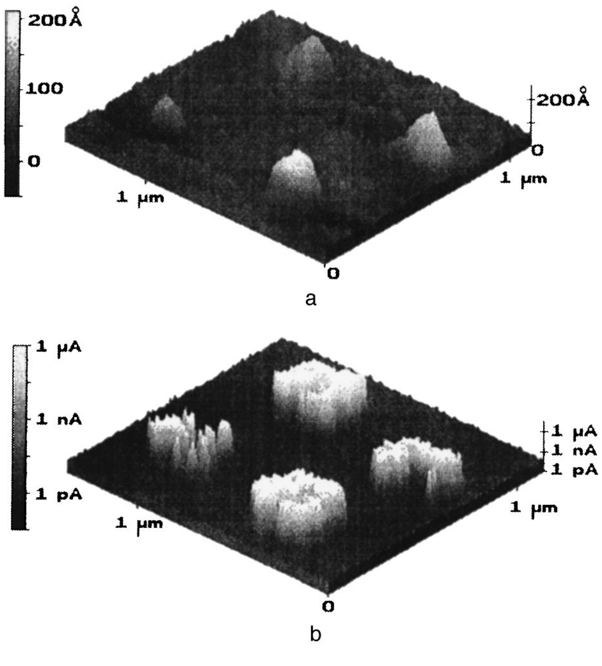

FIG. 3. Result of local dielectric breakdown of diamond film.

Figure 3b shows the distribution of the tunnel current measured at the same time as scanning the profile shown in Fig. 3a. It can be seen from Fig. 3b that an electrically conducting phase appeared at the breakdown sites, with the lighter parts of the image corresponding to higher conductivity. The size of the conducting sections is substantially larger than the size of the humps formed at the breakdown sites. This section of the sample was scanned repeatedly over 12 days. The images obtained showed good reproducibility, which suggests that these structures are stable and the scanning process does not destroy the surface of the sample.

The proposed design is considerably simpler than the conventional AFM design, since it obviates the need to use a microspring and devices for measuring its deflection. In addition, attaching the tip directly to the piezomanipulator eliminates any unstable behavior of the tip at the spring for certain distances between the tip and the sample[7] and can be used to set any required tip–sample gap, which means that the tunnel current can be recorded simultaneously.

This work was carried out under the Russian State Program ''Promising Technologies and Devices in Micro- and Nanoelectronics'' (Project No. 039.04.223/57/2-3/1-95) and the Federal Target Program ''State Support for the Integration of Higher Education and Fundamental Science'' (Project No. 32642).

[1] G. Binnig, H. Rohrer, Ch. Gerber, and E. Weibel, Phys. Rev. Lett. **49**, 57 (1982).
[2] G. Binnig, C. F. Quate, and Ch. Gerber, Phys. Rev. Lett. **56**, 930 (1986).
[3] G. Binnig, H. Rohrer, Ch. Gerber, and E. Weibel, Phys. Rev. Lett. **50**, 120 (1982).
[4] J. R. Hahn, H. Kang, S. Song, and I. C. Jean, Phys. Rev. B **53**, R1725 (1996).
[5] G. Binnig, Ch. Gerber, E. Stoll, T. R. Albrecht, and C. F. Quate, Europhys. Lett. **3**, 1281 (1987).
[6] O. Nickolayev and V. F. Petrenko, J. Vac. Sci. Technol. B **12**, 2443 (1994).
[7] D. Sarid and V. Elings, J. Vac. Sci. Technol. B **9**, 431 (1991).

Translated by R. M. Durham

Rotation of the wavefront of an optical vortex in free space

A. V. Volyar, V. G. Shvedov, and T. A. Fadeeva

Simferopol State University

(Submitted November 11, 1998)
Pis'ma Zh. Tekh. Fiz. **25**, 87–94 (March 12, 1999)

It is shown experimentally and theoretically that when an optical vortex propagates in free space, its wavefront rotates through an angle numerically equal to the Gouy phase. It is found that both the energy maximum of the optical vortex light flux and the amplitude zero of the perturbed optical vortex field propagate along the ray surface. It is shown that the ray surface, which is a consequence of the relativistic constraints on the beam group velocity, forms an unparted hyperboloid of revolution and has various properties: 1) the circulation of the Poynting vector on the surface does not depend on the longitudinal coordinate z; 2) the evolution of the light flux and a pure screw dislocation takes place along straight lines of this surface; 3) the Poynting vector on the ray surface is always perpendicular to the wavefront surface. [S1063-7850(99)01603-1]

As they propagate, the fields of Laguerre–Gauss and Hermite–Gauss beams may be rotated relative to the direction of propagation. This surprising property of laser beams does not alter their structural stability[1,2] and is caused by the presence of a nonzero azimuthal component of the Poynting vector. However, the physical and technical treatment of the rotational capacity of beams comes up against some major problems. For instance, Allen *et al.*[3] and Padgett and Allen[4] showed that the optical energy flux in Laguerre–Gauss beams and especially in optical vortices propagates along curvilinear trajectories in free space, which is generally inconsistent with the variational principle.[5] In addition, the trajectories of phase singularities (and pure screw dislocations in particular) in perturbed optical vortices have not been identified.

The aim of the present paper is to make a theoretical and experimental study of the rotation of the wavefront of optical vortices in free space and to study the local flow trajectories along which energy and pure screw dislocations of the wavefront propagate in perturbed beams.

1. We shall assume that a laser beam propagates in free space with electric and magnetic fields given by

$$\mathbf{E}=\mathbf{e}(x,y,z)\exp\{i[\omega t-k\mathcal{J}(x,y,z)]\},$$

$$\mathbf{H}=\mathbf{h}(x,y,z)\exp\{i[\omega t-k\mathcal{J}(x,y,z)]\}. \tag{1}$$

We define the Poynting vector[6] of this field as

$$\begin{aligned}\mathbf{P}&=1/2\mathrm{Re}\{\mathbf{e}\times\mathbf{h}^*\}\\&=1/2(\varepsilon_0/\mu_0)^{1/2}\mathrm{Re}\{|\mathbf{e}|^2\nabla\mathcal{J}-1(ik)(\mathbf{e}\times\boldsymbol{\nabla}\times\mathbf{e}^*)\}\\&=\mathbf{P}_0+\delta\mathbf{P}.\end{aligned} \tag{2}$$

Expression (2) was obtained using the steady-state Maxwell equations, from which the value of **h** was isolated. The first term in Eq. (2) characterizes the Poynting vector $\mathbf{P}_0$, perpendicular to the wavefront surface $\mathcal{J}=\mathrm{const}$. The second term $\delta\mathbf{P}$ in Eq. (2) is only nonzero for elliptically polarized fields, for which **e** changes abruptly in the beam cross section. This term characterizes the departure of the Poynting vector from the wave normal direction.

In the first approximation of perturbation theory[8] the optical vortex field[7] may be given as

$$e_r=\psi,\quad e_\psi=i\delta e_r,\quad e_z=i/k\nabla_t\mathbf{e}_t,$$

$$\mathbf{h}_t=(\varepsilon_0/\mu_0)^{1/2}\hat{\mathbf{z}}\times\mathbf{e}_t,$$

$$h_z=-(i/k)(\varepsilon_0/\mu_0)^{1/2}(\boldsymbol{\nabla}_t\times\mathbf{e}_t)\hat{\mathbf{z}}, \tag{3}$$

$\psi=(1/\Lambda)\exp\{-(r^2/\rho^2\Lambda)\}(x+i\kappa y/\rho\Lambda)^{|l|}$, $\Lambda=I+iz/z_R$, $z_R=k\rho^2/2$, $r^2=x^2+y^2$, ρ is the radius of the beam constriction in the cross section $z=0$, $|l|$ is the topological charge, $\kappa=\pm1$ is its sign, and $\sigma=\pm1$ is the helicity of the beam polarization ($\sigma=+1$ indicates right circular and $\sigma=-1$ left circular polarization).

Substituting expression (3) into expression (2) we find

$$P_r=K\frac{r}{R(z)}|\psi|^2,$$

$$P_\varphi=\frac{K}{k}\left\{\sigma\frac{d|\psi|^2}{dr}+\frac{\kappa|l|}{r}|\psi|^2\right\},\quad P_z\approx K|\psi|^2, \tag{4}$$

where $R(z)=(z_R^2/z)|\Lambda|^2$, $k=2\pi/\lambda_0$, $K=E_0^2(\varepsilon_0/\mu_0)^{1/2}$, and E_0 is the amplitude of the electric field.

The component P_φ in expression (4) indicates that energy circulates in the beam cross section. However, this by no means implies that the optical energy flux in free space propagates along a curvilinear trajectory.

In fact, the evolution of the Poynting vector **P** in free space is described by the equation of continuity $\nabla\mathbf{P}=0$, and thus the vector **P** is determined correct to within the vector $\nabla\times\mathbf{A}$. This indeterminacy can be eliminated by the Ehrenfest optical theorem,[9] which stipulates that only those vectors **P** corresponding to the maximum energy flux are physically meaningful. From expression (3) we find that the maximum energy flux occurs on the radius $r^2=x_m^2+y_m^2$:

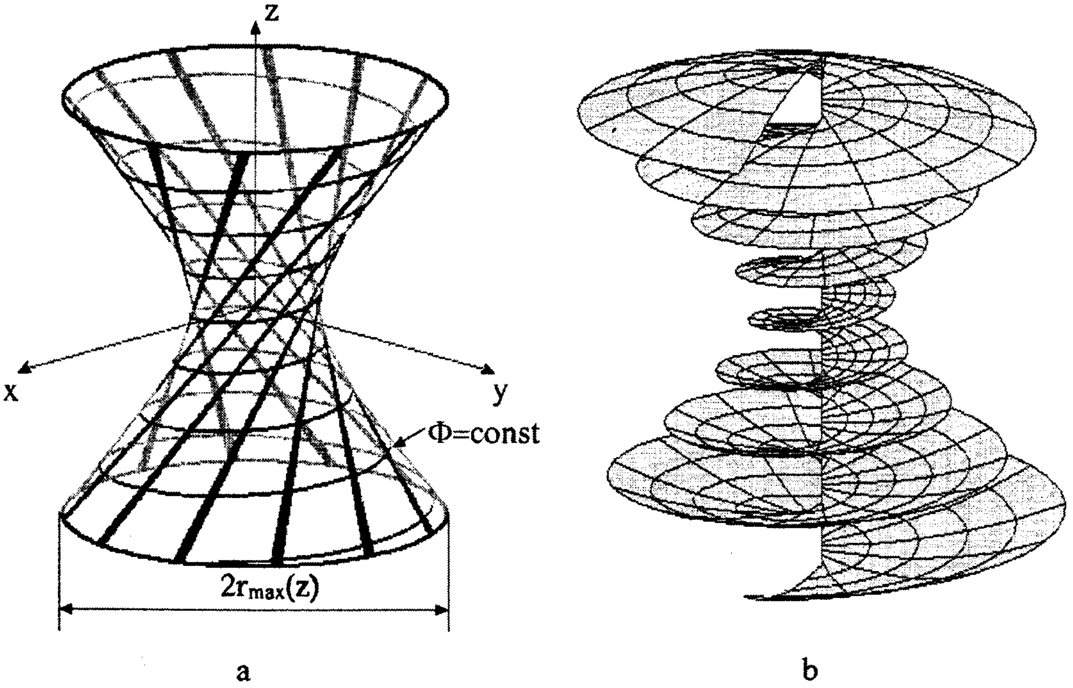

FIG. 1. Ray (a) and wave (b) surfaces of an optical vortex field with $|l|=1$ and $\kappa+1$. The spiral curve on the ray surface (a) is the line of constant phase $\Phi=\text{const}$. The local flow lines on the surface (a) are always perpendicular to the wave surface (b). (For clarity we have changed the scale of the wave surface).

$$x_m^2+y_m^2=(\rho^2/2)|\Lambda(z)|^{2|l|}. \qquad (5)$$

Expression (5) is the equation for a hyperboloid of one sheet.

We can show that the surface (5) has many remarkable features. First, on this surface the circulation of the linear energy flux density $\mathbf{P}_L=r\mathbf{P}$ does not depend on the longitudinal coordinate z:

$$\oint_L \mathbf{P}_L dL=\int\!\!\int_S \mathrm{curl}\,\mathbf{P}_L\cdot dS=f(\kappa|l|), \qquad (6)$$

where S is the area enclosed by the contour L (Fig. 1a). Using the equations $dr/(rP_r)=d\varphi/(P_\varphi)$ and (5), we find that the energy flux line $\mathbf{P}$ is given by

$$\varphi=(\kappa)\arctan(z/z_R). \qquad (7)$$

Expression (7) is the equation for the straight lines of local flow on the surface (5), and the energy flux in the optical vortex propagates along these straight trajectories [a second property of the surface (5)]. On the surface of the unparted hyperboloid there are two families of straight lines whose orientation relative to the z axis is defined[10] by the angle azimuthal φ and polar angle θ. One family of lines differs from the other by the sign of the angle φ. These two families of local flow lines are separated physically by a change in the sign of the topological charge κ in expression (7).

Figure 1a shows this ray surface for an optical vortex with $|l|=1$ and $\kappa=+1$ and Fig. 1b shows its wave surface. It is interesting to note that the angle φ in expression (7) does not depend on the helicity of the polarization σ, as may appear at first glance from Eq. (2), nor on the magnitude of the topological charge $|l|$. This follows from the third property of the ray surface: on the surface (5) we find $d\psi/dr=0$ and thus the first term in expression (4) for the P_φ component of the Poynting vector, which is responsible for the polarization properties of the laser beam, vanishes. Thus, on the ray surface (5) the Poynting vector is parallel to the wave normal vector. As a result, it is found that the observed angle of rotation φ of the local current line (7) is numerically equal to the Gouy phase.

If we visualize some point in the plane of the constriction $z=0$ at the wavefront, relate this point to the direction of the vector $\mathbf{P}_L$, and follow its evolution along the z axis, we observe that the wavefront is rotated through the angle φ determined by Eq. (7). Its instantaneous angular rotation velocity is given by

$$\Omega=z_R/(z^2+z_R^2)V_{\mathrm{ph}}, \qquad (8)$$

where V_{ph} is the phase velocity of the optical vortex. The angular velocity reaches a maximum near the beam waist $(z=0)$:

$$\Omega_{\max}=(\nu_0/\pi)(\lambda/\rho)^2, \qquad (9)$$

where ν_0 is the light frequency.

2. In order to observe this wavefront rotation experimentally, we need to have a physically discernible marker on the wave surface. This marker can be a pure screw dislocation of the wavefront displaced along the radius by the distance d. In order to achieve such a displacement, a smooth Gaussian beam of amplitude e_0 must be superposed on an optical vortex having a field amplitude e_V such that the constriction radii of the optical vortex and the Gaussian beam are the same $(\rho_V=\rho_0)$. The wavefront dislocation then has the radial coordinate[7]

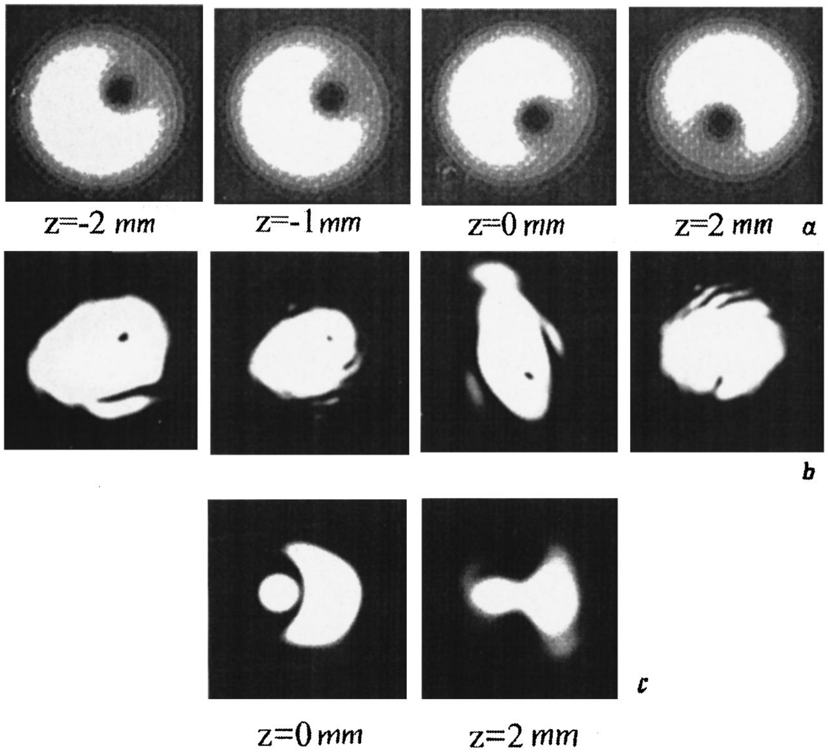

FIG. 2. Results of computer calculations (line a) and photographs of the intensity distribution in the cross section of an optical vortex with $|l|=1$ and $\kappa=+1$ near the waist of the beam after an $f=50$ mm lens at a suitable length z from the plane of the constriction (line b). Photographs showing the transformation of a topological dipole into an annular edge dislocation near the focus of a 20× microscope objective (line c).

$$r_d^2=x_d^2+y_d^2=\rho^2\left(\frac{e_v}{e_0}\right)^2\frac{z^2+z_R^2}{z_R^2}, \tag{10}$$

while the azimuthal coordinate φ is given by Eq. (7). However, this implies that the zero intensity of the optical vortex field (pure screw dislocation) propagates along a straight line lying on the surface of the hyperboloid (10). The intensity maximum will clearly have the same radial coordinate (10), but the azimuthal coordinate is given by $\varphi_{\max}=\pi+\varphi_{\min}$. From this it follows that the maximum and minimum of the vortex intensity propagate along straight lines on the ray surface and form a coupled system with its center of gravity lying on the beam axis.

Basistiy *et al.*[7] made an experimental investigation of the rotation of two coupled dislocations with topological charge of the same sign. Since it is extremely difficult to obtain an analytic expression for this dislocation dumbbell, we focused our attention on the evolution of an isolated perturbed dislocation. In order to determine experimentally the motion of a perturbed pure screw dislocation, we directed circularly polarized laser radiation onto the hologram of an optical vortex[7] with $|l|=1$, shifted relative to the center of the beam, and focused this using an $f=50$ mm spherical lens. We examined an image of the field of the optical vortex near the focal plane under a horizontal microscope. The position of the screw dislocation was recorded in various cross sections of the beam. Figure 2 shows photographs of the beam in various cross sections z and the results of computer calculations. We found that a change in the direction of circulation of the circular polarization from right $(\sigma=+1)$ to left $(\sigma=-1)$ does not change the propagation of the pure screw dislocation. However, reversal of the sign of the topological charge κ changed the direction of rotation of the field intensity zero.

The rotation of the wavefront shows up most clearly for a beam with a double pure screw dislocation (topological dipole)[11] propagating through the plane of the constriction. In this case, the dislocation with positive topological charge $l>0$ tends to rotate clockwise about the z axis, while the dislocation with negative $l<0$ tends to rotate counterclockwise. Thus, the topological dipole as a whole does not rotate in the regions $z>0$ and $z<0$. However, the topological charges undergo polarity reversal near the plane of the constriction $(z=0)$. Thus, the dipole state is indeterminate and this results in the formation of an annular edge dislocation. This process is illustrated by a photograph of the field after passing through a $20^{\times}$ microscope objective (Fig. 2c).

To conclude, we note that the Poynting vector characterizes the group velocity of the beam, which cannot exceed the velocity of light in vacuum. In our case, the group velocity describes the propagation of the intensity maximum of the optical vortex. This means that concepts of a ray surface follow directly from relativistic constraints.

[1] E. Abramochkin and V. Volostnikov, Opt. Commun. **102**, 336 (1993).

[2] E. Abramochkin and V. Volostnikov, Opt. Commun. **125**, 302 (1996).

[3] L. Allen, M. W. Beijersbergen, R. J. C. Spreeuw, and J. P. Woerdman, Phys. Rev. A **45**, 8185 (1992).

[4] M. J. Padgett and L. Allen, Opt. Commun. **121**, 36 (1995).

[5] L. D. Landau and E. M. Lifshits, *The Classical Theory of Fields*, 4th English ed. (Pergamon Press, Oxford, 1975) [Russ. original, later ed., Nauka, Moscow, 1988, 512 pp.]

[6] M. Born and E. Wolf, *Principles of Optics*, 4th ed. (Pergamon Press, Oxford, 1969; Nauka, Moscow, 1973, 720 pp.)

[7] I. V. Basistiy, V. Yu. Bazhenov, M. S. Soskin, and M. V. Vasnetsov, Opt. Commun. **103**, 422 (1993).

[8] M. Lax, W. H. Louisell, and W. B. McKnight, Phys. Rev. A **11**, 1365 (1975).

[9] D. Marcuse, *Integrated Optics* (IEEE Press, New York, 1973; Mir, Moscow, 1974, 576 pp.)

[10] V. F. Kagan, *Principles of Surface Theory* Vol. 1 [in Russian], OGIZ, Moscow (1947), 512 pp.

[11] I. V. Basisty, I. G. Marienko, M. S. Soskin, and M. V. Vasnetsov, Proc. SPIE **2792**, 172 (1996).

Translated by R. M. Durham

TECHNICAL PHYSICS LETTERS VOLUME 25, NUMBER 3 MARCH 1999

Chaotic oscillations in a system of coupled triggers

É. V. Kal'yanov

Institute of Radio Engineering and Electronics, Fryazin' Branch of the Russian Academy of Sciences

(Submitted August 3, 1998)
Pis'ma Zh. Tekh. Fiz. **25**, 1–6 (March 26, 1999)

A circuit consisting of two triggers coupled by a capacitance is studied. The equations of motion are presented with a cubic approximation for the nonlinear terms. It is shown by numerical analysis that chaotic oscillations can be excited. A mechanism for the transition of the oscillations to chaos is described. © *1999 American Institute of Physics.* [S1063-7850(99)01703-6]

Triggers and their ensembles are widely used in various radio-engineering systems, including computers. As the speed of operation increases, the working frequencies (in computers, the clock speed) must be increased, which produces complicated effects due to the influence of, for example, parasitic capacitances. The latter inevitably appear as ultrahigh frequencies are approached. For this reason, it is of interest to study the operation of a circuit consisting of coupled triggers, specifically when they are coupled capacitively.

In the present letter the interaction of two classical triggers coupled by capacitances is studied. It is shown that chaotic oscillations are possible in such a circuit. This is of interest in its own right, since the investigation of the chaotic behavior of various systems is now a pressing problem.[1–3]

The circuit consisting of coupled triggers is shown in Fig. 1. The first trigger T_1 contains a capacitor C_1, a resistor R_1, an inductor L_1, and a nonlinear active element g_1 arranged in the classical way.[4] The components C_2, R_2, L_2, and g_2 determine the completely analogous arrangment of the second trigger T_2. The triggers are coupled by the capacitors C_{01}, C_0, and C_{02}.

The equations describing the operation of the circuit in Fig. 1 can be represented in terms of dimensionless quantities in the form

$$\begin{aligned}
&\dot{x}=y+y_1-x_1-g_1(x_1),\\
&\dot{x}_2=\delta[y+y_2-x_2-g_2(x_2)],\\
&\dot{y}=\alpha\{x_1-(y+y_1)+z_1+\varkappa[x_2-(y+y_2)+z_2]\},\\
&\dot{y}_1=[x_1-(y+y_i)+z_i]\gamma_i^{-1},\\
&\dot{z}_i=-\beta_i(y+y_i),
\end{aligned}\tag{1}$$

where $i=1,2$. The variables x_1, x_2, y, y_1, and y_2 determine, respectively, the oscillatory processes on the capacitors C_1, C_2, C_0, C_{01}, and C_{02}, and the variables z_1 and z_2 characterize the variation of the current flowing through the inductances L_1 and L_2. An overdot denotes differentiation with respect to the dimensionless time t, which is related to the real time t^* by $t=t^*(R_1C_1)^{-1}$. The constant coefficients in Eqs. (1) are $\alpha=C_1/C_0$, $\beta_1=C_1R_1^2/L_1$, $\beta_2=C_1R_1^2/L_2$, $\varkappa=R_1/R_2$, $\delta=\varkappa C_1/C_2$, $\gamma_1=C_{01}/C_1$, and $\gamma_2=C_{02}/C_1$. The functions $g_1(x_i)$ describe the nonlinear characteristics of the active components. Using a cubic approximation, they can be represented by the relation

$$g_i(x_i)=-\nu_i x_i+\mu_i x_i^3,\tag{2}$$

where ν_i and μ_i are constants.

From the system (2) it is easy to obtain equations describing the processes in an individual trigger. Setting $\gamma_1=0$ we obtain for the trigger T_1

$$\begin{aligned}
&\dot{x}_1=z_1-g_1(x_1),\\
&\dot{z}_1=-\beta(x_1+z_1),
\end{aligned}\tag{3}$$

The equations (1)–(3) were solved by the fourth-order Runge–Kutta method with a time step of 0.1.

Numerical analysis of Eqs. (1) and (2) showed that the system of coupled triggers is auto-oscillatory and exhibits chaotic dynamics. The computational results illustrating this are presented in Fig. 2. They were obtained for the case of identical triggers ($\beta_1=\beta_2=1.8$, $\delta=\varkappa=1$, $\nu_1=\nu_2=0.25$, and $\mu_1=\mu_2=0.1$) with $\alpha=10$, $\gamma_1=100$, and $\gamma_2=40$. The initial conditions were assumed to be $x_i(0)=y(0)=y_i(0)=z_i(0)=0.1$. Figure 2a shows an image of the attractor of the oscillatory process $x_1(t)$ (in the coordinates (x_1, y)), and Fig. 2b shows the motion of an image point in the phase space x_1, x_2.

The attractor of the autostochastic process $x_1(t)$ attests to the existence of two basins (regions)ll * of attraction (which we term P_1 and P_2), where the system undergoes chaotic oscillations and randomly switches from one basin of attraction to another (Fig. 2a). The existence of two basins of attraction is consistent with the existence of two stable states in a trigger. In accordance with Eqs. (2) and (3) with the initial conditions $x_1(0)=0.1$ and $z_1(0)=0$ (once again, $\nu_1=0.25$, $\mu_1=0.1$, and $\beta_1=1.8$), the stationary value of $x_1(t)$ is 1.58, and for the initial conditions $x(0)=-0.1$ and $z(0)=0$ it becomes negative for the same absolute quantity $x_1(t)=-1.58$). The basins P_1 and P_2, where chaotic auto-oscillations of the coupled system of triggers occur, are located precisely in the neighborhoods of these stable states.

The oscillatory process $x_2(t)$ is also chaotic with oscillations switching between the two basins of attraction, but the structure of the attractor of this process is different from that presented in Fig. 2a. The presence of four ''clumps'' of

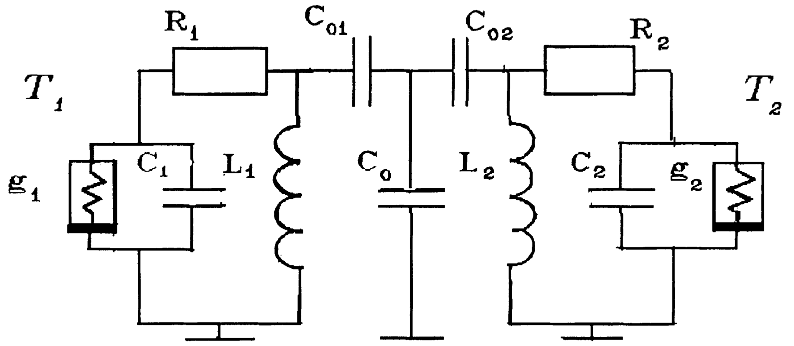

FIG. 1. Circuit consisting of two triggers coupled by capacitors.

chaotic motion of the image point in the phase space x_1, x_2 attests to this (Fig. 2b). The clumps near the limit set $x_1 = x_2$ correspond to time intervals when the chaotic oscillations $x_1(t)$ and $x_2(t)$ occur simultaneously in one basin of attraction (first or second), while the two other regions where trajectories clump (near the limit set $x_1 = -x_2$) correspond to time intervals where the oscillatory processes occur in different basins of attraction.

It should be noted that for $\varkappa = 0$ Eqs. (1) and (2) describe a generator, similar to the well-known Chua circuit[5] but with a more complicated oscillatory loop. The system of equations obtained in this case with the parameter values for which Fig. 2a was calculated (with the exception of the fact that $\varkappa = 0$) also possesses chaotic dynamics and permits switching to Eqs. (3). In the well-known dimensionless Chua equations[1,2,5–9] such a switch is impossible, since in the latter equations the dimensionless time is introduced by a relation that does not contain the capacitance appearing in the trigger circuit.

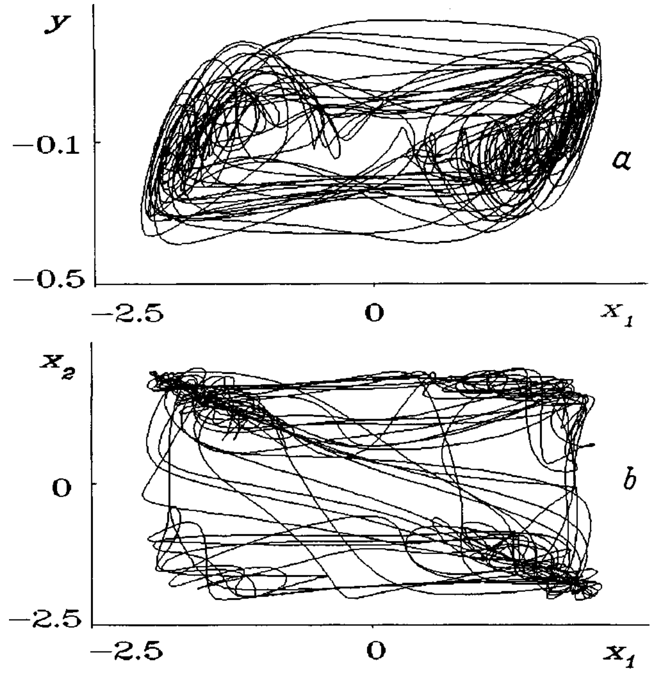

FIG. 2. Attractor of an oscillatory process in the first trigger (a) and motion of an image point in the (x_1, x_2) plane (b) with capacitive coupling of the two coupled triggers.

The foregoing analysis shows that the mechanism by which the oscillations in the circuit of Fig. 1 become chaotic involves impulsive excitation of an oscillatory process in the loop formed by the inductors of the triggers and the capacitive coupling components. The presence of these components gives rise to two autostochastic systems with a common oscillatory loop. Each partial system is similar to a Chua circuit, if in the latter the resonant system is made more complicated in a corresponding manner. The shock waves in the loop, which are maintained by the presence of the nonlinear components, grow in one of the basins of attraction (near one stable state of the triggers) until the other stable state of the triggers (the other basin of attraction) is reached. The waves ''break'' randomly in agreement with the chaotic change in the initial conditions of the impulsively excited oscillations in the loop. The differences in the coupling parameters and, in consequence, in the conditions for switching of the triggers make the interacting oscillations more complicated.

The circuit studied above can be used as a simple source of chaotic oscillations with more highly entangled motions than those observed in an ordinary Chua circuit, whose study and practical applications are still the sibject of many investigations.[1,2,6–9]

This work was supported by the Russian Fund for Fundamental Research (Grant 98-02-16722).

[1] A. S. Dmitriev, A. I. Panas, and S. O. Starkov, Zarubezhnaya Radioélektronika, Uspekhi sovremennoĭ radioélektroniki, No. 10, 4 (1997).

[2] V. D. Shalfeev *et al.*, Ibid., pp. 27–49.

[3] A. S. Khramov, Pis'ma Zh. Tekh. Fiz. **24**(5), 51 (1998) [Tech. Phys. Lett. **24**, 189 (1998)].

[4] W. Cunningham, *Introduction to the Theory of Nonlinear Systems* (Russian translation, Gosénergoizdat, 1962).

[5] L. O. Chua, M. Komuro, and T. Matsumoto, IEEE Control Syst. Mag. **CAS-33**, 1073 (1986).

[6] C. W. Wu, T. Yang, and L. O. Chua, Int. J. Bifurcation and Chaos **6**, 455 (1996).

[7] M. Biey *et al.*, in *Proceedings of the 5-th International Specialist Workshop, Nonlinear Dynamics of Electron Systems (NDES'97),* June 26–27, 1997, pp. 358–363.

[8] V. V. Astakhov *et al.*, Radiotekh. i élektron., No. 3, 320 (1997).

[9] I. A. Khovanov and V. S. Anishchenko, Radiotekh. i élektron. **42**(7), 823 (1997).

Translated by M. E. Alferieff

The possibility of forming soliton-like pulses during ion implantation

S. G. Psakh'e, K. P. Zol'nikov, R. I. Kadyrov, G. E. Rudenskiĭ, Yu. P. Sharkeev,
and V. M. Kuznetsov

Institute of the Physics of the Strength of Materials and Materials Science, Siberian Branch of the Russian Academy of Sciences, Tomsk

(Submitted October 14, 1998)
Pis'ma Zh. Tekh. Fiz. **25**, 7–12 (March 26, 1999)

The nonlinear response of a material under a high-energy process acting on groups of atoms or individual atoms of a free surface is studied. The dissipation of the energy transferred by soliton-like pulses at structural defects, such as regions with high vacancy density, grain boundaries, and the free surface, is investigated. A method of describing the ''long-range action'' during ion implantation in metallic materials is proposed. © *1999 American Institute of Physics.* [S1063-7850(99)01803-0]

To understand the physical nature of the processes in materials subjected to high-energy processes it is necessary to study in detail the nonlinear response of a material. The development of new materials that work successfully under extreme conditions (high pressures and temperatures, impact loads, irradiation, and so on) makes this problem of great interest from both the scientific and applied standpoints.

A method that has been used successfully for a long time to study the nonlinear response of materials at the microscopic level is molecular dynamics. Early treatments based on this approach showed that an external high-energy perturbation acting on a material can produce soliton-like pulses in it.[1–4] In a defect-free material these excitations can propagate over large distances with virtually no change in shape and amplitude.[5–8]

The present letter is devoted to a molecular-dynamics investigation of the characteristic features of the dissipation of the energy transferred by solitary pulses on structural defects, such as a free surface, grain boundaries, and regions with high vacancy density. The possibility of generating solitary pulses when a free surface is irradiated by high-energy particles or beams is also studied.

Three-dimensional Ni and Al crystallites, containing about 10000 atoms, were the objects of investigation. In the present work we studied solitary pulses passing through a region with low atomic density and grain boundaries were investigated on the basis of a pair interaction potential. The interaction of a soliton-like pulse with a free surface was studied using a multiparticle potential based on a model electron density functional.[9,10]

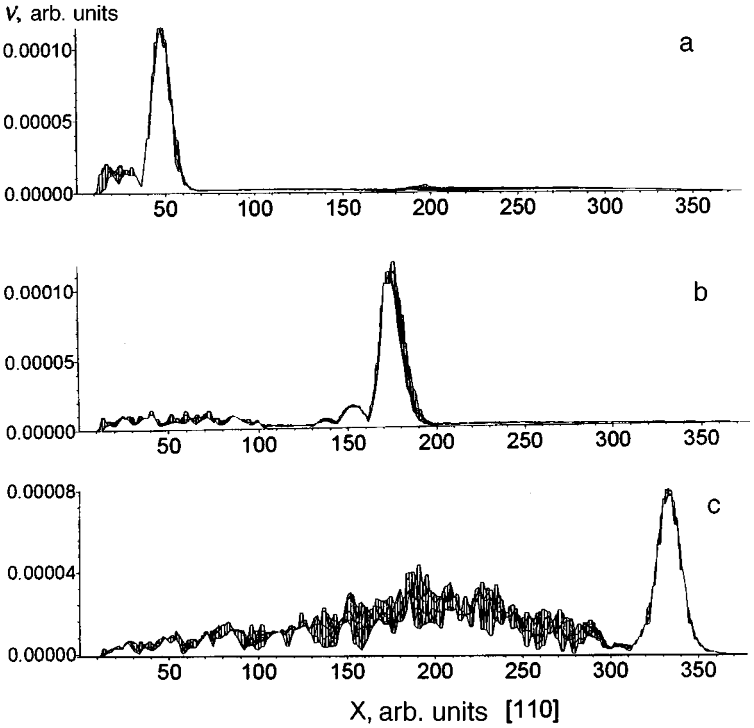

FIG. 1. Position of a soliton-like pulse: a — at the start of the sample, b — near a grain boundary, c — after passage through a grain boundary.

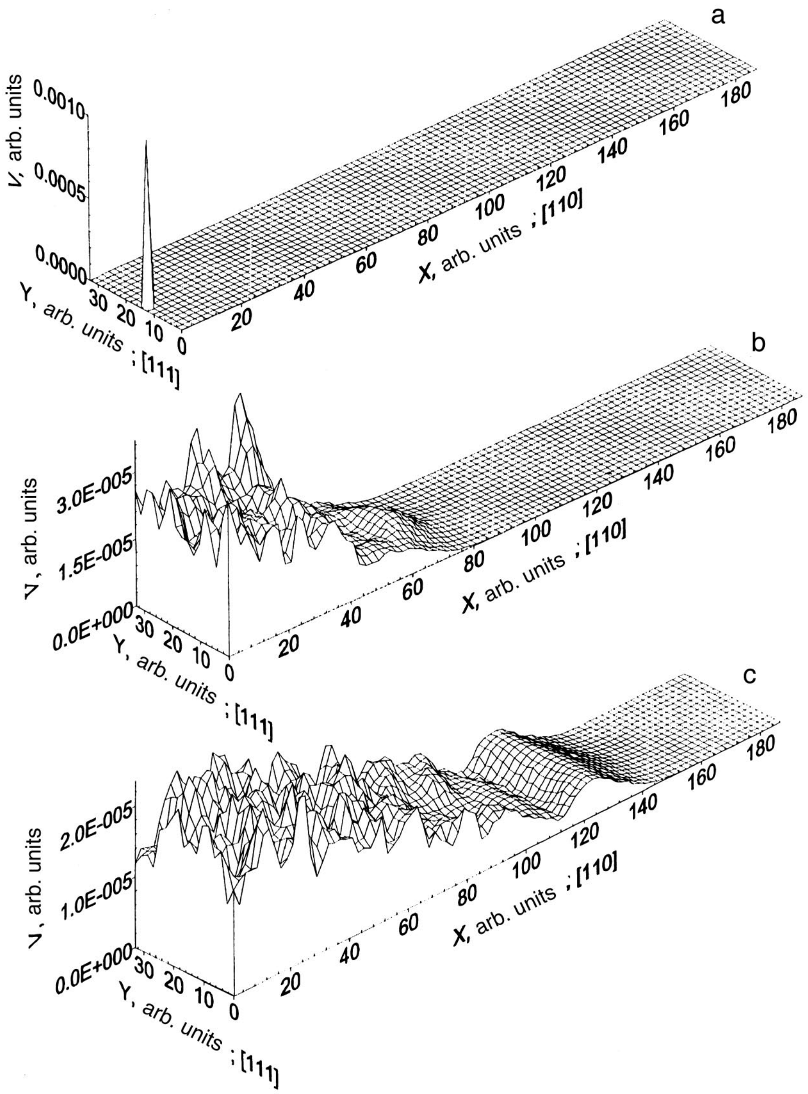

FIG. 2. Stages of formation of a soliton-like pulse.

The analysis of the passage of solitary waves through a region with low atomic density in Al showed that the larger the deviation of the atomic density in the defect region from the equilibrium value, the higher the fraction of the pulse energy dissipated in this region is. Thus, for a soliton-like pulse passing through local regions of a material that contain 25 and 50 vacancies the amplitude of the pulse decreased by 10 and 20%, respectively. A similar picture was also observed for a pulse passing through grain boundaries of a special type (for example, $\Sigma 7$-type boundaries). Figure 1 shows a compression-initiated soliton-like pulse in an Al sample at various times. The grain boundary was located at the center of the experimental sample perpendicular to the propagation direction of the pulse. It is evident from Fig. 1 that a large fraction of the pulse energy (approximately 20%) is dissipated in the grain-boundary region.

Investigations of the interaction of a solitary pulse with a free surface showed that in this case energy is pumped into layers near the surface of the material. According to the computational results, when a pulse interacts with a free Ni surface the pulse amplitude can increase by a factor of 1.5–2, depending on the orientation of the free surface. This effect is accompanied by a small compression of the atomic layers. After the pulse is reflected from the free surface, the pulse amplitude decreases and energy is pumped into the region of the material near the surface.

The simulation results showed that a high-energy process acting on a group of atoms or on individual atoms of a free surface can generate soliton-like pulses. Effects of this kind can occur when a material is irradiated by powerful electron beams and radiation or by ion bombardment. Figure 2 shows the characteristic stages of the formation of a soliton-like pulse as a result of energy transfer to an atom of the free surface. Specifically, each atom was assigned a velocity of about 2000 m/s directed into the material. We note that for ion implantation much higher (by one or two orders of magnitude) velocities can be imparted to the atoms in the irradiated surface. The instant at which momentum is tranferred to a surface atom is illustrated in the first stage (Fig. 2a). In the second stage energy is transferred to the nearest neighbors and a pulse with a hemispherical front is formed (Fig. 2b). The atoms at the center of the front have high velocities, i.e., an initial hump is formed. As the pulse propagates into the material, the pulse front transforms from hemispherical to planar and the crest of the front is leveled off (Fig. 2c). A similar picture is also observed when a pertubation acts on a group of several neighboring atoms in the free surface.

These results are of particular interest for understanding the processes occurring during ion implantation in metallic materials. The structural rearrangements in the near-surface layers of ion-implanted metals agree quite well with existing theoretical calculations of the interaction of ions with a material. At the same time the important ''long-range action'' phenomenon (the formation of a defect structure in the material at distances much greater than the thickness of the surface layer doped during ion implantation[11–13]) has still not been adequately studied on a theoretical level. The difficulties of the experimental study of this problem are due to the short time scales of the processes being studied and the high energies of the ion fluxes as well as to the strongly nonlinear processes occurring when ion beams strike the surface layers of a material.[14]

Note that up to now we have considered the interaction of one pulse with structural defects, while in the case of ion implantation with metallurgical doses ($10^{15}-10^{17}$ ions/cm^2) an enormous number of pulses are generated. This should result in pumping of energy into both the ion-doped surface region and the defect regions (grain boundaries, regions with high vacancy density, and so on) which are located in the interior of the material. We note that even in a well-annealed metallic crystal the dislocation density can reach 10^7 cm^{-2} and higher. Since the propagation velocity of the pulses in the material is very high (close to the speed of sound), energy transfer and redistribution in the interior of the material can occur quite rapidly. Aside from this, they can also cause existing dislocations to be displaced from the surface into the interior of the material. The energy pumped during ion implantation by soliton-like pulses into the near-surface layers of a material will transform into the energy of the defect system of the crystal, including dislocation structure. In the process the dislocation density in the near-surface layers of the irradiated material will also increase.

This mechanism of the change in the defect subsystem of a crystal is probably best observed in single-crystal and large-grain materials, since in these cases pulses propagate over large distances with much smaller energy losses. Therefore the long-range action effects will be manifested in the near-surface layers, which are at least an order of magnitude thickner than the doped surface layer.[11,12,15]

[1] M. Toda, *Springer series in Solid State Sciences*, Vol. 20, *Theory of Nonlinear Lattices*, (Springer-Verlag, New York, 1981; Russian translation, Mir, Moscow, 1984).

[2] R. K. Bullough and P. K. Caudrey [Eds.], *Solitons* (Springer-Verlag, New York, 1980; Russian translation, Mir, Moscow, 1983).

[3] M. Wadati, J. Phys. Soc. Jpn. **38**, 673–680 (1975).

[4] R. Kh. Sabirov, Fiz. Tverd. Tela (Leningrad) **32**(7), 1992 (1990) [Sov. Phys. Solid State **32**, 1161 (1990)].

[5] S. G. Psakh'e, K. P. Zol'nikov, and S. Yu. Korostelev, Pis'ma Zh. Tekh. Fiz. **21**(13), 1 (1995) [Tech. Phys. Lett. **21**, 489 (1995)].

[6] S. G. Psakh'e, K. P. Zol'nikov, and D. Yu. Saraev, Fiz. Goreniya Vzryva **33**(2), 43 (1997).

[7] S. G. Psakh'e, K. P. Zol'nikov, and D. Yu. Saraev, Pis'ma Zh. Tekh. Fiz. **24**(3), 42 (1998) [Tech. Phys. Lett. **24**, 99 (1998)].

[8] S. G. Psakh'e, K. P. Zol'nikov, and D. Ju. Saraev, J. Mater. Sci. Technol. **14**, 1 (1998).

[9] V. M. Kuznetsov, P. P. Kaminskiĭ, and V. F. Perevalova, Fiz. Met. Metalloved. **63**, 213 (1987).

[10] V. M. Kuznetsov, G. E. Rudenskii, R. I. Kadyrov, and P. P. Kakinskiĭ, in *Shock Induced Chemical Processing: Proceeding of the USA–Russian Workshop*, St. Petersburg, 1996, pp. 97–106.

[11] D. K. Sood and G. Dearnaley, J. Vac. Sci. Technol. **12**, 463 (1975).

[12] Yu. P. Sharkeev, A. N. Didenko, and E. V. Kozlov, Surf. Coat. Technol. **65**, 112 (1994).

[13] Yu. P. Sharkeev, E. V. Kozlov, and A. N. Didenko, Surf. Coat. Technol. **96**, 103 (1997).

[14] F. F. Komarov, *Ion Implantation in Metals* (Metallurgiya, Moscow, 1990).

[15] V. P. Zhukov and A. A. Boldin, Phys. Status Solidi B **166**, 339 (1991).

Translated by M. E. Alferieff

Anomalous character of the decay kinetics of the photoluminescence of carbonized porous silicon

B. M. Kostishko, Sh. R. Atazhanov, S. N. Mikov, I. P. Puzov, and K. A. Kordetskiĭ

Ul'yanov State University

(Submitted 10 September 1998)
Pis'ma Zh. Tekh. Fiz. **25**, 13–20 (26 March 1999)

The time dependence of the decay of the photoluminescence of porous silicon subjected to high-temperature carbonization (1000–1200 °C) and simultaneously doped with B, P, Ga, or Al atoms is investigated. The boron-doped samples show an anomalously long decay time for the blue-green (2.4 eV) photoluminescence band. In addition, in this case oscillations with a period of 50 ms are observed in the photoluminescence decay curve. © *1999 American Institute of Physics.* [S1063-7850(99)01903-5]

Since 1990 a large number of research groups throughout the world have been actively studying mechanisms for the efficient photoluminescence (PL) of porous silicon (PS). However, even though PS-based light-emitting diodes,[1] photocells,[2] gas sensors,[3] and other devices already exist, it is still not possible to talk realistically about applying PS in microelectronics. The high instability of the optical properties of porous silicon obtained by chemical and electrochemical etching is the main reason why the devices listed above remain in the laboratory. In recent years increasing attention has been devoted to the investigation of methods for modifying PS and subsequently altering its degradation properties, photoluminescence spectra, and relaxation spectra. Of the most important results in this direction we call attention to the work concerning the rapid thermal oxidation,[4] prolonged low-temperature vacuum annealing,[5] and laser modification of the initial single-crystal silicon wafer.[6]

We report in the present letter the results from studying the kinetics of the decay of PL from porous silicon subjected to rapid high-temperature carbonization to stabilize the light-emission properties.[7] The PS samples were produced using phosphorus-doped silicon wafers with (100) orientation and resistivity $\rho=2.4\ \Omega\cdot\mathrm{cm}$. The porous silicon was produced by the standard technology in a process of electrochemical etching in the electrolyte $HF:C_2H_5OH=1:1$. The electrochemical etch time was 40 min for a current density 20 mA/cm^2.

Freshly prepared samples of PS were placed in a reactor, where carbonization was performed at temperatures 1000–1200 °C for 2–4 min in carbon tetrachloride gas (CCl_4) with hydrogen as the carrier gas.[7] During the carbonization process a near-surface region of various samples was doped from solid-phase sources with B, Al, or Ga atoms to density $5\times10^{17}\ \mathrm{cm}^{-3}$ or from the gaseous compound P_2Cl_5 with P atoms to density $3\times10^{18}\ \mathrm{cm}^{-3}$. The procedure described is used to produce 10–15 nm buffer layers in 3C–SiC/Si heteroepitaxial structures. Such buffer layers formed on a single-crystal substrate do not contain a silicon-carbide phase, but Auger spectroscopy shows that they are supersaturated with carbon (15%, near the surface) and contain no oxygen. The PL of modified PS samples was blue-green with two sharp spectral maxima near 1.9 and 2.5 eV.[7]

The excitation of photoluminescence in the process of recording the decay kinetics of the luminescence was accomplished using ultraviolet radiation from an ILA-800 nitrogen vapor laser ($\lambda=337$ nm) with pulse repetition frequency 10 Hz, pulse duration 7.5 ns, and pulse power 500 kW. The PL was measured ''in reflection.'' The radiation was collected by a system of quartz lenses onto the input slit of an MDR-23 monochromator and then recorded in the photon-counting regime. The resolution of the apparatus according to the PL relaxation times was 1.0 μs.

Analysis of the decay kinetics of the PL of carbonized PS showed that the temporal decay of the photoluminescence for Al-, Ga-, or P-doped samples is similar to that observed in the cases where PS was modified by oxidation[4] or laser annealing.[6] However, the samples carbonized with simultaneous doping with boron atoms possessed an anomalously long PL decay time in the blue-green region ($\lambda=500$ nm). The decay of the red line in the PL spectrum (the characteristic times are hundreds of nanoseconds for freshly prepared PS[8] and hundreds of microseconds for modified PS[4,6]), which in all previously known cases was slower, is now faster than in the short-wavelength part of the spectrum.

Figures 1a and 1b show the time dependence of the PL intensity at a wavelength of 500 nm for boron-doped porous silicon SEC. carbonized for 2 min at 1200 °C. It is obvious that the decay of the PL is not exponential and is very slow, seconds. This anomalously high value is 7 orders of magnitude longer than the decay time of the photoluminescence of the initial PS and 4 to 5 orders of magnitude longer than the PL decay time of oxidized PS. The prolonged afterglow of the sections exposed to UV radiation is even noticeable visually. Another substantial feature observed in the boron-doped samples is the nonmonotonic character of the decay: oscillations with a period of 50 ms are present in the spectrum (Fig. 1b). In addition, these oscillations are observed in different sections of the sample, and their period does not change with time when the samples are stored in air.

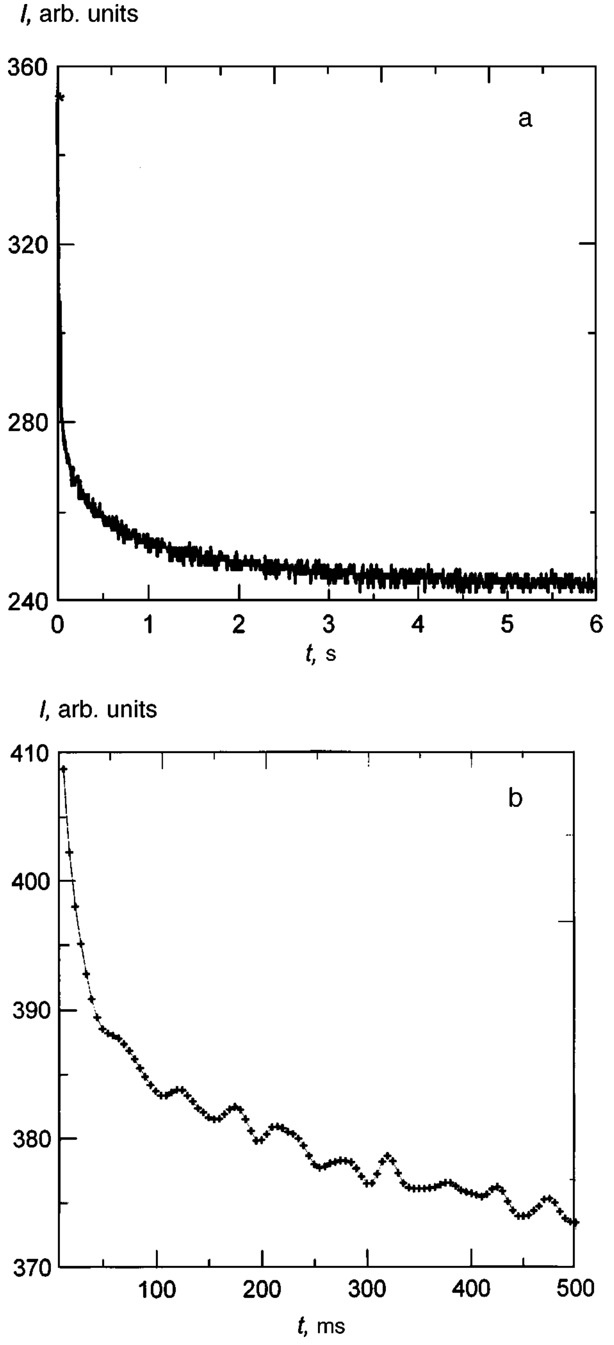

FIG. 1. Time-dependence of the blue-green (520 nm) photoluminescence line of porous silicon carbonized for 4 min at 1200 °C and simultaneously doped with boron atoms: a — averaging over 50 laser pulses and b — averaging over 100 laser pulses.

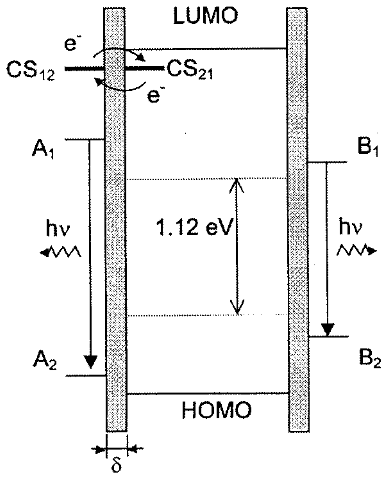

FIG. 2. Diagram illustrating resonant charge transfer in a system of isolated attachment centers.

A plot constructed using a logarithmic scale made it possible to describe the experimentally observed time dependence of the PL by a sum of two exponentials with characteristic times τ_1 and τ_2:

$$I = A_0 + A_1 \exp(-t/\tau_1) + A_2 \exp(-t/\tau_2). \tag{1}$$

The decay time τ_1 for the fast exponential changes negligibly with increasing number of laser pulses irradiating the sample (13.4 ms for 50 repetitions and 15.7 ms for 100 repetitions). The decay time τ_2 for the slow component decreases by almost a factor of 3 (857 ms for 50 repetitions and 333 ms for 100 repetitions). The increase in the decay rate of the blue-green PL line with increasing number of repetitions of the laser pulses attests to the existence of the photostimulated fatigue of carbonized PS.[9]

The slow decay of the photoluminescence could be due to several factors. First, it could be due to the formation of a large number of attachment centers during the carbonization process. In this case the fact that the effect is observed only in boron-doped samples signifies that the attachment centers are associated with a state of the impurity atoms in quantum wires. Another possible mechanism is due to the appearance, during doping, of a *p–n* junction whose electric field separates the mobile carriers generated in the process of laser irradiation. Then the lifetime of the charge carriers which have accumulated in quantum-size regions will increase substantially, since carrier transport through nanometer sections of the quantum wires in ''lightning'' or ''coral-like'' structures[10] is impeded, and relaxation is now determined mainly by tunneling processes.

The existence of oscillations (Fig. 1b) can be explained, in our opinion, by resonant charge transfer between localized attachment centers (CS) separated by tunneling-transparent potential barriers. This situation is illustrated in Fig. 2. The band gap of the initial single-crystal silicon ($E_g = 1.12$ eV) is shown between the highest occupied orbital state (HOMO) and the lowest unoccupied orbital state (LUMO) in PS. Judging from the presence of two peaks in the PL spectrum two types of luminescence centers are present in the system, one associated with radiative transitions in porous silicon (1.9 eV) and the other with radiative transitions in 3C–SiC nanocrystallites (2.4 eV).[7] The upper and lower levels of these transitions are shown in Fig. 2 by the symbols B_1, B_2 and A_1, A_2, respectively. The attachment centers separated by a potential barrier of width δ are designated as CS_{12} and CS_{21}. Then the interaction in a system consisting of two localized levels can be written in the Anderson–Newns model[11]

$$\begin{cases} i\dfrac{d}{dt}a_{12}(t)=E_1a_{12}(t)+V_0a_{21}(t), \\ \\ i\dfrac{d}{dt}a_{21}(t)=V_0a_{12}(t)+E_2a_{21}(t), \end{cases} \tag{2}$$

where E_1 and E_2 are, respectively, the energy levels of CS_{12} and CS_{21}, V_0 is the interaction potential of these states, a_{12} and a_{21} are the coefficients of the wave functions

$$\psi=a_{12}(t)\psi_{12}+a_{21}(t)\psi_{21}, \tag{3}$$

and ψ_{12} and ψ_{21} are the wave functions of the discrete attachment levels. The electron tunneling probability in this system and hence the probability of finding an electron in the level CS_{12}, from which thermalization to the radiative centers A occurs, can be described by the equation

$$P(t)=1-|a_{21}(t)|^2=\frac{4V_0^2}{(W_2-W_1)^2}\sin^2\left(\frac{W_2-W_1}{2}t\right), \tag{4}$$

where $W_{1,2}=(\Delta E\pm\sqrt{\Delta E^2+4V_0^2}/2$ and $\Delta E=E_2-E_1$ is the resonance defect.

Assuming that the PL intensity is proportional to the charge transfer probability $P(t)$ and the levels of the attachment centers in resonance $(\Delta E\approx 0)$, the experimentally observed oscillations make it possible to estimate the exchange potential as $V_0\approx 10^{-12}$ eV.

In summary, in the present letter the decay kinetics of the photoluminescence of PS samples subjected to rapid high-temperature carbonization with simultaneous doping with various impurities was studied. It was shown that the blue-green line (2.4 eV) of the PL spectrum in the boron-doped samples exhibits an anomalously long decay time. Another feature of these samples is the nonmonotonic character of the decrease in the intensity of the photoluminescence after the laser radiation is switched off. The experimentally observed effects can be explained by the formation of a large number of attachment centers and a built-in field of a *p–n* junction in the process of carbonization and doping. The existence and period of the oscillations can be explained by resonance tunneling between localized CSs and by the magnitude of the interaction potential. The anomalously long decay time of the PL of carbonized PS, together with its stable optical properties,[7] can facilitate control of the long-lived nonequilibrium states and give rise to a population inversion in a particular material.

This work was financed by ‘‘Russian universities—fundamental studies’’ and ‘‘Radiotekhnika’’ State Committee on Schools of Higher Education grants, and by the Russian Fund for Fundamental Research (97-02-16710).

[1] K. Nobuyoshi, O. Tsuyishi, and S. Xia, Jpn. J. Appl. Phys., Part 2 , Pt. 2, **34**, L705 (1995).

[2] I. Schirone, G. Sotgin, and F. Rallo, Nuovo Cimento D **18**, 1225 (1996).

[3] M. Akiro, K. Manabu, and A. Hidekazu, Jpn. J. Appl. Phys., Pt. 1, **34**, 5840 (1995).

[4] A. Takazawa, T. Tamuro, and M. Yamada, J. Appl. Phys. **75**, 2489 (1994).

[5] P. K. Kashkarov, E. A. Konstantinova, S. A. Petrov *et al.* Fiz. Tekh. Poluprovodn. **31**, 745 (1997) [Semiconductors **31**, 639 (1997)].

[6] L. L. Fedorenko, A. D. Sardarly, É. B. Kaganovich *et al.*, Fiz. Tekh. Poluprovodn. **31**, 6 (1997) [Semiconductors **31**, 4 (1997)].

[7] B. M. Kostishko, Sh. R. Amtazhanov, and S. N. Mikov, Pis'ma Zh. Tekh. Fiz. **24**(16), 24 (1998) [Tech. Phys. Lett. **24**, 633 (1998)].

[8] T. Matsumoto, M. Daimon, T. Futagi *et al.*, Jpn. J. Appl. Phys., Pt. 2, **31**, L619 (1992).

[9] M. E. Kompan and I. Yu. Shabanov, Fiz. Tverd. Tela (St. Petersburg) **39**(7), 1165 (1997) [Phys. Solid State **39**, 1030 (1997)].

[10] É. Yu. Buchin, A. V. Postnikov, A. V. Prokaznikov *et al.*, Pis'ma Zh. Tekh. Fiz. **21**(1), 60 (1995) [Tech. Phys. Lett. **21**, 27 (1995)].

[11] K. W. Sulston, A. T. Amos, and S. G. Davison, Phys. Rev. B **37**, 9121 (1988).

Translated by M. E. Alferieff

TECHNICAL PHYSICS LETTERS VOLUME 25, NUMBER 3 MARCH 1999

Determination of the relaxation time of a gas–liquid mixture

V. G. Kovalev, M. B. Rigina, and V. N. Tsurkin

Institute of Pulsed Processes and Technologies, Ukrainian National Academy of Sciences, Nikolaev

(Submitted December 30, 1998)
Pis'ma Zh. Tekh. Fiz. **25**, 21–26 (March 26, 1999)

The relaxation time of a gas-liquid mixture is estimated. A new widely applicable Rayleigh-type equation for the dynamics of an interphase boundary in the field of a square pressure wave is integrated for various values of the initial bubble radius and wave loading. It is shown that the model of an equilibrium medium can be used to describe electric-explosion processes in real gas-liquid mixtures. © *1999 American Institute of Physics.* [S1063-7850(99)02003-0]

Dynamical processes in two-component gas-liquid mixtures can be described in an equilibrium model provided that the characteristic time of these processes is much longer than the relaxation time of the components of the relevant mixture. For time-dependent signals with a short rise time the relevant time is the interval between the instantaneous change in pressure and the establishment of the corresponding equilibrium density, which for bubble liquids is completely determined by the pulsations of the gas bubbles.

Let us consider the process by which a single bubble establishes a new equilibrium radius in a liquid loaded by a wave with a step profile. We shall conventionally divide this process into two stages. In the first stage adiabatic compression of the bubble occurs, damped oscillations arise, and finally an equilibrium adiabatic radius and a corresponding density are established. Only mechanical equilibrium is attained, the gas temperature in the bubble remaining higher than the temperature of the surrounding medium. However, thermodynamic equilibrium is established at the second stage, where the radius decreases to the isothermal value at a very slow rate, so that acoustic and viscous effects can be neglected.

To describe the first stage of the process correctly let us estimate the basic characteristics of the second stage: We shall use similarity methods[1] to determine the characteristic time τ for establishment of thermal equilibrium, writing the heat-conduction equation for the case of spherical symmetry in the form

$$\frac{\langle T\rangle}{\langle R^2\rangle}+\frac{2\langle T\rangle}{\langle R^2\rangle}=\frac{\langle T\rangle}{a^2\tau},\quad \text{or}\quad \tau=\frac{\langle R^2\rangle}{3a^2}, \tag{1}$$

where a is the thermal diffusivity.

The characteristic equilibrium adiabatic bubble radius R_a in the second stage is related to the initial radius R_0 and the excess applied pressure δP by

$$R_a=R_0\left(\frac{P_0}{P_0+\delta P}\right)^{1/3\gamma}, \tag{2}$$

where P_0 is the hydrostatic pressure, γ is the adiabatic index, and the final isothermal radius R_i is given by

$$R_i=R_0\left(\frac{P_0}{P_0+\delta P}\right)^{1/3}. \tag{3}$$

The expressions (1)–(3) make it possible to determine the characteristic time of the second stage $\tau=(R_0/3a^2)\times[P_0/(P_0+\delta P)]^{2/(3\gamma)}$, the relative change in the bubble radius $\delta R=(R_a-R_i)/R_i$, and the average velocity of the bubble wall $v=\delta RR_i/\tau$. The computational results for various values of the bubble radius R_0 and excess pressure δP are presented in Table I.

The quantity δR, which depends only on the pressure, is quite large for high pressures. For this reason it may be necessary to take account of the compression process when investigating, for example, the expansion of a cavity in a liquid with the natural gas saturation. The rates of compression in most cases are low, but for small bubbles and high pressures dynamic effects apparently cannot be neglected. Moreover, if the characteristic time of the second stage is comparable to the relaxation time of the medium, then the process cannot be divided into two stages; compression and heat transfer will occur simultaneously. However, this does not complicate the mathematical model of the pulsations, since the process can be described by similar equations of polytropic compression of a bubble with a polytropic exponent falling between the adiabatic and isothermal values (the determination of its value is a separate problem).

Let us now consider the first stage, adiabatic or polytropic pulsations. The expression obtained in Ref. 2 for the damping rate in the linear approximation,

$$\beta_{\mathrm{L}}=\left(\frac{4\eta}{\rho_0R_0^2}+\frac{3\gamma P_{0\mathrm{g}}}{\rho_0c_0R_0}\right)\Bigg/\left[2\left(1+\frac{4\eta}{\rho_0c_0R_0}\right)\right], \tag{4}$$

where η is the dynamic viscosity coefficient, ρ_0 is the density of the liquid, c_0 is the unperturbed sound speed in the liquid, and P_{0g} is the gas pressure in a bubble, can be simplified as

$$\beta_{\mathrm{L}}=\frac{2\eta}{\rho_0R_0^2}+\frac{3\gamma P_{0\mathrm{g}}}{2\rho_0c_0R_0} \tag{5}$$

and then used to analyze the nonlinear process, since even for the minimum value $R_0=1\,\mu\mathrm{m}$ for water $4\eta/(\rho_0c_0R_0)=0.003$.

TABLE I.

Determined parameters	R_0, μm	$\delta P \cdot 10^{-5}$, Pa			
		1	10	50	100
τ, μs	50	30	13	6.4	4.6
v, m/s		0.09	0.43	0.96	0.13
τ, μs	10	1.2	0.5	0.26	0.2
v, m/s		0.45	2.2	4.8	6.2
τ, μs	5	0.3	0.13	0.06	0.05
v, m/s		0.9	4.3	9.6	13
τ, μs	1	0.01	0.005	0.003	0.002
v, m/s		4.5	22	48	64
δR	Arbitrary	0.07	0.26	0.45	0.55

TABLE II.

Regime parameters	i	R_i/R_{i-1}	t_i, μs	β_i, μs^{-1}	β_L, μs^{-1}
$R_0 = 50$ μm	1	0.27	1.58	0.037	
$P = 1$ MPa	2	0.30	4.5	0.032	
	3	0.33	7.3	0.032	0.0317
	4	0.35	10.1	0.0318	
$R_0 = 10$ μm	1	0.420	0.43	1.41	
$P = 10$ MPa	2	0.493	0.94	0.41	
	3	0.506	1.45	0.40	0.396
	4	0.508	1.96	0.40	

The first term in Eq. (5) gives the contribution of viscous effects to the damping and the second term describes radiation effects (radiation of waves into the liquid). Considering their ratio, even for comparatively low pressures, for example, $P_{0\text{g}} = 0.14$ MPa for $R_0 = 10\,\mu$m, it is found that the contribution of radiation effects becomes dominant. This means, first and foremost, that the nonlinear Rayleigh equation, where radiation effects are absent by definition, is not suitable for estimating the relaxation time of the medium for in the range of values of P_{0g} and R_0 of interest to us.

We shall examine next the nonlinear damping based on the equation of pulsations in an alternating pressure field:[3,4]

$$R\ddot{R}\left(1+\frac{P_1}{\rho_0 C_1^2}-\frac{\dot{R}}{C_1}+\frac{\dot{R}^2}{2C_1^2}\right)+\frac{3}{2}\dot{R}^3\left(1-\frac{\dot{R}}{3C_1}\right)$$

$$=\frac{P_1}{\rho_0}\left(1+\frac{\dot{R}_1}{C_1}\right)+\frac{R\dot{P}_1}{\rho_0 C_1}, \tag{6}$$

$$P_1=P_0\left(\frac{R_0}{R}\right)^{3\gamma}-P_0-P, \quad c_1=c_0+\dot{R}.$$

Analysis of the plots obtained as a result of solving Eq. (6) numerically in the case of loading by a square pressure wave made it possible to distinguish two types of pulsations.[5] Pulsations of the first type, which are nearly linear, are characteristic of bubbles with a comparatively large initial radius and small excess pressures (i.e., from among the cases considered, $R_0 = 10\,\mu$m, $R_0 = 50\,\mu$m, and $\delta P \leqslant 3$ MPa). Pulsations of the second type, which occur at high pressures for bubbles less than 10 μm in size and for comparatively small bubbles, are characterized by strongly nonlinear pulsations accompanied by a large energy losses and subsequent quite prolonged small linear oscillations around the position of equilibrium (their decay time can be neglected when determining the relaxation time of the density).

Let us now introduce the concept of the damping rate of the *i*th pulsation:

$$\beta_i=\frac{1}{t_{i+1}-t_i}\ln\left(\frac{R_i-R_a}{R_{i+1}-R_a}\right) \tag{7}$$

and compare its value with the linear damping β_L (5) for two characteristic pulsation regimes. The computational results are presented in Table II.

As one can see, when the medium relaxes by a process of the second type it can indeed be assumed that the new equilibrium value of the density is established even after the first pulsation of a bubble. Since the damping rate of the first, strongly nonlinear, pulsation is several times greater than the linear value (5), the quantity $t_\beta = 1/\beta_\text{L}$ characterizes the relaxation time of the bubble medium with an adequate margin.

Since for small bubbles radiation effects make the main contribution to damping,[2] the condition for the equilibrium approximation to be correct can be written in the form

$$P > \frac{2\rho_0 c_0 R_0}{3\gamma t \beta}. \tag{8}$$

If it is required that the relaxation time of the medium be less than 1 μs, then for bubbles with radius 15 μm we obtain from Eq. (8) the condition $P > 10$ MPa. This makes it possible, for example, to use the model of an equilibrium medium to describe the hydrodynamics of an electric explosion in a bubble gas-liquid medium with natural gas saturation, where $R_0 \leqslant 15\,\mu$m (Refs. 6,7).

[1] L. I. Sedov, *Similarity and Dimensional Methods in Mechanics* (Academic Press, New York, 1959, translation of the 4th Russian edition; Russian original, Nauka, Moscow, 1977, 438 pp.).

[2] A. A. Gubaĭdullin, A. I. Ivandaev, R. I. Nigmatulin *et al.*, Itogi nauki i tekhniki, VINITI, Mekh. Zhid. i Gaza **17**, 160 (1982).

[3] V. G. Kovalev, Akust. Zh. **40**(4), 606 (1994) [Acoust. Phys. **40**, 537 (1994)].

[4] N. M. Beskaravaĭnyĭ, V. G. Kovalev, and E. V. Krivitskiĭ, Zh. Tekh. Fiz. **64**(2), 197 (1994) [Tech. Phys. **39**, 224 (1994)].

[5] V. G. Kovalev, M. B. Rigina, and V. N. Tsurkin, in *Abstracts of Reports at the 2nd Scientific School on Pulsed Processes in the Mechanics of Continuous Media*, Nikolaev, 1996, p. 37.

[6] V. G. Kovalev, M. B. Rigina, and V. N. Tsurkin, in *Abstracts of Reports at the Scientific and Technical Conference on Electric Discharge in Liquids and Its Applications in Industry*, Nikolaev, 1992, p. 78.

[7] N. M. Beskaravaĭnyĭ, V. G. Kovalev, and M. B. Rigina, Inzh.-Fiz. Zh. **67**(1-2), 54 (1994).

Translated by M. E. Alferieff

Mechanism for microwave pulse shortening in a relativistic BWT

S. D. Korovin, G. A. Mesyats, I. V. Pegel', S. D. Polevin, and V. P. Tarakanov

Institute of High-Current Electronics, Siberian Branch of the Russian Academy of Sciences, Tomsk

(Submitted November 3, 1998)
Pis'ma Zh. Tekh. Fiz. **25**, 27–36 (March 26, 1999)

It is shown that reduction in the pulse length in a relativistic BWT, is accompanied by the appearance of explosive-emission plasma on the surface of the ripples of the slow-wave system. Generation stops because electrons emitted by the plasma absorb the electromagnetic wave. This absorption is sharply enhanced by the presence of ions emitted from the plasma. © *1999 American Institute of Physics.* [S1063-7850(99)02103-5]

In relativistic microwave generators powered by high-current relativistic electron beams (REBs), the microwave pulse length is observed to be limited to 10^{-8}–10^{-7} s[1–4] for hf electric field intensities 10^5–10^6 V/cm on the surface of the electrodynamic system. The pulse length decreases with increasing radiation power, so that the energy in the pulse remains approximately constant. At the present time, the maximum energy in microwave pulses of relativistic generators is at most a few hundred joules.

The range of possible reasons for this phenomenon is quite wide.[4–9] For Cherenkov devices with a guiding magnetic field and pulse lengths ~ 10 ns, for which the displacement of the cathode and collector plasmas is negligible, the plasma formed on the surface of the slow-wave system by an intense hf electric field apparently plays the main role in pulse shortening. The source of the plasma could be explosive-emission centers as well as gas desorbed from the surface and ionized by secondary-emission and scattered electrons.

In a 3-cm relativistic backward wave tube (BWT) with a TM_{01} working mode, a ~ 10 ns limit on the pulse length has been observed even at power levels ~ 300 MW (Ref. 2). As a possible explanation the authors suggested explosive emission of electrons from the surface of the slow-wave structure and the formation of an electron load.

In the 3-cm 3-GW relativistic BWT[3] the microwave pulse length was only 6 ns. The pulse length was inversely proportional to the pulse power, so that the energy in the pulses remained at the level 20 J. Traces of erosion, just like those on the surface of the metallic explosive-emission cathodes, were observed on the surface of the slow-wave structure of the BWT at locations of the maximum electric field strength. This indicates that microwave pulse shortening is associated wth explosive emission on the surface of the electrodynamic system of the generator.

The present work is devoted to the experimental and numerical investigation of the processes limiting the length of the radiation pulses from a 3-cm relativistic BWT under conditions such that the influence of the motion of the cathode and collector plasmas can be neglected.

The experimental investigations were performed on the Sinus-6 high-current electron accelerator with an 18-ns current pulse. A uniform relativistic BWT with a TM_{01} working mode and radiation wavelength $\lambda \approx 3.3$ cm was used. The slow-wave structure of the BWT consisted of individual ripples (stainless steel rings). The length of the slow-wave structure was $L = 9d$, the ripple amplitude $l \approx \lambda/15$, the average radius $R \approx \lambda/2$, and the period $d \approx \lambda/2$. The tube was evacuated to 10^{-4} Pa with a vapor-oil pump.

In the optimal generation regime (cathode voltage $U = 600$ kV, beam current $I = 4.7$ kA, magnetic field intensity 26 kOe) the radiation power was about 500 MW. At this microwave power level the shortening of the microwave pulse does not yet occur under ordinary conditions (Fig. 1 and also Ref. 3). To check the effect of explosive emission on the pulse length, one of the ripples of the slow-wave structure was replaced by a ripple of the same shape but with a ring-shaped graphite insert (Fig. 2). The presence of graphite in the rippled waveguide did not change the electrodynamic properties of the guide; it merely facilitated the conditions for the development of explosive-emission processes. The shape of the cathode voltage and REB current pulses remain the same.

The installation of a ripple with an insert produced shortening of the microwave pulse. The shortening was greatest when the ripple was located near the center of the slow-wave structure (Fig. 3). The length of the microwave pulses was partially restored as the number of pulses produced without breaking the vacuum of the system increased. This is probably due to the degradation of the explosive-emission capacity of graphite as a result of conditioning by the hf field. Further shortening of the first few pulses correlated with the larger number of pulses required for partial restoration of the pulse length (Fig. 3).

When the microwave pulse became shorter, an intense flux of electrons moving along the magnetic field lines was observed in the gap between the ripples near the ripple with the insert. Imprints on a lucite witness plate (Fig. 2) attest to a high current density (~ 1 kA/cm^2), which only explosive electron emission can produce.

In the theoretical analysis it was assumed that the shortening of the microwave pulse in the presence of explosive-emission plasma occurs as a result of the cessation of the generation process as a result of the absorption of the working electromagnetic wave. It was assumed that the plasma has no effect on the electrodynamic properties of the slow-

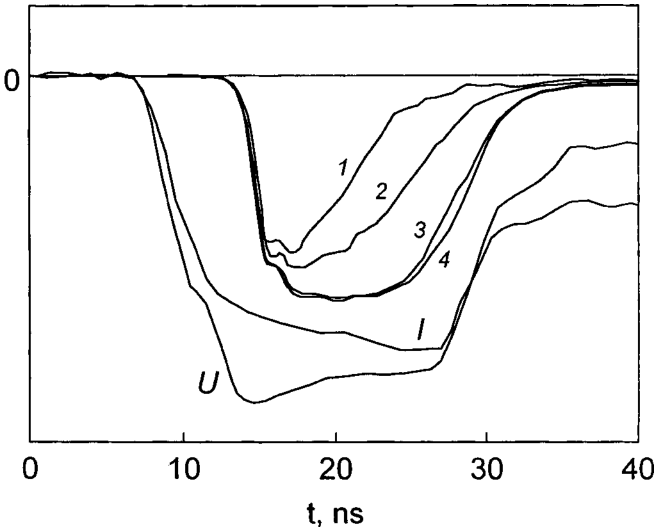

FIG. 1. Oscillograms of the beam current *I*, voltage *U* in the diode, and signals from the microwave detector (the first pulse after a ripple when a graphic insert is installed): 1 — insert at the fourth ripple from the constriction reducing the transverse size below cutoff, 2 — at the eighth ripple, 3 — at the first ripple, 4 — no insert.

wave structure. In this formulation of the problem the cessation of generation in the BWT in the presence of partial absorption of the wave could be due to an increase in the critical current of the generator below which generation stops. The solution of the one-dimensional time-dependent problem by the PIC method[10] showed that the critical current of the BWT equals the starting current. The latter current, as is well known, increases with wave absorption.

The effect of linear absorption (the absorbed power is proportional to the wave power) was investigated in one-dimensional calculations. Both compact and distributed (along the tube) absorbers, which were switched on at a given moment in time, were simulated. The calculations showed that under typical conditions with the beam current initially two to three times greater than the starting current the oscillations decay in several nanoseconds, provided that on the order of half the wave power is absorbed. The greatest effect of absorption was observed when a compact absorber was placed near the center of the slow-wave structure. In this case, for a classical tube, neglecting the copropagating wave, the expected result was observed in the limit of total wave absorption—an increase of the starting current by a factor of 8. The simulation also confirmed the obvious fact that placing a compact absorber at the edge of the slow-wave structure perturbs the internal generation process very little.

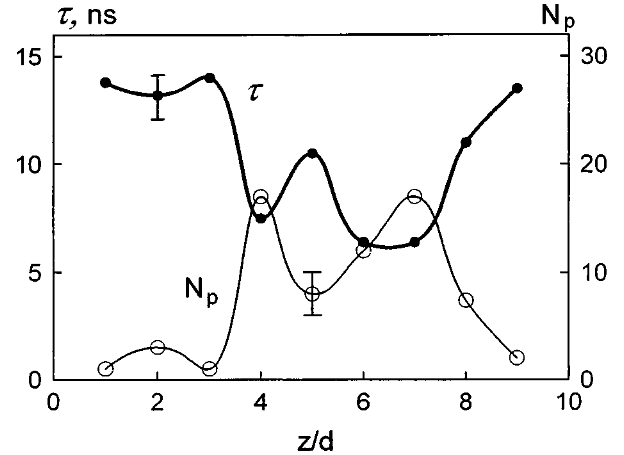

FIG. 3. Length of the first microwave pulse and number of pulses required to restore the maximum pulse length versus the distance between the graphite insert and the constriction reducing the transverse dimension below cutoff (as a fraction of the ripple period).

The electrons emitted from the plasma formed on the surface of the ripples can cause the wave to be absorbed in the BWT. At the same time, it is easy to see that the nonlinear character of purely electron absorption makes it insufficient for cessation of generation. Indeed, to change the starting current of the BWT the ratio of the power losses $P_{\rm loss}$ to the power P_w transported by the wave must be finite with weak hf fields. The intensity of the absorption of the wave by the electrons is proportional to the emission current density $j_{\rm em}$ and the energy ε picked up by the electrons in the field of the wave. If the field of the wave is weak the electron motion can be assumed to be nonrelativistic. Then the space-charge-limited current density satisfies $j_{\rm em}\propto E^{3/2}$ and the electron energy satisfies $\epsilon\propto E^2$, where E is the intensity of the electric field of the wave. Thus $P_{\rm loss}\propto E^{5/2}$. Since the wave power satisfies $P_w\propto E^2$, we have $P_{\rm loss}/P_w\propto E^{3/2}\rightarrow 0$ in the limit $P_w\rightarrow 0$. Thus a pure electron load cannot influence the starting current of a BWT.

Moreover, the presence in the system of a high-currrent electron beam with a potential $\sim 10^5$ V relative to the waveguide wall must be taken into account. When the microwave power drops below a certain level, the electric field of the wave pulling electrons from the surface of the slow-wave structure is exactly balanced by the static field of the beam, making electron emission impossible.

Nonetheless, the absorption of the electromagnetic wave makes it possible to explain the cessation of generation, because ions can be pulled out of the plasma on the surface of

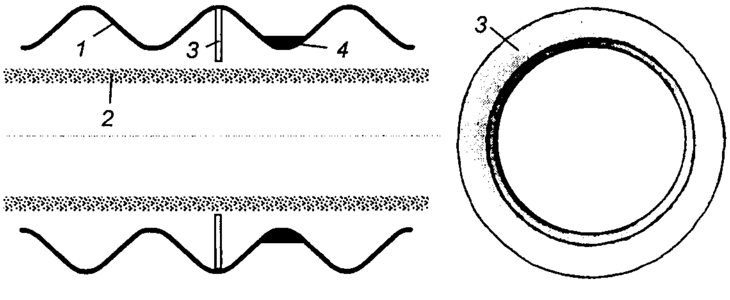

FIG. 2. Plot of the electron current between the ripples and the circuit used to obtain it. 1 — ripple of the slow-wave structure, 2 — REB, 3 — lucite witness plate, 4 — graphite insert.

the ripples during the corresponding phases of the hf field. The cyclotron radius for ions is much larger than for electrons, and it can be comparable to the tranverse size of the waveguide. For this reason the ions are accelerated initially in a direction toward the axis of the apparatus by the static field of the REB, tending to cancel the space charge of the beam. The number of singly charged ions per unit length of the system must be $\sim 10^{12}$ cm^{-2} in order to neutralize the space charge of a REB with a 5 kA current. Estimates and a numerical experiment showed that for protons and carbon ions the neutralization process lasts for several nanoseconds.

As a result of the neutralization of the space charge of the REB, the electric field pulling electrons from the surface of the electrodynamic system increases up to the total amplitude E_0 of the wave field. This hastens the appearance of new emission centers. The $t^{3/2}$ growth of the current of individual emission centers in time must also be included as one of the factors giving rise to avalanche-like development of explosive emission.

As they execute radial motion the ions accumulate in the space between the ripples. This is due primarily to the presence of an electron current here. The electrons emitted from ripples under the action of the microwave field move along the field lines of the external longitudinal magnetic field. We note that in a typical (not oversize) relativistic BWT with electric field strength 10^5–10^6 V/cm on the ripples, electrons can be transported from one ripple to another in one period of the microwave oscillations. Since the electron current is space-charge limited, the electrons produce in the gap between the ripples a quasistatic field of order E_0 averaged over one period of the oscillations. The motion of the ions in this field is accelerated, and estimates and numerical experiment show that the ions fill the gap between the ripples within several nanoseconds. The process can be characterized as hf ambipolar diffusion of ions and electrons. We note that ion accumulation between the ripples can also occur under the action of the hf field alone. Then, however, the longitudinal motion of the ions is cyclic drift motion and the duration of the process is hundreds of nanoseconds.

As a result of filling the gap with ions, a quasilinear plasma forms between the ripples. The space charges of the electron and ion components averaged over one period of the microwave oscillations cancel out, and the plasma density grows in time under the action of the field of the wave. In the process the power carried to the walls by the electron component of the plasma increases. A model time-dependent calculation for a 1-cm wide one-dimensional planar gap with an applied 10-GHz 500-kV/cm ac electric field showed that in the presence of unidirectional electron emission and space-charge limitation of the current the intensity of the electron bombardment of the walls is 28.5 MW/cm^2 (for comparison, the intensity of an electron beam with a constant applied voltage of the same magnitude is 380 MW/cm^2). When proton emission with current density 10, 100, and 1000 A/cm^2 was introduced, the average bombardment intensity increased to 0.13, 0.5, and 2.2 GW/cm^2, respectively, and the ions filled the gap in 4.1, 3.2, and 2.8 ns. The maximum plasma density in the gap was limited only by the electrode emissivity, which was taken to be arbitrarily large but finite in the calculation.

Time-dependent numerical simulation of the propagation of a TM$_{01}$ wave in a sinusoidally rippled waveguide, on one ripple of which electron and ion emission was prescribed, was performed using an axisymmetric version of the 2.5- and three-dimensional completely electromagnetic PIC code KARAT.[11] The simulation showed that the maximum wave absorption (up to 50% with respect to the power) occurs 7 ns after the wave is started, and the characteristic plasma density between the ripples is $n \sim 5 \cdot 10^{11}$ cm^{-3}. As the density increases further, the wave absorption decreases, equalling 30% for $n \sim 3 \cdot 10^{12}$ cm^{-3}. This is apparently because the wave penetration into the plasma is degraded between the ripples (the skin effect). A similar phenomenon in a BWT can change the electrodynamic properties of the slow-wave structure and destroy the generation regime.

In practice, the maximum plasma density is apparently determined by the amount of matter ionized during the explosive emission. We note that neutralization of the space charge of the REB requires approximately the same number of ions as for substantial absorption of the wave, specifically, 10^{11}–10^{12} singly-charged ions per 1 cm of the system length. Ionization of several or tens of cubic microns of matter is required to produce this number of ions; this is easily achievable during explosive emission.

A full-scale numerical experiment performed using the KARAT code showed that ion–electron emission from the ripples of the slow-wave structure of the BWT, substantially reduces the generated power, until generation ceases entirely. The latter was observed when at least two emitting ripples were positioned near the center of the tube. Figure 4 illustrates the case of three emitting ripples in a BWT with initial power generation ~ 600 MW. The times when the electron and ion emission were switched on were separated in order to demonstrate their effect separately. When the electron emission is switched on, the microwave power at the exit of the tube decreases substantially, but the generation process itself does not stop and the spectrum of the oscillations remains narrow. Approximately 3 ns after the ion emission is switched on, the radiation power drops to ~ 10 MW. Broadening of the oscillation spectrum, destruction of the phase portrait of the beam characteristic for a generating BWT, and a sharp drop in the intensity of electron bombardment of the ripples are observed. The number of electrons and ions in the electrodynamic system increases with time.

As noted above, the absorption of even a substantial fraction of the energy of the wave in the generator does not shut off generation if the absorption is concentrated near the edges of the apparatus. However, from outside, such a situation with strong absorption can also appear as shortening of the microwave pulse. Thus, in the numerical experiment with fixed ion and electron emission at the first (from where the constriction causes a cutoff) period of the ripple a three-fold decrease of microwave power was obtained without cutting off generation.

In summary, pulse shortening in a relativistic BWT may be due to the appearance of explosive-emission plasma on the surface of the ripples of the slow-wave structure. Gen-

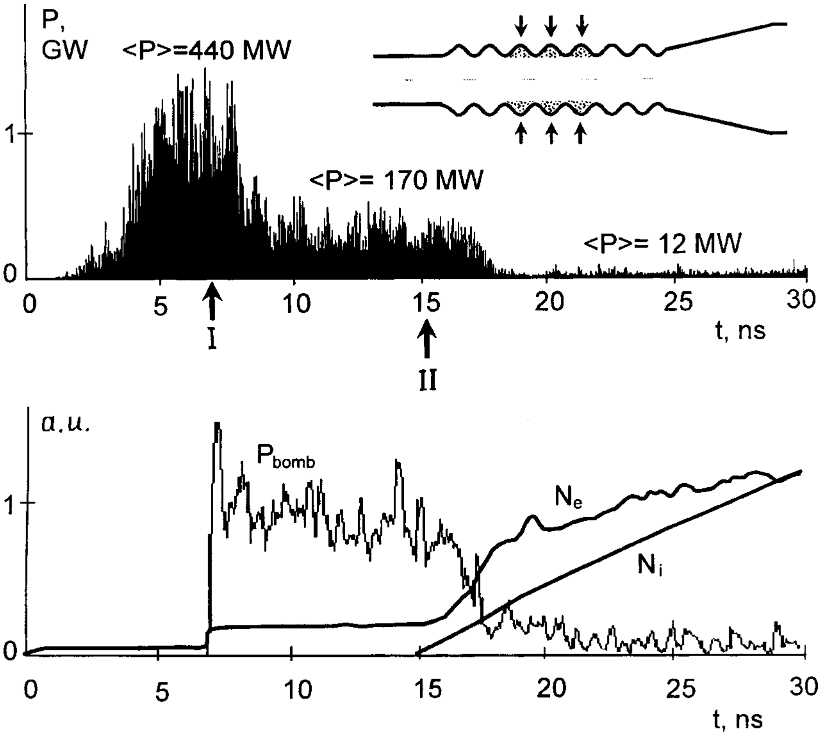

FIG. 4. Computed time dependences of the output microwave power, the intensity of electron bombardment of the ripples, and the number of electrons and ions in the BWT with emission of electrons and ions from the surface of the slow-wave structure: I — onset of electron emission, II — onset of ion emission.

eration may cease because the electromagnetic wave is absorbed by electrons emitted from the plasma. This absorption is greatly enhanced by the presence of ions emitted from the plasma. Thus, the length of the microwave pulse is limited by the development time of the explosive electron emission on the surface of the electrodynamic system and by the time for ions to fill the volume of the system.

[1] N. I. Zaĭtsev, N. F. Kovalev, G. S. Korablev *et al.*, Pis'ma Zh. Tekh. Fiz. **7**(14), 879 (1981) [Sov. Tech. Phys. Lett. **7**, 879 (1981)].

[2] A. S. El'chaninov, F. Ya. Zagulov, S. D. Korovin *et al.*, Pis'ma Zh. Tekh. Fiz. **7**(19), 1168 (1981) [Sov. Tech. Phys. Lett. **7**, 1168 (1981)].

[3] A. V. Gunin, S. A. Kitsanov, A. I. Klimov *et al.*, Izv. Vyssh. Uchebn. Zaved. Fiz. No. 12, 84 (1996).

[4] A. F. Aleksandrov, S. Yu. Galuzo, V. I. Kanavets *et al.*, in *Abstracts of Reports at the 4th All-Union Conference on High -Current Electronics*, Novosibirsk, 1982, pp. 168–171.

[5] A. F. Aleksandrov, L. G. Blyakhman, and S. Yu. Galuzo, in *Relativistic High-Frequency Electronics*, No. 3, Gor'kiĭ, 1983, pp. 219–240

[6] G. A. Mesyats, in *Proceedings of a Course and Workshop on High Power Generation and Applications*, Villa Monastera, Varenna, Italy, 1991, pp. 345–362.

[7] J. Benford and G. Benford, IEEE Trans. Plasma Sci. **25**, 311 (1997).

[8] N. F. Kovalev, V. E. Necaev, M. I. Petelin, and N. I. Zaitsev, IEEE Trans. Plasma Sci. **26**, 246 (1998).

[9] O. T. Loza and P. S. Strelkov, in *Digest of Technical Papers, International Workshop on High Power Microwave Generation and Pulse Shortening*, Edinburgh, UK, 1997, pp. 103–108.

[10] I. V. Pegel', Izv. Vyssh. Uchebn. Zaved. Fiz. No. 12, 62 (1996).

[11] V. P. Tarakanov, *User's Manual for Code KARAT*, Berkeley Research Associates, Springfield, VA, 1992.

Translated by M. E. Alferieff

Formation of a negative image by an opaque screen

Sh. D. Kakichashvili

Institute of Cybernetics, Georgian Academy of Sciences, Tbilisi

(Submitted November 24, 1998)
Pis'ma Zh. Tekh. Fiz. **25**, 37–41 (March 26, 1999)

An effect that can serve as a basis for reconciling two approaches in the description of diffraction—Fresnel's and Young's—is described.
[S1063-7850(99)02203-X]

The focusing action of a camera obscura was apparently first mentioned in the sixteenth century.[1] The formation of an image by this device is essentially completely described by the laws of ray optics. To explain the analogous effect of a circular opaque screen and an opaque sphere the wave theory of light and the Huygens–Fresnel principle must be invoked.[2] The corresponding experiment reveals a strong sensitivity to the geometry of the experiment and the precision of the circular screen.[3] Just as in a camera obscura, the image is inverted and positive.[4]

Many years ago I observed the formation of a negative image by a small opaque screen. This effect apparently did not attract any attention earlier. Using an extended light source in the form of an incandescent filament with an arbitrary configuration, a candle flame, etc., and placing in the path of the light a small opaque screen ($\leqslant 1-2$ mm), at a certain distance it is easy to observe a negative image of the source. The image formed is not critically dependent on the shape of the opaque screen (circle, triangle, square, and so on) and, just as in a camera obscura, it is inverted (Fig. 1). The smaller the screen, the higher the contrast and the clearer the image are, even relatively close to the screen. The experiment described (essentially, elementary) is virtually insensitive to the conditions and geometry of the experiment. My efforts to explain the observed effect, even qualitatively by means of the mathematical apparatus based on the Huygens–Fresnel principle, were all unsuccessful.

In the present letter I employ Young's diffraction idea for this purpose. This idea is considered to be an alternative, in a certain sense, to the Huygens–Fresnel principle. Instead of secondary spherical waves, Young postulated the appearance of so-called conical waves, reflected by the edge of the diffracting opening on both sides of this edge. The conical wave together with the directly transmitted wave form a diffraction pattern as a result of their interfering with one another. An amplitude discontinuity occurs at the edge of the screen itself. To eliminate this discontinuity Young postulated the appearance of a jump in phase by π for the part of the conical wave that is deflected into the region of the initial wave and the absence of a jump for the other part that is deflected into the shadow region (see Fig. 2).[5]

Figure 3 shows a diagram of the formation of a negative image by an opaque screen. Here $E = E_0 \exp i(\omega t + \varphi)$ is the initial, illuminating wave. According to Young, the conical waves for the outer and inner parts of an opaque screen can be written in the paraxial approximation in the form

$$E_{\text{out}} = k_{\text{out}} E \exp(-i\pi), \quad E_{\text{in}} = k_{\text{in}} E, \tag{1}$$

where the coefficients k_{out} and k_{in} describe the decrease of the amplitude of the conical wave in the regions outside and inside the shadow, respectively. These coefficients are related to the material nature of the opaque screen and in the general case can be unequal to one another. Adding the waves (1) and calculating the intensity of the resulting field we obtain

$$I_{\Sigma} = (E_{\text{out}} + E_{\text{in}})(E_{\text{out}} + E_{\text{in}})^* = E_0^2 (k_{\text{out}} - k_{\text{in}})^2. \tag{2}$$

Setting[5] $k_{\text{out}} = k_{\text{in}}$, following Rubinovich, we have for the resulting intensity $I_{\Sigma} = 0$, which uniquely describes the appearance of a negative image of the source.

It should be noted that the formation of an image by a camera obscura is also consistent with Young's diffraction idea. In this case three waves participate in the formation of the image: an undeflected wave with amplitude proportional to the area of the opening $E_H = kE$ and two waves, E_{out}, which are exterior with respect to the shadow. Under the conditions of tautochronism of the waves being superposed, which occurs for an infinite separation between the object and the opening and between the opening and the location where the image forms, and setting $k = k_{\text{out}}$, we have for the intensity of the resulting field

$$I_{\Sigma} = (kE + 2E_{\text{out}})(kE + 2E_{\text{out}})^* = k^2 E_0^2. \tag{3}$$

For different geometrical conditions of the experiment the image formed is burdened by substantial diffraction noise. This is easily observed experimentally.[1]

I also observed a similar negative image formation effect by using a small phase step of arbitrary depth and an anisotropically absorbing screen in the form of a 1 mm piece of film polarizer. A circular sample of film polarizer was placed

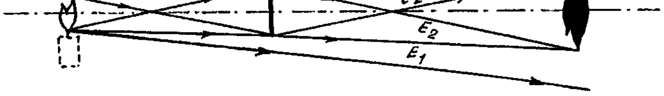

FIG. 1. Illustration of the formation of a negative image of an extended source by an opaque screen.

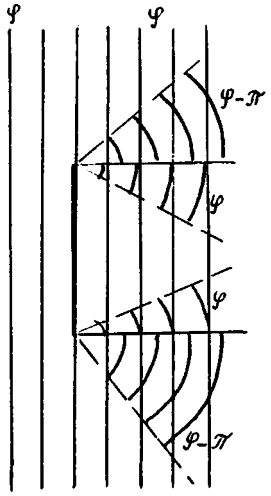

FIG. 2. Illustration of the phase jump in Young's conical wave from one side of an opaque screen to the other.

between two pieces of glass, together with an immersion liquid whose refractive index was close to that of glass and the material of the sample. The contrast of the negative image decreased sharply under illumination by linearly polarized light with the electric field vector oriented parallel to the transmission axis of the sample. The contrast of the negative image is a maximum and close to the contrast with an opaque screen for illuminating light with orthogonal polarization. The latter experiment attests unequivocally to the participation of two waves E_{out} and E_{in} in the creation of the image. More accurate quantitative measurements of the image contrast can apparently be used to determine the coefficients k_{out} and k_{in} for absorbing screens of different material nature.

A complete theory of the observed defect will be published later.

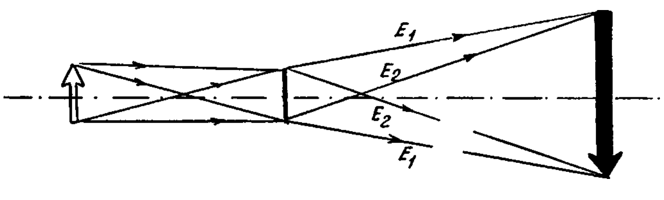

FIG. 3. Diagram of the formation of a negative image by an opaque screen.

In my opinion the effect described in the present letter can serve as a basis for reconciling the two seemingly alternative approaches in the description of optics, that of Fresnel and that of Young.

As is well known, Young's diffraction idea in its most general form consists in postulating transverse diffusion of the amplitude beyond the limits of the diffracting opening. The spreading of the amplitude of the field can be described similarly to the diffusion of heat according to a corresponding heat-conduction equation. The latter, as is well known, is very similar to the Schrödinger wave equation. The diffusion of the complex amplitude should occur with a phase shift, similarly to the phase shift introduced by Young heuristically for the phases of the conical wave. As a result of this, oscillations should arise in the distribution of the amplitude over the front and for any points of observation.

It is well known that the Huygens–Fresnel principle does not introduce any special conditions in connection with the phases of the secondary waves. However, this approach does not permit dsecribing even approximately the effect observed in the present work.

Both approaches are essentially scalar. They cannot be used to describe the diffraction of electromagnetic waves by screens with an anisotropic and gyrotropic profile. It follows unequivocally on this basis that in the future both approaches must be modified in application to the vector waves of the electromagnetic field. It now seems that the vector modification of the Huygens–Fresnel principle in application to holography,[6,7] despite the wide range of phenomena described, is not sufficiently general. The future, modified theory should not require the independent, heuristic introduction of either the Huygens–Fresnel principle or the idea of interference and should incorporate them as mathematical consequences.

I thank D. Sh. Kakichashvili and Professor E. M. Lyubimov for their interest in this work and for helpful discussions.

[1] S. Tolansky, *Optical Illusions* (Pergamon Press, New York, 1964; Russian translation, Mir, Moscow, 1969).
[2] M. Born and E. Wolf, *Principles of Optics* (Pergamon Press, New York, 1969; Russian translation, Nauka, Moscow, 1970).
[3] R. V. Pol', *Optics and Atomic Physics* (Nauka, Moscow, 1966).
[4] A. Sommerfeld, *Optics* (Academic Press, New York, 1954; Russian translation, Inostr. Lit., Moscow, 1953).
[5] A. Rubinowicz, Nature (London) **180**, 160 (1957).
[6] Yu. N. Denisyuk, Dokl. Akad. Nauk SSSR **144**(6), 1275 (1962) [Sov. Phys. Dokl. **7**, 543 (1962)].
[7] Sh. D. Kakichashvili, *Polarization Holography* (Nauka, Leningrad, 1989).

Translated by M. E. Alferieff

Model of scattering by a perturbed thin cylinder

D. A. Zubok and I. Yu. Popov

St. Petersburg State Institute of Precision Mechanics and Optics (Technical University)

(Submitted July 20, 1998)
Pis'ma Zh. Tekh. Fiz. **25**, 42–45 (March 26, 1999)

A model of wave scattering by a perturbed thin cylinder is constructed. The model is based on the theory of self-adjoint operator extensions. A method is found for choosing a model operator ensuring that the model solution is identical to the leading term of the asymptotic expansion, in terms of the small diameter of the cylinder, of the real scattering problem. © *1999 American Institute of Physics.* [S1063-7850(99)02303-4]

The problem of wave scattering by thin bodies is attracting a great deal of attention in connection with various physical applications. In this problem asymptotic expansions are constructed in terms of a small parameter (the diameter of a cylinder, the opening angle of a cone). A number of interesting results have been obtained by this method.[1,2] However, the great difficulties that often arise preclude any substantial progress, so that it is desirable to construct models that can simplify the situation.

One such modeling procedure is to apply the theory of self-adjoint operator extensions. This approach is similar to the well-known zero-range potential method in atomic physics,[3] which goes back to the work of Fermi.[4] After F. A. Berezin and L. D. Faddeev[5] showed that from a mathematical standpoint prescribing a zero-range potential signifies the construction of a self-adjoint exptension of a symmetric operator, the method gained new impetus and was applied to a much wider range of problems.[6,7] Operator extension theory has been used to obtain a correct mathematical description of the Laplace operator perturbed on a set of zero measure.[8–11] In the present letter a model of wave scattering by a thin cylinder perturbed in a bounded region is constructed on the basis of an analysis of the three-dimensional Laplace operator perturbed on a line. The model solution is compared with the asymptotic (in terms of the cylinder diameter) solution of the real problem and a method is indicated for choosing the model parameters so as to ensure that the solution coincides with the leading term of the asymptotic expansion. Thus, the abstract mathematical scheme has found a specific physical application.

Let us briefly describe the model. Let L be the Z axis of a cylindrical coordinate system. We start with the Laplace operator A_L restricted to a set of functions that vanish on L. Here A_L is a symmetric operator with infinite deficiency indices. To construct its self-adjoint extension it is necessary to consider the domain of the adjoint operator, which can be represented as

$$\mathcal{D}(A_L^*)=\mathcal{D}(A_L^F)\dot{+}N_{\lambda_0} \tag{1}$$

where A_L^F is the Friedrich extension of the operator A_L, N_{λ_0} is the kernel of the operator $A_L^*-\lambda_0$, $\lambda_0=k_0^2<0$, and λ_0 is a regular value of the operator. It is easy to find that the subspace N_{λ_0} consists of the functions v of the form

$$v(r,\varphi,z)=(2\pi)^{-3/2}\int_{-\infty}^{\infty}e^{iz\xi}\frac{i}{4}H_0^{(1)}(\sqrt{k_0^2-\xi^2}r)\alpha(\xi)d\xi, \tag{2}$$

where $\alpha(\xi)$ is a function in the Sobolev space $H_{-1}(\mathbf{R})$. To construct the domain of the self-adjoint extension of the operator A_L it is necessary to separate in $\mathcal{D}(A_L^*)$ a line on which the following ''boundary form'' vanishes:

$$Y(u,v)=(A_L^*u,v)-(u,A_L^*v)=0.$$

In accordance with the representation (1),

$$u=u_0+u_L,\quad u_0\in H_2=\mathcal{D}(A_L^E),\quad u_L\in N_{\lambda_0}.$$

Using Eq. (2) we obtain

$$J(u,v)=\int_{-\infty}^{\infty}(\alpha_u^+(s)\overline{\alpha_v^-(s)}-\alpha_u^-(s)\overline{\alpha_v^+(s)})ds. \tag{3}$$

Here α^+ is α from Eq. (2) and $\alpha_u^-(s)=u_0(s)$. Using the theory of simplectic forms,[12] we can construct all classes of possible extensions. We shall not present this description here. We merely note the extensions that are distinguished by the condition

$$\alpha_u^+(z)=\int_{-\infty}^{\infty}B(z,z')\alpha_u^-(z')dz', \tag{4}$$

where $B(z,z')$ is a symmetric kernel.

In Ref. 1 the leading term u^0 of the asymptotic expansion in terms of the small radius was obtained for the problem of scattering of a plane wave by a thin cylinder perturbed in a bounded region:

$$u^0(r,z)=\frac{\pi}{2i}\int_{-\infty}^{\infty}H_0^{(1)}(\sqrt{k^2-\xi^2}r)\nu(\xi)e^{iz\xi}d\xi,$$

where $\nu(\xi)$ satisfies the equation

$$\ln(\tilde{\varepsilon}\sqrt{k^2-\xi^2})\nu(\xi)+\int_{-N}^{N}\gamma(\xi-t)\nu(t)dt=-\tilde{h}(\xi)\eta\left(\frac{\xi}{N}\right). \tag{5}$$

Here $|\xi|<N=\varepsilon^{-1+\delta}$, $0<\delta<1, \eta(\xi/N)$ is the characteristic function of the segment $[-1,1]$,

$$\ln\tilde{\varepsilon}=\ln\varepsilon+\frac{\pi}{2i}-\ln 2-\psi(1), \quad \gamma(\xi)=F(\ln\Phi)(\xi), \quad \tilde{h}=Fh,$$

F is the Fourier transform, the function Φ gives the shape of the cylinder, and h is the value of the incident wave on the cylinder.

The corresponding model problem can be solved explicitly and leads to an integral equation similar to Eq. (5). Comparing the results shows that in selecting the extension (4) with the kernel $\beta(\xi,\xi')=B(\xi-\xi')=(2i/\pi)F(\ln\Phi)$ and the parameter $k_0=(2i/\varepsilon)e^{\psi(1)}$ we obtain a model solution that is identical to the leading term of the asymptotic expansion of the real solution.

The correspondence obtained above opens up the possibility of further using the model for investigating resonances, analyzing the problem of diffraction by a narrow slit of variable width, and so on.

This work was supported by a grant from the Russian Fund for Fundamental Research.

[1] M. V. Fedoryuk, Izv. Akad. Nauk SSSR **49**, 160 (1985).

[2] V. M. Babich, B. A. Samokish, and D. B. Dement'ev, Zapiski nauchn. semin. POMI RAN **221**, 151 (1996).

[3] Yu. N. Demkov and V. N. Ostrovskiĭ, *Method of Zero-Radius Potentials in Atomic Physics* [in Russian] (Leningrad State University Press, Leningrad, 1975), 240 pp.

[4] E. Fermi, Ric. Sci. **7**, 13 (1936).

[5] F. A. Berezin and L. D. Faddeev, Dokl. Akad. Nauk SSSR **137**, 1011 (1961) [*sic*].

[6] S. Albeverio, F. Gesztesy, R. Hoegh-Krohn, and H. Holden, *Solvable Models in Quantum Mechanics* (Springer, Berlin, 1988), 430 pp.

[7] B. S. Pavlov, Usp. Mat. Nauk **42**(6), 99 (1987).

[8] A. S. Blagoveshchenskiĭ and K. K. Lavrent'ev, Vestn. LGU, No. 1, 9 (1977).

[9] I. Yu. Popov, J. Math. Phys. **33**, 3794 (1992).

[10] Yu. G. Shohdin, Teor. Mat. Fiz. **105**(1), 3 (1995).

[11] W. Karwowski and V. Koshmanenko, J. Funct. Anal. **143**, 205 (1997).

[12] L. Hormander, *The Analysis of Linear Partial Differential Operators. 3. Pseudodifferential Operators* (Springer-Verlag, New York, 1985), 485 pp.

Translated by M. E. Alferieff

Effect of an inert medium on the formation of ordered states in $YBa_2Cu_3O_x$

I. V. Zhikharev, S. I. Khokhlova, and N. E. Pis'menova

A. A. Galkin Donetsk Physicotechnical Institute, Ukrainian National Academy of Sciences

(Submitted October 5, 1998)
Pis'ma Zh. Tekh. Fiz. **25**, 46–48 (March 26, 1999)

Ordered structures were produced in $YBa_2Cu_3O_x$ ceramic samples with oxygen index $x = 6.75$ in an argon atmosphere as a result of isothermal holding. The ordering is clearly manifested in the dependence of the volume P of the superconducting phase and the room-temperature conductivity σ on the isothermal holding temperature. The effect of an inert medium, in contrast to air, is to displace the temperature interval where the ordered state with $x = 6.75$ is formed to lower isothermal holding temperatures 188–225 °C (instead of 350–400 °C).

[S1063-7850(99)02403-9]

The experimental arrangement was similar to that described in Ref. 1, i.e., ten samples prepared from the same ceramic block $YBa_2Cu_3O_x$ with $x = 6.86$, were isothermally held for 5 h in an argon atmosphere at various temperatures. The isothermal holding temperature prescribed for each sample was reached in 2 h. Next, the samples were cooled slowly, which made it possible to maintain the oxygen concentration established at the temperature during the holding process: constant-stoichiometry (CS) samples.[2] The values of the oxygen index were obtained by x-ray analysis from the correlation of the lattice parameters $c/3 - b$ (Ref. 3).

The volume of the superconducting phase was determined from magnetic measurements, taking account of the porosity of the samples and the penetration depth of the magnetic field.[4]

Just as in the case of heating of $YBa_2Cu_3O_x$ samples in air, a correspondence is found between the anomalies of $\sigma(T_1)$ and $x(T_1)$ (T_1 is the isothermal holding temperature). The maximum values of $\sigma(T_1)$ correspond to a definite value $x = 6.75$, kindicating the formation of ordered superstructures (see Fig. 1). The formation of ordered states results in an appreciable decrease of the scattering of charge carriers, since in this case the defects become elements of the periodic structure.

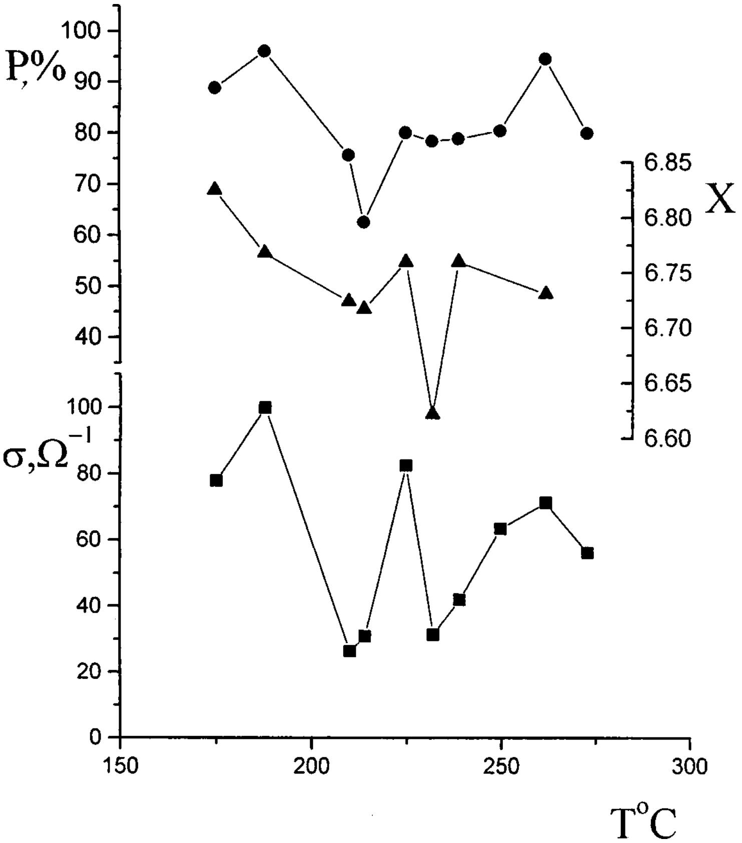

FIG. 1. Conductivity σ and oxygen index x at $T = 300$ K and the volume P of the superconducting phase at $T = 4.2$ K versus the isothermal holding temperature.

For the ordered $x=6.75$ superstructure the minimum period along the a axis is four interatomic distances.

The dependence of the volume $P(T_1)$ of the superconducting phase is very similar to $\sigma(T_1)$ (Fig. 1), since in contrast to conventional superconductors, whose superconducting characteristics show a weak dependence on the ordering of nonparamagnetic impurities, the behavior of the same characteristics in high-temperature superconductors depends strongly on the character of the ordering of these impurities.[5]

Comparing the results of isothermal holdings in air[1] and in an inert argon atmosphere shows that ordered states with $x=6.75$ form in an inert medium at lower temperatures than in air (188–225 and 350–400 °C), respectively). This is apparently thermodynamically favorable in a more oxygen-depleted medium.

Ordered states corresponding to only one oxygen index $x=6.75$ were found in the presented range of isothermal holding temperatures in argon. This opens up the possibility of obtaining ordered states with $x=6.67$ (the minimum period along the a axis is $3a$) and possibly $x=6.35$ ($2\sqrt{2a\times 2\sqrt{2a}}$ superstructure)[6] with isothermal holding temperatures much lower than the tetra-ortho transition temperature. These ordered states could not be produced in air.

In closing, it is our pleasant duty to thank B. Ya. Sukharevskiĭ for the idea of performing these experiments, N. H. Andersen for helpful comments, and G. E. Shatalova and A. Ya. Duk for determining the oxygen index.

[1] B. Ya. Sukharevskii, I. V. Zhikharev, S. I. Khokhlova *et al.*, Physica C **194**, 373 (1992).
[2] J. Reyes-Gasga, T. Krekels, S. Amelinckx *et al.*, Physica C **159**, 831 (1989).
[3] G. E. Shatalova, S. I. Khokhlova, B. Ya. Sukharevskiĭ, I. V. Zhikharev, P. N. Mikheenko, Kristallografiya **35**, 727 (1990) [Sov. Phys. Crystallogr. **35**, 424 (1990)].
[4] P. N. Mikheenko, Yu. E. Kuzovlev, and E. N. Malyshev, Zh. Tekh. Fiz. **60**(11), 104 (1990) [Sov. Phys. Tech. Phys. **35**, 1292 (1990)].
[5] B. G. Levi, Phys. Today January (1996), pp. 19–22.
[6] A. A. Aligia and J. M. Elores, Physica C **333**, 202 (1996).

Translated by M. E. Alferieff

Use of nonresonant radiation to detect spin-oriented photofragments

O. S. Vasyutinskiĭ, B. V. Picheev, and A. G. Smolin

A. F. Ioffe Physicotechnical Institute, Russian Academy of Sciences 194021 St. Petersburg, Russia

(Submitted July 3, 1998)
Fiz. Tverd. Tela (St. Petersburg) **25**, 49–54 (March 26, 1999)

A technique is proposed for detecting the anisotropy in the angular distribution of photofragment spins on the basis of the birefringence effect. A comparative analysis is made of the nonresonant method of detection with the conventional resonance absorption method. It is shown that using the Faraday effect facilitates efficient detection of high concentrations of polarized photofragments. For an optically thick layer this is an important advantage over the absorption method. Thus, the proposed method supplements the method of detection using magnetic dichroism and permits high fragment concentrations to be studied. © *1999 American Institute of Physics.* [S1063-7850(99)02503-3]

In the last few years the investigation of oriented and aligned photofragments formed through photodissociation of molecules has been attracting increasing attention from investigators, since such fragments make it possible to obtain detailed information about the dynamics of the photoprocess.[1] Studying how the polarization moments of fragments are related to other vector properties of a reaction (vector correlations) makes it possible to investigate the form and symmetry of excited states as well as interference effects and nonadiabatic interactions in the dissociating molecules.[2,3]

Earlier our group developed a method of investigating the polarization of resonant (with the absorption line of the atoms being investigated) probe radiation which has passed through a cell containing vapors of salt subjected to photolysis in the presence of an external magnetic field and tested it on oriented and aligned photofragments.[4,5] The observed signals due to the variation of the dichroism of the atomic vapors, modulated at the Larmor precession frequency, made it possible to obtain high experimental sensitivity. Contributions from dichroism and light absorption by an ensemble of the experimental particles were present in the experimental signal; this simplified the normalization. However, this method is effective only for a sufficiently low concentration of the experimental photofragments that satisfies the conditions of an optically thin layer, thereby limiting the magnitude of the observed signals. In addition, real optical transitions between the states of the fragments are used. This can distort the initial distributions of the relative populations of the magnetic sublevels of the state being investigated.

In the present work a different method of detection, employing the paramagnetic Faraday effect,[6–8] is tested. This method is based on observing the rotation of the polarization plane of linearly polarized, nonresonant, probe radiation passing through an oriented atomic vapor. As far as we know, this method has not been previously used to detect oriented photofragments.

We investigated the following reaction leading to the photodissociation of RbI molecules by pulsed circularly polarized radiation at the fourth harmonic of the Nd:YAG laser with wavelength 266 nm:

$$\mathrm{RbI}+h\nu\Rightarrow \mathrm{Rb}(6^2S_{1/2})+\mathrm{I}(5^2P_{1/2}). \qquad (1)$$

The spin-oriented rubidium atoms produced in the reaction (1) were previously investigated in Ref. 5 by the resonant absorption method. In Ref. 5 the signal due to the modulation of the circular dichroism of the absorption of the atomic vapor as a result of the precession of the atomic spins in an applied transverse magnetic field accompanying the passage of the probe radiation in the 794.8 nm D_1 line of atomic rubidium through the absorbing cell (AC) was observed. In the setup of Ref. 5 the isotopic salt $^{87}\mathrm{Rb}^{127}\mathrm{I}$ was used in the AC; an electrodeless high-frequency lamp, containing the same rubidium isotope, served as the source of the probe radiation. In the present work, salt containing the isotope $^{85}\mathrm{Rb}$ was subjected to photolysis, and a lamp containing the isotope $^{87}\mathrm{Rb}$ served as the source of probe radiation, which provided a shift of the probe radiation line relative to the absorption line. The probe radiation passed through a linear polarizer, the AC, and an additional linear polarizer crossed with the first one at an angle of 45°, as shown in Fig. 1a.

The typical experimental signals obtained after 20 laser pulses were accumulated are presented in Fig. 1b. In this figure the moment of the laser pulse corresponds to the time $t=0$. As a result of the small overlapping of the closely spaced hyperfine (HF) lines of the two rubidium isotopes, the signal contains a contribution—a ''step''—from the absorption signal. The absorption signals are damped by the recombination of atoms in the molecule and the escape of the atoms from the detection zone. The oscillating part of the signal (the orientation signal) is due to a periodic change in the birefringence of the atomic vapor as a result of the precession of atomic spins in the external magnetic field. In the experiments described, in one case the probe radiation beam propagated parallel to the laser dissociation beam and in the other case these two beams propagated at right angles to one another (Fig. 1a). It was observed that the amplitude of the orientation signals was different in these two cases. The experimental geometry affects the magnitude of the orientation

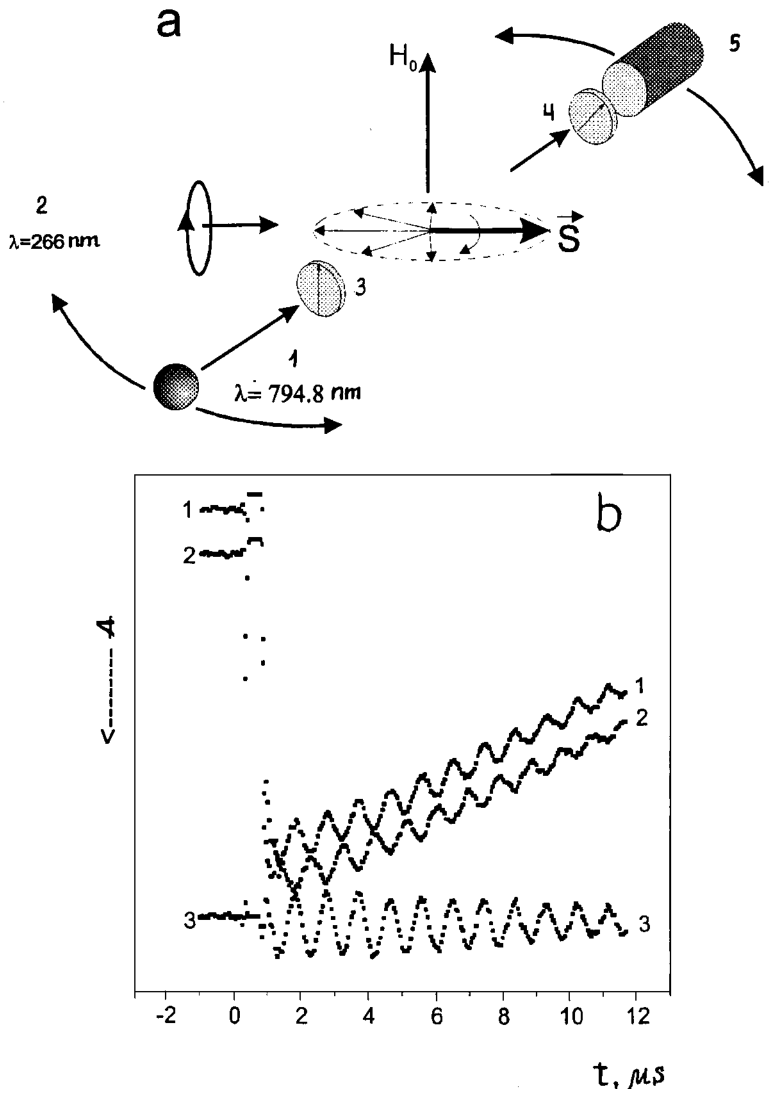

FIG. 1. a — Geometry of the experiments: 1 — Probe beam; 2 — circularly polarized dissociating beam; 3 — linear polarizer; 4 — linear analyzer; 5 — FÉ7. b — Experimental signals (absorption). The signals 1 and 2 were recorded using left- and right-circularly polarized dissociation radiation, respectively. The signal 3 is the difference of signals 1 and 2.

signals this way because the total birefringence signal is due to the precession of the orientation vectors of the two HF sublevels F_+ and F_- of the ground state of the rubidium atoms, the signals from both sublevels being added in one geometry and subtracted in the other.

Assuming that the HF of the structure of the excited $6^2P_j(j=1/2,3/2)$ states of the Rb atoms cannot be resolved for the probe radiation on the transitions $^2S_{1/2}\Rightarrow{}^2P_j$, the following expression can be obtained for the normalized orientation signals to first order in the optical thickness τ:[9]

$$\frac{U}{U_0}=\frac{\frac{11}{4}-j_e(j_e+1)}{(I+1)J^a_{F_+}+IJ^a_{F_-}}\times\left[\frac{(I+1)(2I+3)}{3(2I+1)}J^d_{F_+}\pm\frac{I(2I-1)}{3(2I+1)}J^d_{F_-}\right]\frac{1}{2}P_e\times\exp-(\Gamma t),\qquad(2)$$

where in the expression in brackets the plus sign corresponds to parallel and the minus sign to perpendicular geometry, $J^a_{F_+}$ and $J^a_{F_-}$ are the overlap integrals of the profiles of the hyperfine components of the probe radiation with the HF components of the absorption spectrum of the experimenal isotope, and $J^d_{F_+}$ and $J^d_{F_-}$ are the overlap integrals of the profiles of the HF components of the probe radiation with the dispersion contour of the experimental isotope on the transitions $F_+\Rightarrow j$ and $F_-\Rightarrow j$, respectively. The quantity $P_e=\langle S_z\rangle/S$ is the degree of initial electronic orientation of the atomic spins and $j_e=1/2$, 3/2 is the total electronic angular momentum of the excited ^2P_j state of the atoms.

The signs of the integrals $J^d_{F_+}$ and $J^d_{F_-}$ in Eq. (2) are determined by the sign of the detuning of the probe radiation frequency from the resonance absorption line. The orientation signal is greater for the perpendicular detection scheme than for the parallel scheme, as was observed in the experiment.

The ratios of the orientation signals for resonant and nonresonant detection, which are scaled to the same magnitude of the absorption signal, are presented in Fig. 2 as a function of the concentration of the molecular vapor in the AC. It is evident that as the concentration of the dissociating molecules increases, the method employing Faraday detec-

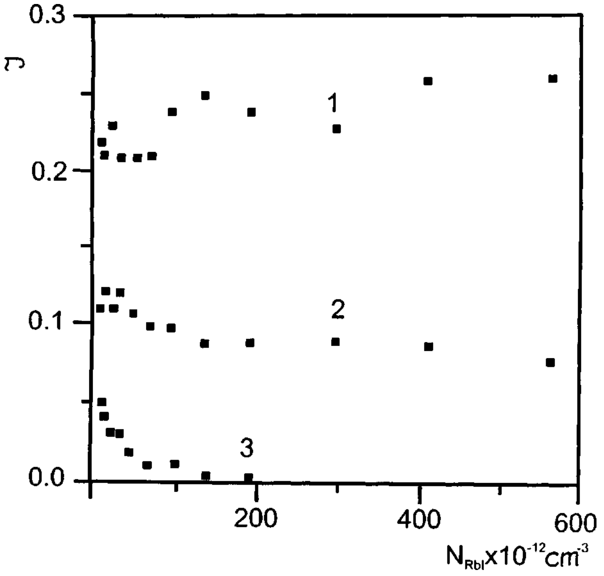

FIG. 2. Amplitudes of the orientation signals versus the density of molecules using different methods of detection: 1 — Faraday detection, perpendicular geometry; 2 — Faraday detection, parallel geometry; 3 — resonance detection, parallel geometry.

tion of oriented atoms gives much higher magnitudes of the experimental signals.

In summary, in the polarization spectroscopy of photofragments the method tested has the advantages that it is possible to detect high concentrations of oriented and aligned atoms and that the probe radiation does not influence their orientation. The use of the Faraday effect to investigate oriented photofragments can be improved by using as the source of probe radiation a tunable laser which has high radiation stability and monochromaticity and makes it possible to optimize the detection parameters with respect to the magnitude of the frequency detuning of the probe radiation from the atomic absorption line.

This work was supported by the Russian Fund for Fundamental Research under Grant 98-02-18313R.

[1] *Proceedings*, Conf. on Stereodynamics of Chemical Reactions, December 1–5, 1996, Bielefeld, Germany.
[2] O. S. Vasyutinskiĭ, Khim. Fiz. **5**, 768 (1986).
[3] M. Glass-Maugean and A. Beswick, Phys. Rev. A **36**, 1170 (1987).
[4] D. V. Kupriyanov, B. N. Sevastianov, and O. S. Vasyutinskii, Z. für Physik D; Atoms, Molecules, and Clusters **15**, 105 (1990).
[5] D. V. Kupriyanov, B. V. Picheyev, and O. S. Vasyutinskii, J. Phys. B: Atomic, Molecular, and Optical Phys. **26**, L803 (1993).
[6] C. Cohen–Tannoudji and F. Laloë, J. Phys. **28**, 505 (1967).
[7] W. Happer, Rev. Mod. Phys. **44**, 169 (1972).
[8] D. V. Kupriyanov, I. M. Sokolov, and S. V. Subbotin, Zh. Éksp. Teor. Fiz. **93**, 127 (1987) [Sov. Phys. JETP **66**, 71 (1987)].
[9] B. V. Picheyev, A. G. Smolin, and O. S. Vasyutinskii, J. Phys. Chem. A **101**, 7614 (1997).

Translated by M. E. Alferieff

Possible nonlinear heat-pulse propagation in solids at Debye temperatures

K. P. Zol'nikov, R. I. Kadyrov, I. I. Naumov, S. G. Psakh'e, G. E. Rudenskiĭ,
and V. M. Kuznetsov

Institute of the Physics of the Strength of Materials and Materials Science, Siberian Branch of the Russian Academy of Sciences, Tomsk

(Submitted November 19, 1998)
Pis'ma Zh. Tekh. Fiz. **25**, 55–59 (March 26, 1999)

Molecular dynamics techniques are used to show that heat can be transferred ballistically in three-dimensional crystalline materials at temperatures on the order of Debye temperatures.

[S1063-7850(99)02603-8]

It is well known that under certain conditions heat can propagate over macroscopic distances with a velocity on the order of sound velocity in crystals. Thus, at very low temperatures ($\sim$4.2 K) generation of second sound—wave oscillations of the temperature—is possible in ultrapure dielectrics.[1–3]

This phenomenon is based on the ''freezing'' of Umklapp processes and conservation of the phonon quasimomentum as well as the large (of order the sample length) phonon mean-free path length. At low temperatures under the conditions of relatively high thermal pumping nonlinear (soliton) propagation of heat pulses, where dispersion (which cause phonon packets to spread) and nonlinear effects (which cause self-localization of packets) compensate one another, is also possible. Such nonlinear pulses have been observed in, e.g., pure NaF at temperatures from 1.4 to 4.2 K along directions of high symmetry [100].[2] Characteristically, the temperature in the pulses assumed only values from a definite range that depends on the temperature of the crystal. Thus, at crystal temperature 2 K the temperature in the pulses was in the range 5–10 K.

In the present letter we report the results of a computer simulation indicating the possibility of ballistic heat propagation in solids even at quite high (Debye) temperatures, where the phonon mean-free path length is short and equals only a few phonon wavelengths.

Three-dimensional Al and Ni crystallites containing about 8000 atoms have been investigated by molecular dynamics methods.[4,5] Rapid local heating was simulated by prescribing a temperature for the surface of the crystal that is much higher than the average temperature in the sample. Rigid boundary conditions were used in the direction of propagation of the thermal perturbation (perpendicular to the surface) and periodic boundary conditions were used in the other two directions. The interatomic interaction of the experimental crystallites was described by means of a multiparticle potential based on a model electron density functional.[6,7]

For ''instantaneous heating'' of a chosen region, starting at temperature 50 K and above, soliton-like pulses characterized by a stable shape and amplitude are formed in the Ni and Al crystallites. Just like ordinary solitons,[8] they remain essentially unchanged in shape as they move through the sample and are restored after interacting with one another.

The character of the propagation of the perturbation produced by local heating of a free (110) Al surface to 8000 K is shown in Fig. 1. One can see that a heat front, ahead of which soliton-like pulses move with a higher velocity, propagates away from the free surface (which corresponds to the origin of the coordinates). The first pulse, which has the largest amplitude, propagates with a higher velocity (8200 m/s) than pulses with a smaller amplitude. Our estimates of the propagation velocity of the heat front agree in order of magnitude with the theoretical calculations.[9]

Increasing the temperature of local heating increases the amplitude and propagation velocity of a pulse. Analysis of the distributions of the directions of the atomic velocities of such pulses shows that there are always regions of either compression or tension.

The effects due to rapid, strong local heating ($\sim$10000) of the surface are produced, for example, by irradiating a material with high-energy charged-particle beams,[10,11] used to alter the properties of a material in the direction required for applications. Thus, in Ref. 10 a bipolar wave (consisting of a wave of compression and tension), produced by rapid heating of a very thin surface layer by low-energy high-current electron beams, was observed, similarly to the manner in which in our calculations the structure of solitary pulses largely depended on the conditions of energy pumping and in Ref. 10 the profile of a bipolar wave was largely determined by the irradiation regime.

Bearing in mind that solitary pulses with similar characteristics are produced with mechanical loading and with local heating, we investigated the effect of the temperature of a crystal on the propagation of pulses induced by high-speed compression at sample temperatures 0, 100, and 300 K (Fig. 2) (specifically, a Ni crystallite was calculated). It was found that the temperature of the sample has virtually no effect on the propagation velocity of soliton-like pulses, but it has quite a strong effect on the shape of the pulse. Specifically, fluctuations of the crest of the soliton-like pulses arise at nonzero temperatures, and the pulse itself becomes wider (Figs. 2b and c). For example, at 300 K the width of the pulse at half-height is approximately two times greater than at 0 K.

In summary, even at temperatures of the order of the

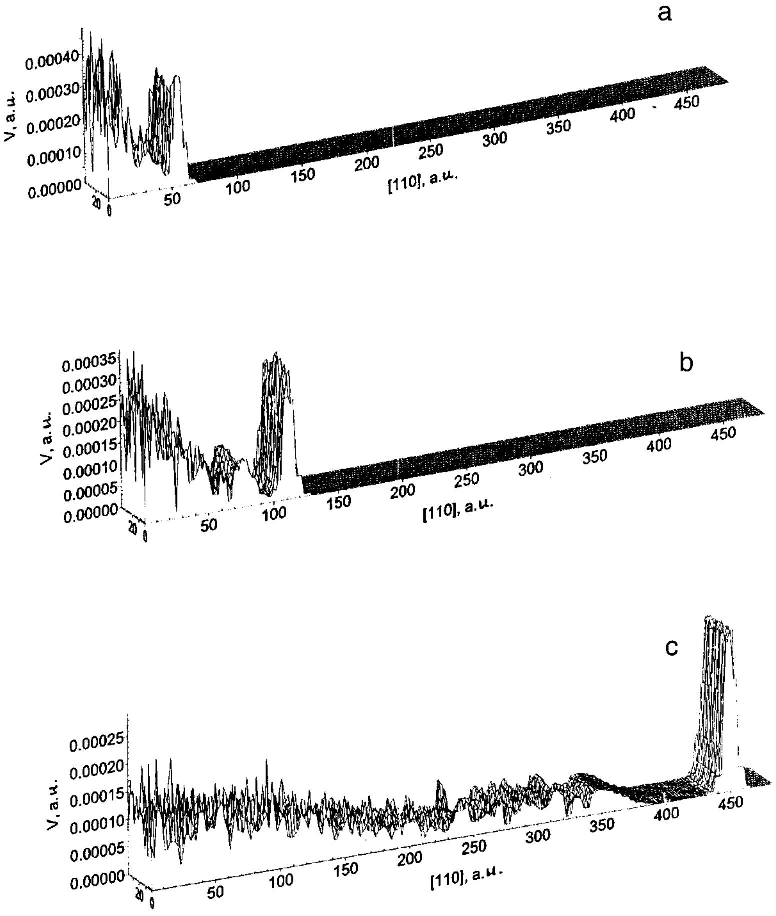

FIG. 1. Positions of a soliton-like pulse initiated by heating of the free surface of aluminum, at various times.

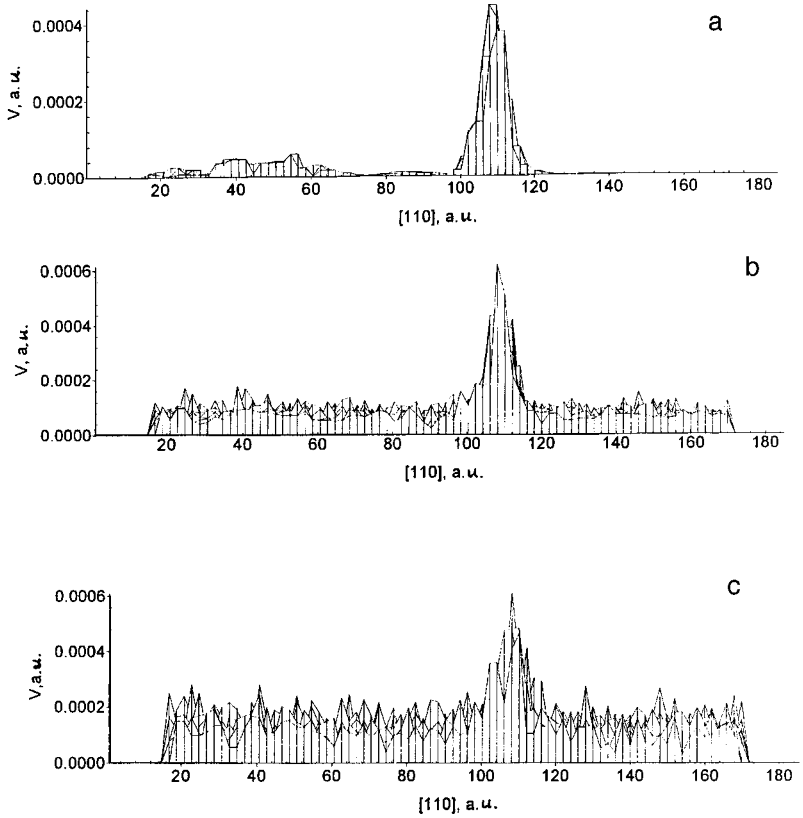

FIG. 2. Changes in the shape of a soliton-like pulse in Ni for various sample temperatures: a — $T=0$ K; b — $T=100$ K; c — $T=300$ K.

Debye temperature heat can be transferred in crystals in a ballistic regime (the Debye temperature in Ni, for example, is close to 300 K). The heat carriers are soliton-like pulses that do not decay appreciably.

It should be noted that although we simulated metals the results of this work are most applicable to insulators, where the phonon mechanism of heat conduction dominates.

[1] N. Ashcroft and D. Mermin, *Solid State Physics* (Holt, Rinehart, and Winston, New York, 1976; Russian translation, Mir, Moscow, 1972, Vol. 2).
[2] V. Narayanamurti and C. M. Varma, Phys. Rev. Lett. **25**, 1105 (1970).
[3] F. D. Tappert and C. M. Varma, Phys. Rev. Lett. **25**, 1108 (1970).
[4] S. G. Psakh'e, K. P. Zol'nikov, and D. Yu. Saraev, Pis'ma Zh. Tekh. Fiz. **24**(3), 42 (1998) [Tech. Phys. Lett. **24**, 99 (1998)].
[5] S. G. Psakh'e, K. P. Zol'nikov, and D. Yu. Saraev, Fiz. Goreniya Vzryva **33**(2), 43 (1997).
[6] V. M. Kuznetsov, G. E. Rudenskii, R. I. Kadyrov, and P. P. Kaminskii, J. Mater. Sci. Technol. **14**, 429 (1998).
[7] V. M. Kuznetsov, R. I. Kadyrov, and G. E. Rudenskii, J. Mater. Sci. Technol. **14**, 320 (1998).
[8] S. G. Psakh'e, K. P. Zol'nikov, and S. Yu. Korostelev, Pis'ma Zh. Tekh. Fiz. **21**(13), 1 (1995) [Tech. Phys. Lett. **21**, 489 (1995)].
[9] S. L. Sobolev, Usp. Fiz. Nauk **167**, 1095 (1997).
[10] S. V. Lykov, V. I. Itin, G. A. Mesyats, D. I. Proskurovskiĭ, and V. P. Rotshteĭn, Dokl. Akad. Nauk SSSR **310**, 858 (1990) [Sov. Phys. Dokl. **35**, 154 (1990)].
[11] V. I. Itin, I. S. Kashinskaya, S. V. Lykov, G. E. Ozur, D. I. Proskurovskiĭ, and V. P. Rotshteĭn, Pis'ma Zh. Tekh. Fiz. **17**(5), 89 (1991) [Sov. Tech. Phys. Lett. **17**, 192 (1991)].

Translated by M. E. Alferieff

Field-ion microscopy of deformation effects near the surface in ion-implanted metals (Ir)

B. A. Ivchenko and N. N. Syutkin

Institute of Electrophysics, Ural Branch of the Russian Academy of Sciences, Ekaterinburg

(Submitted November 2, 1998)
Pis'ma Zh. Tekh. Fiz. **25**, 60–64 (March 26, 1999)

Field-ion microscopy is used to determine the deformation due to ion implantation ($E=20$ keV, $D=10^{18}$ ions/cm^2, $j=300\ \mu$A/cm^2) near the surface in pure iridium. The effect is manifested as a high density of various types of defects in the near-surface volume (~50 nm from the irradiated surface) of the material. © *1999 American Institute of Physics.* [S1063-7850(99)02703-2]

It is well-known that irradiation alters the structural state of a material, specifically, in part because defects of various types form: radiation-disordered zones; dislocation configurations, dislocation loops and barriers, as well as complexes of these defects localized in small volumes; segregations of atoms of one component (for solid solutions), etc.

In Ref. 1 field-ion microscopy (FIM) was used to observe such defects and study their atomic structure in the near-surface volume of Cu_3Au which had undergone a structural phase transformation. It is of interest to study experimentally radiation defects in materials from the standpoint of strain hardening when radiation-stimulated phase transformations do not occur in the materials and a high density of implanted defects can produce a large change in the structural state and properties.

The aim of the present work was to observe radiation defects on an atomic level, to study the structural state of pure iridium after irradiation with argon ions, and to make a comparison with the morphology of the structural defects arising in pure iridium as a result of mechanical deformation.

Field-ion microscopy was used to study the changes in the structural state of ion-implanted Ir and to determine the character and distribution of the defects formed in the near-surface volume of the material. The method is capable of investigating the structural alterations of the crystal lattice of metals and alloys accurately with atomic-scale resolution, working with atomically pure surface at cryogenic temperatures, and at the same time analyzing the structure of the object through controlled removal of successive surface layers by an electric field.

The samples were implanted with 20–24 keV argon ions. The irradiation dose was 10^{18} ions/cm^2 and the current density was $j=300\ \mu$A/cm^2. Before irradiation the iridium precertified in a field-ion microscope had an atomically smooth surface prepared *in situ* by field evaporation of surface atoms. Ion images of the certified field emitters showed a perfect ring pattern of single crystals (Fig. 1a), essentially attesting to the absence of structural defects. The implanted samples were placed once again into the field-ion microscope and the state of the material in a volume near the surface was analyzed by recording with a VCR or a photographic camera the field-ion images of the surface through controlled removal of successive atomic layers.

As a result, a high density of point, linear, and three-dimensional structural defects was observed in the implanted pure iridium. A comparative analysis of the defects observed in mechanically predeformed iridium (~90%; Fig. 1b) and irradiated iridium (Fig. 2) showed a large difference between their structures.

After mechanical deformation it was established that boundaries of 20–30 nm grains form in the Ir volume (Fig. 1b). But virtually no structural defects are observed in the

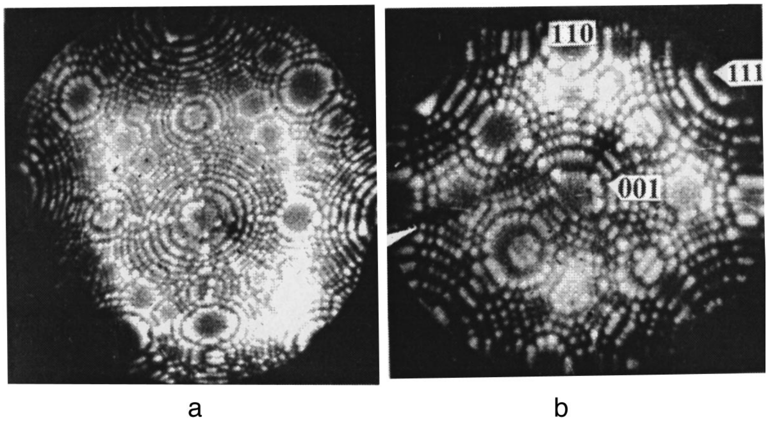

FIG. 1. Neon images of the surface: a — pure Ir single crystal ($V=10$ kV); b — pure Ir ($V=10$ kV) after ~90% deformation (the arrows indicate the grain boundaries).

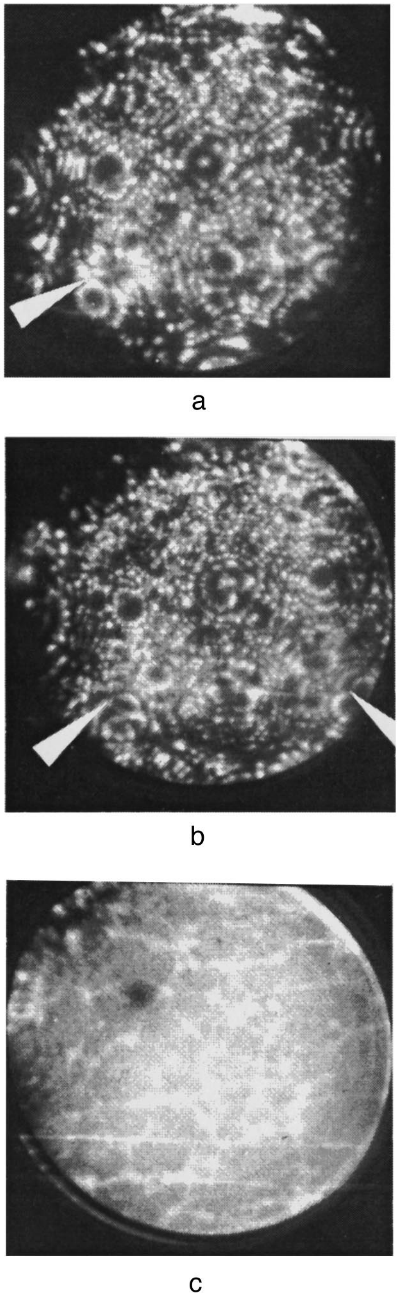

FIG. 2. Neon images of the surface of pure Ir after implantation with argon ions ($E=20$ keV, $D=10^{18}$ ions/cm^2, $j=300$ μA/cm^2): a — $V=7.2$ kV (a micropore is indicated); b — $V=8.4$ kV (the arrows indicate the defects of the crystal structure); c — $V=8.9$ kV.

body of the grains. Conversely, a subblock microstructure ($\sim 3-5$ nm) was observed in the irradiated metal (Fig. 2a–c). The disorientation of the blocks is 0.5–1 deg. In addition, various structural defects (Fig. 2) (marked by arrows) up to micropores (Fig. 2a) are observed in the body of the blocks.

The ion contrast of the subblock structure was revealed by increasing the voltage on the sample by a small amount (the difference relative to the voltage of the best image was about 500 V), but field evaporation of surface atoms still did not occur. The contrast of the boundaries themselves could be easily seen in the form of brighter lines bounding the blocks of the structure (Fig. 2c). In addition, it is obvious that there is a complete correspondence between the discontinuity of the ring-shaped pattern in Fig. 2b and the contrast of the block boundaries of the substructure in Fig. 2c (photomicrographs of the same Ir surface are presented in Figs. 2b and c, but the photomicrograph in Fig. 2c was obtained by increasing the voltage on the sample by 500 V). Note that the discontinuity in the ring-shaped pattern of the ionic contrast shows a disruption of the perfect structure of the crystal and determines the contrast from particular defects arising in the material after external perturbations.

Analysis of the near-surface volume of the Ar-ion-implanted Ir in the process of subsequent controlled removal of surface atoms showed that such a microstructure remains at distances up to 50 nm from the irradiated surface. It is known[2] that the projective range of the argon ions in metals, specifically, iridium, is less than 10 nm for the implantation conditions employed. Hence it can be inferred that the observed deformation effects are most likely due to impact effect of the ion beam, propagation of elastic waves into the material, and interaction of the elastic waves with lattice defects arising in the course of irradiation and with the embedded argon ions. In our view, the high implantation current density plays a significant role in the formation of the defects.

In summary, in this work the formation of an ultradispersed block structure in the surface and near-surface volumes of a pure metal (iridium) as a result of implantation of argon ions ($E=20$ keV, $D=10^{18}$ ions/cm^2, $j=300\mu$A/cm^2) was observed experimentally at distances an order of magnitude greater than the projective range of the particles from the irradiated surface. Such an irradiation-induced deformation effect is virtually impossible to obtain by mechanical action on the pure metal (Ir).

This work was supported by the Russian Fund for Fundamental Research (Project No. 98-02-17304).

We thank Professor V. V. Ovchinnikov for assisting in the experiment.

[1] V. A. Ivchenko and N. N. Syutkin, Appl. Surf. Sci. **87/88**, 257 (1995).

[2] A. F. Burenkov, F. F. Komarov, M. A. Kumakhov, and M. M. Temkin, *Spatial Distributions of the Energy Released in a Cascade of Atomic Collisions in Solids* (Énergoatomizdat, Moscow, 1985).

Translated by M. E. Alferieff

TECHNICAL PHYSICS LETTERS VOLUME 25, NUMBER 3 MARCH 1999

Optoelectronic neural system for processing the output data from a fiber-optic measuring network

Yu. N. Kul'chin, I. V. Denisov, and O. T. Kamenev

Far-East State Technical University, Vladivostok

(Submitted November 20, 1998)
Pis'ma Zh. Tekh. Fiz. **25**, 65–70 (March 26, 1999)

The results of an investigation of an optoelectronic neural system for processing the output data from a distributed fiber-optic tomographic-type measuring network are reported. The processing system is based on the operation principle of an optical perceptron in which the interneuron coupling matrix is implemented using a collection of amplitude holograms recorded on a disk-shaped holographic carrier. It is shown experimentally that this system makes it possible to reconstruct to within 20% the spatial distribution functions of the physical quantity under investigation. © *1999 American Institute of Physics.* [S1063-7850(99)02803-7]

To investigate natural and artificial physical objects and fields distributed over a certain area it is necessary to use information-measuring systems (IMSs) in which data acquisition is accomplished using distributed fiber-optic tomographic-type measuring networks. As shown in Ref. 1, the principles of neural network information processing make it possible to solve unambiguously the problem of reconstructing the tomographic data. Perceptron-type neural computer can be implemented best using optical components. This enables data processing in real time. Such a computer can be based on a holographic disk used as the optical coupling matrix of the neural network. This will increase the speed of operation substantially.

Several optical digital neural systems employing a holographic disk are now known.[2,3] However, for processing the output data from fiber-optic measuring networks it is more convenient to use analog neural systems, which will greatly increase the speed of operation and decrease the error.

For this reason, our objective in the present work was to develop and investigate an optoelectronic neural system for processing the output data from a fiber-optic measuring network.

The neural system under consideration processes the output signals from a measuring network used for reconstructing the distribution of the the external action under study over the region of interest. A collection of fiber-optic

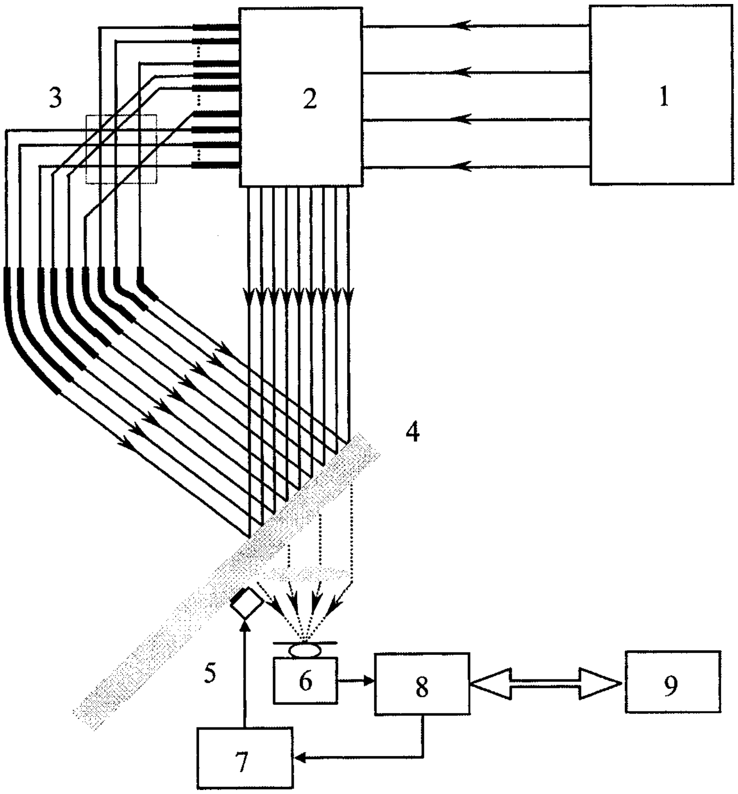

FIG. 1. Diagram of the experimental layout of an optoelectronic neural system for processing the output data from a fiber-optic measuring network: *1* — Optical radiation sources, *2* — beam splitter, *3* — fiber-optic measuring network, *4* — holographic disk, *5* — stepping motor, *6* — photodetector, *7* — controller, *8* — analog-to-digital converter (ADC), *9* — personal computer (PC).

measuring lines (FOMLs), packed in a square region as shown in Fig. 1, is used as the fiber-optic measuring network. A node (intersection of three FOMLs) that detects the effect of gravity on an object secured at the node is present at the center of each section. The measuring lines are based on a single-fiber two-mode interferometer, in which the radiation intensity at the exit of each FOML is proportional to the sum of the external actions detected by the same nodes through which it passes.[4]

The matrix elements of the interneuron connections of an optical perceptron are calculated using a computer model of the perceptron. The values obtained for the coupling matrix elements w_{ij} are used to determine the diffraction efficiency η_{ij} of the holographic diffraction gratings that are recorded on a disk-shaped carrier in the form of amplitude holograms of the optical perceptron:

$$\eta_{ij}=\frac{w_{ij}}{I_{0i}\Delta}I_0, \quad (i=1,\dots,N;\ \ j=1,\dots,M),$$

where I_{0i} is the intensity of the laser radiation at the exit of the i-th measuring line when recording holograms; I_0 is the intensity of the reference radiation when exposing the photomaterials; Δ is a constant that is determined by the value of the maximum diffraction efficiency of the holograms.

Figure 1 shows the layout of our optoelectronic neural processing system, which is based on an off-axis holographic scheme. To study the distribution of the physical quantity of interest, the radiation from each exit of the fiber-optic measuring network propagates successively onto a collection of holographic gratings belonging to each node of the measuring network. This produces an array of output data of the optical perceptron. This array characterizes the distribution of the physical quantity under study. After detection by a photodetector, these data pass through an ADC into a PC, where they are adjusted according to the expression

$$z_k=\sigma\psi\left(\sum_{i=1}^{N} I_{ij}^{d}-\sum_{i=1}^{N} w_{ij}b_i\right),$$

where k labels the node in the measuring network; N is the number of measuring lines; I_{ij}^{d} is the intensity of the radiation diffracted by the holographic grating with the corresponding diffraction efficiency η_{ij}; ψ is the transfer function of the photodetector and ADC amplifier; and b_i is a free term in the linear transfer functions of all nodes along the ith measuring line. The correction factor σ determines the degree of mismatch between the intensities I_{0i} at the exits of the measuring lines at the hologram-recording stage and the intensities I'_{0i} at their exits immediately before the measurements and is calculated according to the formula

$$\sigma=\frac{1}{N}\sum_{i=1}^{N}\frac{I_{0i}}{I'_{0i}}.$$

Figure 2 shows the result of the experimental reconstruction of the reference deformation action of the gravitational field at three nodes of a 16×16 measuring network divided into 256 elementary sections. The accuracy of the reconstruction depends on the spatial frequency of the measuring network. The experimental results showed that the relative error introduced by the optical perceptron is determined by the quality of the training of its model and was 6% in our experiment. At the same time, the instability of the radiation sources and the temperature drift of the working points of the FOMLs increase the error to 20%.

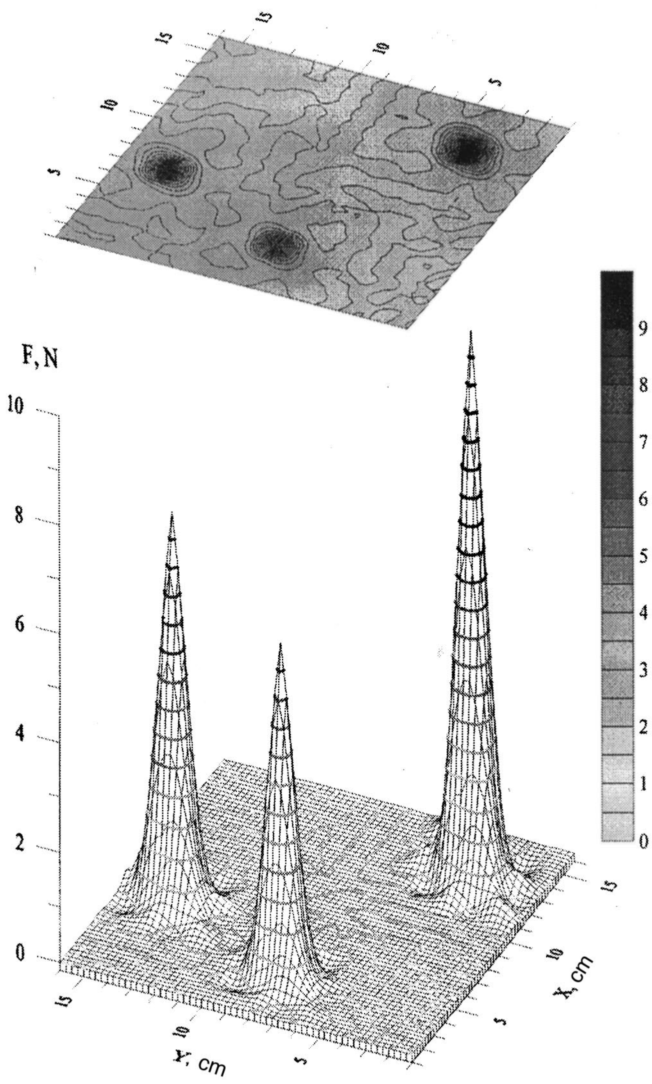

FIG. 2. Result of the reconstruction of the deformation action of gravity at three nodes of the measuring network by an optoelectronic neural processing system.

In summary, in the present letter an optoelectronic neural system for processing the output data from a fiber-optic tomographic measuring network was presented. This system makes it possible to perform parallel processing of optical information for the purpose of reconstructing the spatial distribution function of a physical quantity of interest.

[1] Yu. N. Kulchin, O. T. Kamenev, and I. V. Denisov *et al.*, Opt. Mem. Neural Netw. **6**, 149 (1997).

[2] A. Kutanov, B. Abdrisaev, and S. Dordoev, Opt. Lett. **17**, 952 (1992).

[3] A. L. Mikaelian, E. H. Gulanyan, and B. S. Kretov *et al.*, Opt. Mem. Neural Netw. **1**, 7 (1992).

[4] Yu. N. Kul'chin, O. B. Vitrik, O. V. Kirichenko *et al.*, Avtometriya, No. 5, 32 (1995).

Translated by M. E. Alferieff

TECHNICAL PHYSICS LETTERS VOLUME 25, NUMBER 3 MARCH 1999

Thermomechanical effect in a cylindrically-hybrid nematic liquid crystal

R. S. Akopyan, R. B. Alaverdyan, É. A. Santrosyan, S. Ts. Nersisyan,
and Yu. S. Chilingaryan

Erevan State University

(Submitted June 5, 1998)
Pis'ma Zh. Tekh. Fiz. **25**, 71–73 (March 26, 1999)

Thermomechanical rotation of a cylindrically-hybrid nematic liquid crystal in the presence of a longitudinal temperature gradient is predicted theoretically and detected experimentally. © *1999 American Institute of Physics.* [S1063-7850(99)02903-1]

1. A systematic theory of thermomechanical effects in deformed liquid crystals (LCs) were first constructed in Ref. 1. Subsequently, the experimental observation of the rotation of matter in the horizontal plane of nematic layers in the field of a longitudinal temperature gradient was reported in Ref. 2. A thermomechanical effect in a homeotropically planar-oriented nematic liquid crystal (NLC) was first detected experimentally in Ref. 3. In this effect a hydrodynamic flow appears as a result of a longitudinal temperature gradient. The values of the thermomechanical coefficient measured in Refs. 2 and 3 are in good agreement with the theoretical estimate.

In the present work a thermomechanical rotation of a cylindrically and axially-hybrid-oriented NLC as a result of a longitudinal temperature gradient is predicted theoretically and detected experimentally.

2. Let us consider a cylindrical horizontal NLC cell on whose bottom substrate $(z=0)$ a homeotropic boundary condition is prescribed. On the top substrate $(z=L)$ planar boundary condition is prescribed such that in this plane the molecules would be oriented everywhere along concentric circles centered on the axis of a cylinder (see Fig. 1). Let the (x,y) plane be the bottom base of the cylinder. Then in the single-constant approximation the Frank elastic constants are $K_1=K_2=K_3=K$. The director distribution will have the form

$$n_x=\sin\varphi\sin\frac{\pi z}{2L},\quad n_y=\cos\varphi\sin\frac{\pi z}{2L},\quad n_z=\cos\frac{\pi z}{2L}. \tag{1}$$

Here φ is the azimuthal angle of the cylindrical coordinate system and L is the cell thickness. Let external heat sources maintain a temperature $T=T_0=\Delta T$ in the $z=0$ section and a temperature $T=T_0$ in the $z=L$ section. Then the expression for the thermomechanical viscous force can be written in the very simple form $\xi(\Delta T/L^3)$. Here ξ is the thermomechanical constant. We shall write the stationary

Navier–Stokes equation in a cylindrical coordinate system, assuming uniformity with respect to φ and r, as

$$\eta\frac{\partial^2\nu_\varphi}{\partial z^2}-\eta\frac{\nu_\varphi}{r^2}=\xi\frac{\Delta T}{L^3}. \tag{2}$$

Here η is the viscosity of the NLC. The solution of the equation with the boundary conditions $\nu_\varphi(z=0,L)=0$ is

$$\nu_\varphi=\frac{\xi}{\eta}r^2\frac{\Delta T}{L^3}\times\left\{\frac{\left(\exp\left(-\frac{L}{r}\right)-1\right)\exp\left(\frac{z}{r}\right)+\left(1-\exp\left(\frac{L}{r}\right)\right)\exp\left(-\frac{z}{r}\right)}{\left(\exp\left(-\frac{L}{r}\right)-\exp\left(\frac{L}{r}\right)\right)-1}\right\}. \tag{3}$$

Far from the cylindrical axis $r\gg L$ and $r\gg z$ we have

$$\nu_\varphi=\frac{\xi}{2\eta}\frac{\Delta T}{L^3}z(z-L)\quad\text{and}\quad\nu_{\varphi\,\max}=\frac{\xi}{8\eta}\frac{\Delta T}{L}. \tag{4}$$

Thus, the velocity of rotation around the cylindrical axis does not depend on the distance from the axis.

3. A cylindrical axially-hybrid cell of the NLC MBBA with the nematic phase interval 20–47 °C was used in the experiment. A sandwich-type cell was arranged in a strictly horizontal plane and heated below by a continuous transparent heater, which gave uniform heating in the horizontal plane to within ±0.01 °C and made it possible to observe textures in a polarizing microscope.

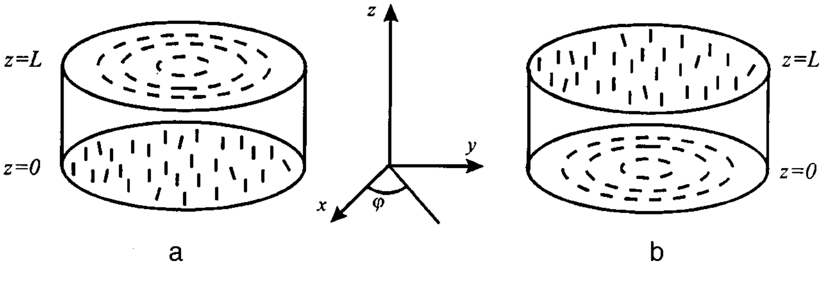

FIG. 1. Geometry of the experiment. The substrate of the cell that sets the planar orientation of the NLC is located a — at the top and b — at the bottom.

The temperature difference between the bottom and top surfaces of the film was determined as the difference of the transition temperatures into the isotropic phase in the bottom and top layers. The velocity $\nu_{\varphi\,\max}$ was determined as the maximum velocity of small (2–3 μm) particles of aluminum oxide.

The geometry of the experiment is displayed in Figs. 1a and b. The dashed lines show the distribution of the director on the coaxial cylinders $r=\text{const}$. In the experiment, when the substrate of the cell that sets the planar orientation of the NLC was located on top (case a), rotation of the liquid crystal around the cylindrical axis z was observed. The maximum flow velocity for a cell with thickness $L=100\ \mu$m and temperature difference between the top and bottom surfaces $\Delta T=5$ °C was on the order of $\nu_{\varphi\,\max}\approx 0.5\ \mu$m/s. In the case *b*, where the substrate setting the planar orientation of the NLC molecules is located at the bottom, an oscillatory rotation around the axis of the cylindrical cell arises in the system.

[1] R. S. Akopyan and B. Ya. Zel'dovich, Zh. Éksp. Teor. Fiz. **87**, 1660 (1984) [Sov. Phys. JETP **60**, 953 (1984)].

[2] O. D. Lavrentovich and Yu. A. Nastishin, Ukr. Fiz. Zh. **32**(6), 710 (1987).

[3] R. S. Akopyan, R. B. Alaverdyan, É. A. Santrosyan *et al.*, Pis'ma Zh. Tekh. Fiz. **23**(17), 77 (1997) [Tech. Phys. Lett. **23**, 690 (1997)].

Translated by M. E. Alferieff

TECHNICAL PHYSICS LETTERS VOLUME 25, NUMBER 3 MARCH 1999

Effect of elastic stresses on free oscillations in ferroelectric liquid crystals

M. N. Pivnenko, A. P. Fedoryako, L. A. Kutulya, and V. P. Seminozhenko

Institute of Single Crystals, Ukrainian National Academy of Sciences, Khar'kov

(Submitted April 3, 1998)
Pis'ma Zh. Tekh. Fiz. **25**, 74–80 (March 26, 1999)

It is shown experimentally that an elastic mechanical stress in a crystal structure is a necessary factor for the appearance of free oscillations of the director of a ferroelectric liquid crystal. Such a mechanical stress arises as a result of internal textural perturbations in the presence of regions with a different orientation of the director or is produced by external pressure applied to one of the cell plates in the appropriate direction. © *1999 American Institute of Physics.* [S1063-7850(99)03003-7]

The effect of an ac electric field on a ferroelectric liquid crystal (FLC) is to produce, as a result of the electroclinic effect and backflow, vertical and horizontal mechanical vibrations of the cell plates at the frequency or harmonics of the applied electric field.[1] Damped mechanical oscillations of the cell plates appear when an FLC is excited near an SmA–SmC* phase transition by square electric pulses. The frequency of these oscillations is determined by the mechanical resonances of the cell and the components securing the cell.[2] We have shown that these mechanical oscillations of the cell plates are accompanied by oscillations of the electric current, which are synchronous with the oscillations of the plates, in the external circuit containing the cell holding the FLC[3,4] and by oscillations of the optical density of a cell placed between crossed polaroids.[5] These processes indicate the appearance of free damped oscillations of the director of the FLC after an abrupt change in the electric field intensity.

Since the methods of classical Fourier spectral analysis do not permit investigating time-dependent processes such as damped oscillations in an FLC correctly (see, for example, Ref. 6), we used[3–5] the instantaneous spectrum method.[6,7] As a result, it was found that there exist two types of damped oscillations of the director of an FLC, the most important distinction between which is that near the SmA–SmC* second-order phase transition the frequency of oscillations of the first type depends strongly on the temperature of the FLC. This fact indicates the existence of resonances of the texture of the FLC in the frequency range 1–20 Hz.

Further investigations revealed that elastic mechanical stresses in the crystal structure play the main role in producing oscillations of the director of an FLC.

The experiment was performed on a eutectic mixture (51.5 and 48.5 wt.%) of the complex esters of 4-*n*-hexyloxyphenyl-4-*n*-octyloxybenzoate and 4-*n*-hexyloxyphenyl-4-*n*-decyloxybenzoate. Bis-4,4″ $(2S-2$-chlorohexyl)-terphenyldicarboxylate[8] in the amount 9.85 wt.% was used as a chiral additive inducing the ferroelectric properties. This composition possesses a SmA–SmC* second-order phase transition at 65 °C. The spontaneous polarization at 30 °C was 22.5 ns/cm^2.

The measuring cell consisted of two $27\times15\times1$ mm glass plates separated by 15 μm thick fluoroplastic spacers. The cell is assembled so that the FLC-filled volume is $15\times15\times0.015$ mm^2. The cell was secured in a manner so as to permit small motions of the top glass plate. The inner side of the glass cell plates was coated with a transparent current-conducting coating, to which a 100-Hz square electric voltage pulse was applied. The maximum electric field strength was $3.3\cdot10^4$ V/cm.

The oscillations were investigated in a uniform bookshelf texture, which was constructed, using the well-known method,[4,9] from a homeotropic texture in an electric field at temperature 63–64 °C [onset of SmC* using mechanical vibrations of the top glass plate in the direction of the X axis (Fig. 1)]. The smectic layers lie in the XZ plane, and the FLC molecules lie in the direction of the Y axis. To produce a controllable mechanical stress in the texture, pressure was applied to the top glass cell plate in the direction of the Y axis, i.e., in the plane of the glass cell plates and perpendicular to the smectic layers (the maximum pressure was 10^4 dynes/cm^2, normalization to the area of the cell occupied by the bookshelf texture).

Two measuring cells **A** and **B** were used. The cell **B** was distinguished only in that the current-conducting coating covered a 5×5 mm^2 area at the center rather than the entire glass plate. Thus, the FLC is in an electric field only within this area and a uniform bookshelf texture was constructed only on this area. Everywhere else on the area of the cell the texture remained homeotropic. The cell temperature was stabilized and measured to within ±0.02 °C.

Figure 2 shows the parameters of the oscillations as a function of pressure: the initial amplitude A_0, the frequency f, and the damping rate α at FLC temperature 61.8 °C, which corresponds to the SmC* phase. As pressure increases, the amplitude of the oscillations increases nonlinearly. As a result of the application of pressure, the initial amplitude can be increased by a maximum of almost one order of magnitude. At pressures above 4500 dynes/cm^2 the top glass cell plate shifts. This is caused by breaking of the bond between the FLC molecules and the substrate surface and destroys the uniform bookshelf texture. The amplitude of the oscillations drops sharply.

The frequency of the oscillations also increases nonlinearly with pressure. The maximum attainable frequency is

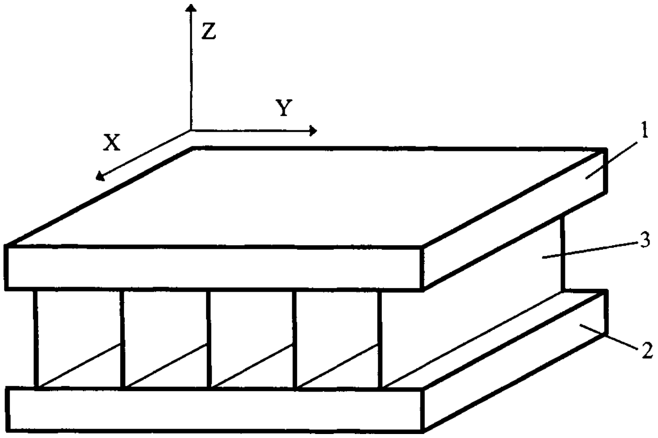

FIG. 1. Geometry of the experiment: 1 — Mobile substrate, 2 — stationary substrate, 3 — smectic layers.

approximately 1.3 times higher than the frequency of the oscillations without pressure. The damping rate α does not change much. A shallow minimum is reached at a pressure of about 2000 dynes/cm^2, after which α increases. The overall change in α was less than $\pm 15\%$ of its value in the absence of pressure.

Similar behavior is also observed at other temperatures in both the SmC* and SmA phases. The change produced in the parameters of the oscillations by the applied pressure is reversible, if the FLC texture has not been destroyed.

It is evident from Fig. 2 that the elastic mechanical stress arising in the texture of the FLC as a result of the applied pressure greatly increases the amplitude of the oscillations. Oscillations with an initial amplitude of about 120 mV, which are observed with zero external pressure, also arise as a result of a mechanical stress in the texture. This stress is caused by the existence of regions with different orientations of the director. If the mechanical stress in the FLC texture is canceled out by adjusting the magnitude and direction of the external pressure, then the oscillations completely vanish.

An experiment investigating the interaction of regions in an FLC with different orientation of the director was performed in cell **B** where a portion of the area was occupied by uniform bookshelf texture and a portion was occupied by homeotropic texture. Figure 3 shows the temperature dependence of the amplitude of the oscillations in the cell **B** (curve 2). This dependence was obtained as follows. At temperature 61.5 °C an external pressure of 4000 dynes/cm^2 was applied to the top glass cell plate and oscillations with an amplitude of about 400 mV were obtained. After the external pressure was removed, the amplitude of the oscillations decreased, but to 250 mV and not zero. We believe that this is due to the fact that the portion of the cell area occupied by the homeotropic texture prevented the top glass plate from returning to the equilibrium position. A mechanical stress of the homeotropic and bookshelf textures of the FLC, which are intercoupled with one another through the mobile glass cell plate, developed. As the temperature increased, the amplitude of the oscillations remained approximately constant in the range 61.5–65.0 °C, i.e., up to the phase transition. A unique regime of stabilization of the amplitude of the oscillations in which the amplitude increase caused by a temperature increase[3,4] was compensated by an amplitude decrease caused by a pressure decrease, was established. The pressure decreased, since it was produced by textural mechanical stresses, and it decreased as the elastic properties of the FLC became weaker with increasing temperature.

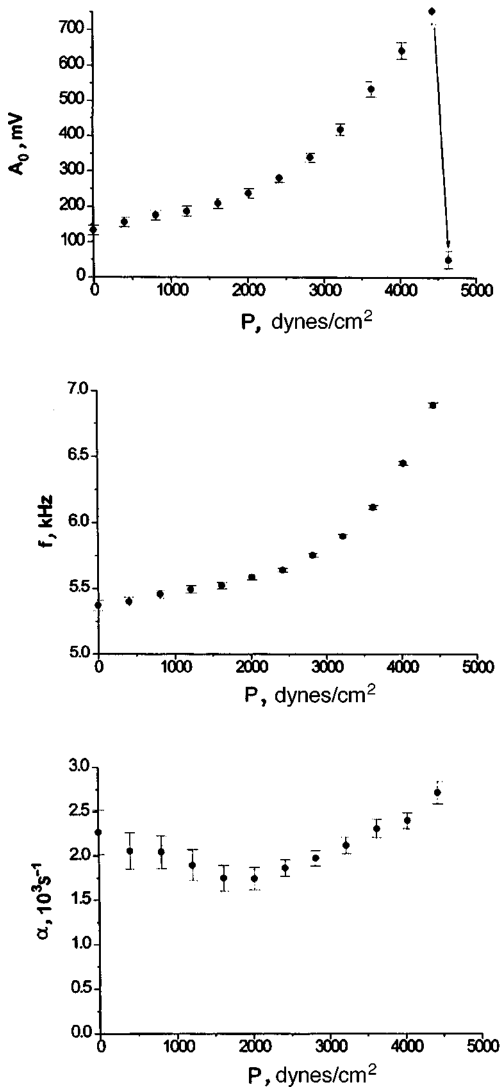

FIG. 2. Oscillation parameters versus the external pressure at temperature 61.80 °C.

After the phase transition in the SmA phase the mechanical stress decreased substantially and the amplitude of the oscillations dropped essentially to zero. Of course, on subsequent cooling, after the transition into SmC*, the mechanical stress and pressure did not recover on their own. For this reason the temperature dependence of the amplitude of the oscillations was found to be very narrow (curve 3 in Fig. 3). The width of the curve was no more than 1 °C, and the maximum was reached at the phase-transition temperature. Previously, such temperature dependences of the oscillations were investigated[3–5] in the absence of external pressure.

The temperature dependence of the initial amplitude of the oscillations with a constant external pressure of 3200 ± 40 dynes/cm^2 is shown in Fig. 3 (curve 1). Comparison of

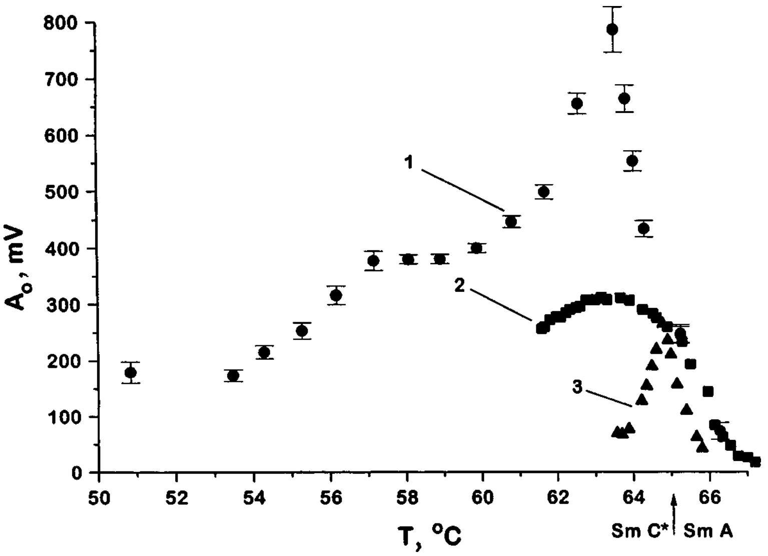

FIG. 3. Oscillation amplitude versus temperature: 1 — with constant external pressure 3230 ± 40 dynes/cm^2; 2, 3 — under a pressure produced by internal mechanical stresses.

the curves 1 and 3 (the amplitude of the oscillations with a constant external pressure and without pressure) shows that in the SmC* phase at a temperature more than 1 °C below the phase transition into SmA, the lateral pressure is the main factor responsible for the appearance of oscillations of the director of the FLC. Under a weak pressure produced only by the internal mechanical stresses, oscillations with a small amplitude are observed in a narrow temperature interval near the phase transition. The temperature dependence of the amplitude of the oscillations is symmetric with respect to the phase-transition temperature. A constant external pressure of order 10^3 dynes/cm^2 causes a large increase in the amplitude of the oscillations and expands the temperature range of the existence of oscillations in the direction of the SmC* phase by at least 15–20 °C. Conversely, the influence of the lateral pressure is negligible in the SmA phase.

It has been noted in investigations of the uniform bookshelf texture[4] that the weakening of the oscillations on cooling is accompanied by the appearance of disclinations which are characteristic for chevron textures. The application of a lateral pressure to the mobile cell plate causes these disclinations to vanish and restores the amplitude of the oscillations.

[1] A. Jákly and A. Saupe, Mol. Cryst. Liq. Cryst. **237**, 389 (1993).
[2] A. Jákly and A. Saupe, Mol. Cryst. Liq. Cryst. **263**, 103 (1995).
[3] A. P. Fedoryako, M. N. Pivnenko, E. V. Popova, and V. P. Seminozhenko, Pis'ma Zh. Tekh. Fiz. **23**(7), 80 (1997) [Tech. Phys. Lett. **23**, 287 (1997)].
[4] A. P. Fedoryako, M. N. Pivnenko, E. V. Popova, and V. P. Seminozhenko, Functional Materials **4**, 375 (1997).
[5] M. N. Pivnenko, A. P. Fedoryako, E. V. Popova, and L. A. Kutulya, *Nonlinear Optics of Liquid and Photorefractive Crystals*, Proc. SPIE (1998), in press.
[6] J. Max, *Methodes et Techniques de Traitment du Signal et Applications aux Mesures Physiques* (Masson, New York, 1981; Russian translation, Mir, Moscow, 1983].
[7] C. N. Page, J. Appl. Phys. **23**, 1 (1952).
[8] M. V. Loseva, E. P. Pozhidaev, A. Z. Rabinovich *et al.*, *Ferroelectric Liquid Crystals* (Itogi nauki i tekhniki, VINITI, Ser. Fizichesakaya khimiya, 1990).
[9] A. Jákly and A. Saupe, Appl. Phys. Lett. **60**, 2622 (1992).

Translated by M. E. Alferieff

TECHNICAL PHYSICS LETTERS VOLUME 25, NUMBER 3 MARCH 1999

Self-organization phenomena accompanying deformation–thermal instability during anodic etching of silicon in a HF solution

V. S. Kuznetsov and A. V. Prokaznikov

P. G. Demidov Yaroslavl' State University; Institute of Microelectronics, Russian Academy of Sciences

(Submitted September 14, 1998)
Pis'ma Zh. Tekh. Fiz. **25**, 81–88 (March 26, 1999)

A model of self-organization during anodic etching in the preparation of porous silicon is proposed. [S1063-7850(99)03103-1]

Interest in self-organization processes continues unabated. This is because such processes touch upon the fundamental properties of nature.[1] These phenomena encompass diverse fields of physics, chemistry, biology, and other disciplines of natural science. Nonlinear processes developing on solid surfaces accompanying local input of energy comprise a definite class of such phenomena. Laser-stimulated self-organization processes have been studied in Refs. 2–4. Self-organization processes caused by current filamentation during anodization of *n*-type silicon samples with a relatively low level of illumination of the silicon have been studied in Refs. 5 and 6. These processes are characterized by the formation of two types of concentric structures, ring-shaped and radial.

The physical mechanism leading to the appearance of ring structures consists in the following. The formation of current filaments in a near-surface space-charge region of silicon on account of generation–recombination instability with large voltage drops[7] is accompanied by the appearance of regions with a high carrier density and temperature[8] and, in consequence, by the occurrence of both a nonuniform (along the surface) lattice-temperature field and a thermoelastic force. The positive deformation and temperature feedback leads to instability, in which the amplitudes of the Fourier components of the temperature (conductivity) perturbations and static deformation grow exponentially in time. As a result, nonuniform etching occurs and concentric rings and radial structures are formed. Electric breakdown and formation of a current filament in this case play the role of the initial activation, and the instability itself is due to Joule heating, but the character of the structure formed depends very strongly on the initial conditions, i.e., on the characteristics of the current filament.

Let the silicon plate be in contact on one side with an electrolyte. We shall assume that the conductivity and thermal diffusivity of the electrolyte are higher than that of silicon. We shall neglect the Joule heating of the electrolyte. In the region of the semiconductor the equation of motion of the nonuniformly heated medium and the heat-conduction equation have the forms[9]

$$\frac{\partial^2 \mathbf{U}_t}{\partial t^2} - c_t^2 \nabla^2 \mathbf{U}_t = 0, \quad \boldsymbol{\nabla} \cdot \mathbf{U}_t = 0; \tag{1}$$

$$\frac{\partial^2 \mathbf{U}_t}{\partial t^2} - c_l^2 \nabla^2 \mathbf{U}_l + \frac{K\alpha}{\rho} \nabla T = 0, \quad \boldsymbol{\nabla} \times \mathbf{U}_l = 0; \tag{2}$$

$$\frac{\partial T}{\partial t} - \chi \nabla^2 T \frac{K\alpha T}{c_v} \frac{\partial}{\partial t} \boldsymbol{\nabla} \cdot \mathbf{U} \frac{\sigma_0 E^2}{c_v} \left\{ \exp\left(\frac{W}{k_b} \left[\frac{1}{T} - \frac{1}{T_p} \right] \right) - 1 \right\} = 0. \tag{3}$$

Here c_t and c_l are the velocity of transverse and longitudinal acoustic waves, χ is the thermal diffusivity, $K = \rho[c_l^2 - c_t^2/3]$ is the bulk modulus, ρ is the density of silicon, α is the volume thermal expansion coefficient, c_v is the specific heat per unit volume, W is the activation energy of electrical conductivity, T_0 is the electrolyte temperature, σ_0 is the conductivity, E is the electric-field intensity in the space-charge region near the surface, and k_b is Boltzmann's constant.

The boundary conditions for the temperature and deformation $\mathbf{V} = \mathbf{U}_l + \mathbf{U}_t$ in a cylindrical coordinate system (r, φ, z) have the form

$$T|_{r\to\infty} = T_0, \quad \left.\frac{\partial T}{\partial r}\right|_{r\to\infty} = 0, \quad \left.\frac{\partial T}{\partial z}\right|_{z=0} = \alpha'(T - T_0); \tag{4}$$

$$\mathbf{V}|_{r\to\infty} = 0, \quad U_z^{\text{liq}}|_{z=0} = 0 = V_z|_{z=0},$$

$$\sigma_{zz}^{\text{liq}}|_{z=0} = \sigma_{zz}|_{z=0}, \quad \sigma_{rz}^{\text{liq}}|_{z=0} = \sigma_{rz}|_{z=0}, \tag{5}$$

where $\alpha' = 1/(c_v \chi R)$ is the thermal diffusivity between the electrolyte and semiconductor, R is the thermal resistance, $\mathbf{U}^{\text{liq}}$ is the displacement vector of the liquid, and σ_{ij}^{liq} and σ_{ij} are, respectively, the strain tensor in the electrolyte and in the semiconductor. Let $z = 1$ be the interface between the electrolyte $(z < 0)$ and the semiconductor $(z \geqslant 0)$.

The system of equations (2) and (3) is nonlinear and has only one uniform stationary solution, $\mathbf{V} = 0$ and $T = T_0$, but nonuniform stationary states are possible.

For $|1 - W/(4kT_0)||T_1/T_0| \ll 1$ the system (2) and (3) can be linearized by expanding about the uniform stationary state

$$\ddot{\Phi} - C_l^2 \nabla^2 \Phi + \frac{K\alpha}{\rho} T_1 = 0,$$

$$\dot{T}_1 - \chi \nabla^2 T_1 - \frac{\sigma_0 E^2}{c_v} \frac{W}{k_b T_0^2} T_1 - \frac{K\alpha T_0}{c_v} \nabla^2 \dot{\Phi} = 0,$$

where $\mathbf{U}_l = \nabla \Phi$ and $T = T_0 + T_1$.

We shall seek the solution of this system in the form

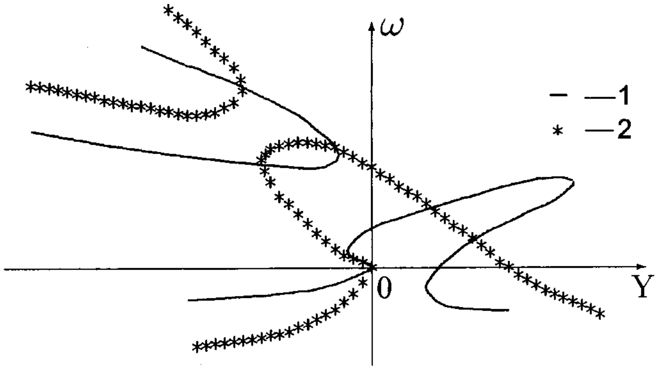

FIG. 1. Growth rate ω versus $k^2-q^2\equiv Y$ for weak electric fields $E^2<E_{\mathrm{cr}}^2(-)$ and for strong electric fields $E^2>E_{\mathrm{cr}}^2(*)$.

$$\Phi(z,r,t)=\sum_{q,\omega}\Phi_0(\omega,q,k)e^{ikz+\omega t}J_0(qr); \tag{6}$$

$$T_1(z,r,t)=\sum_{q,\omega}T_0'(\omega,q,k)e^{ikz+\omega t}J_0(qr), \tag{7}$$

where ω is the growth rate of the deviations from the initial state, k is the wave number, Φ_0 and T_0' are independent of the coordinates z and r and of the time t, and $J_n(x)$ is an nth order Bessel function of the first kind.

The condition of solvability with respect to Φ and T_0' leads to the equation

$$\left[\omega+\chi(k^2+q^2)-\frac{\sigma_0E^2}{c_v}\frac{W}{k_bT_0^2}\right][\omega^2+c_l^2(k^2+q^2)] = \frac{K^2\alpha^2T_0}{\rho c_v}\omega(k^2+q^2), \tag{8}$$

which is cubic in ω and quadratic in $k^2+q^2\equiv Y$, i.e., it gives two values Y_1 and Y_2 with a fixed value of ω. We shall take Y_1 to be the branch that corresponds to the lower value of Y for a given value of ω. At the point of the maximum both groups are equal, $Y_1=Y_2$. Figure 1 shows the Y dependence of the growth rate ω of the normal modes for $E^2<E_{\mathrm{cr}}^2=K^2\alpha^2k_bT_p^3/(\sigma_0\rho\chi W)$ and for $E^2>E_{\mathrm{cr}}^2$.

Hence it follows that to each fixed value of ω and q there correspond four values of k: $k_1=\sqrt{Y_1-q^2}, -k_1$, $k_2=\sqrt{Y_2-q^2}$, and $-k_2$. Therefore the solution in the general case can be written as a superposition of the four expressions (6) and (7) with $k=k_1$, $k=-k_1$, $k=k_2$, and $k=-k_2$.

Three regions can be distinguished in the figures presented: region I ($Y_2<q^2$), region II ($Y_1<q^2<Y_2$), and region III ($q^2<Y_1$). In the first region k_1 and k_2 are imaginary quantities, in the second region k_1 is imaginary and k_2 is real, and in the third region both k_1 and k_2 are real.

The solution of Eq. (1) can be written in the form

$$U_r=\sum_{q,\omega}\frac{1}{q}A_0(\omega,q)e^{-\lambda z+\omega t}J_1(qr), \tag{9}$$

$$U_z=\sum_{q,\omega}\frac{1}{\lambda}A_0(\omega_0,q)e^{-\lambda z+\omega t}J_0(qr), \tag{10}$$

where $\lambda=(q^2+\omega^2/c_t^2)^{1/2}$ and A_0 is a function of ω and q.

In the region of the electrolyte we are dealing only with longitudinal acoustic waves, for which the components of the displacement vector are

$$U_r^{\mathrm{liq}}=\sum_{q,\omega}B_0(\omega,q)e^{\lambda_1z+\omega t}J_1(qr), \tag{11}$$

$$U_z^{\mathrm{liq}}=\sum_{q,\omega}B_0(\omega,q)e^{\lambda_1z+\omega t}J_0(qr), \tag{12}$$

where $\lambda_1=(q^2+\omega^2/c_{ll}^2)^{1/2}$ and c_{ll} is the velocity of sound in the electrolyte.

It follows from the expressions obtained for λ and λ_1 that for real ω and q these quantities are also real and the equations (9)–(12) describe the formation of deformational perturbations near the surface.

The four boundary conditions (4) and (5) at $z=0$ give a system of four equations for determining, in the general case, the six coefficients A_0, $\Phi_0(\omega,q,k_1)$, $\Phi_0(\omega,q,-k_1)$, $\Phi_0(\omega,q,k_2)$, $\Phi_0(\omega,q,-k_2)$, and B_0.

In the region I in Fig. 1 the quantities k_1 and k_2 are purely imaginary, and taking account of the fact that the deformation into the semiconductor should not grow without bound, we must set $\Phi_0(\omega,q,-k_1)=0$ and $\Phi_0(\omega,q,-k_2)=0$. In this case we obtain a system of four homogeneous equations for determining the four unknowns. A solution exists only for certain values of $\alpha'<0$ and describes the processes in a thin layer near the surface with energy pumped into the semiconductor–electrolyte interface (illumination, ultrasonic irradiation, and formation of a thin layer with a high electrical resistance on the surface).

In region II in Fig. 1 k_1 is imaginary and k_2 is real. Therefore it is necessary to determine five unknowns: $A_0,\Phi_0(\omega,q,k_2)$, $\Phi_0(\omega,q,-k_2)$, and B_0 $(\Phi_0\times(\omega,q,-k_2)=0)$; ω and q are unrestricted, but strict conditions arise from the initial conditions.

In Fig. 1 for $E<E_{\mathrm{cr}}$ we can identify a narrow region III ($\omega_{\min}<\omega<\omega_{\max}$ and $q^2<Y_1$), where both k_1 and k_2 will be real. Here

$$\omega_{\min}=\frac{\sigma'E^2}{c_vT_0}\frac{W}{k_bT_0},$$

and $\omega_{\max}$ is determined from the condition that $Y_1=Y_2$ at the point of the maximum.

Since self-organization phenomena, expressed in the formation of ring-shaped structures, occur simultaneously with pore-formation processes, the electric-field intensity E must equal the electric-field intensity for the formation of strata. The value of this intensity is somewhat less than that of the electric field E_l for avalanche breakdown.[8] For $E=0$ and $E=E_{\mathrm{cr}}$ the third region vanishes ($\omega_{\max}=\omega_{\min}$). According to Ref. 10, for silicon $E_l\approx4\times10^5$ V/cm and for $c_c=1.63$ J/(cm$^3\cdot$K), $\chi=0.896$K cm^2/s, $\sigma_0^{-1}=4.5\,\Omega\cdot$ cm, $\alpha=7.8\times10^{-6}\,\mathrm{K}^{-1}$, $W=0.15$ eV, $c_l=9.10\times10^5$ cm/s, $c_t=5.84\times10^5$ cm/s, $\rho=2.328$ g/cm^3 we obtain $E_{\mathrm{cr}}=3.98\times10^5$ V/cm, which can be regarded as good agreement. Figure 2 shows the dependence of the maximum value of q and the growth rate $\omega_{\max}$ for the given region as a function of the electric field intensity E.

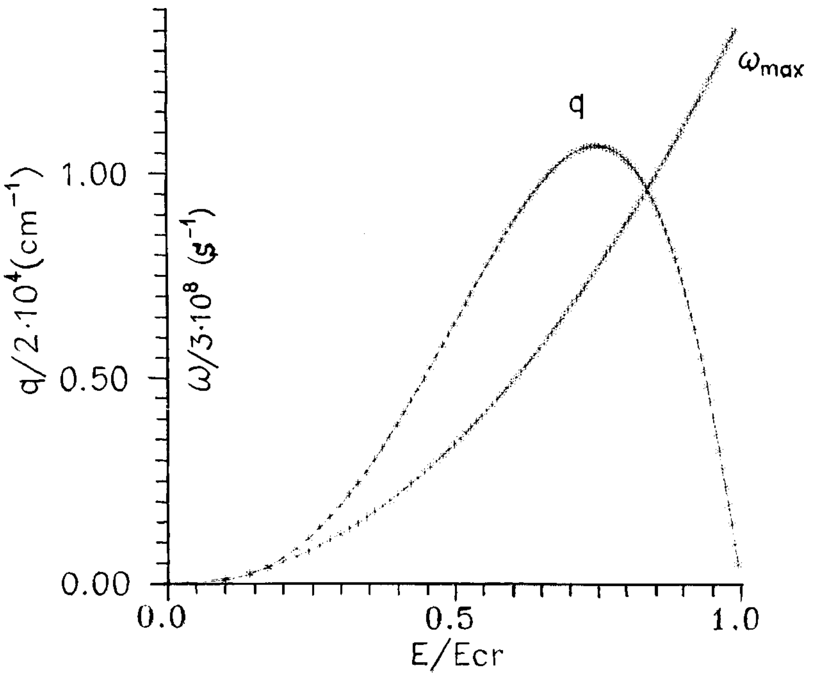

FIG. 2. Maximum value of q and $\omega_{\max}$ for the third region as a function of the electric-field intensity E.

Since Y_1 and Y_2 are positive and different and $k_i=\sqrt{Y_i-q^2}$, the regions of possible values of k_1 and k_2 will likewise be different. From the boundary conditions $\Phi_0(\omega,q,k_1)$ and $\Phi_0(\omega,q,-k_1)$ can be determined uniquely in terms of $\Phi_0(\omega,q,k_2)$ and $\Phi_0(\omega,q,-k_2)$, which are in turn determined by the initial conditions (length and radius of the current tube and the temperature at the moment of avalanche breakdown). The solutions obtained comprise two branches in the expansion in terms of z [with $\exp(ik_1z)$ and $\exp(ik_2z)$], and the coefficients in these parallel Fourier expansions are related to one another. To take account of the initial conditions it is necessary to switch from summation over ω and q to summation over k and q; ω will be a function of k and q. In so doing, to one term with k there corresponds a collection of terms—functions of q, taken with the corresponding weighting factors $\exp(\omega t)$. On this basis it can be expected that the contribution of the terms with the same values of k and different values of q to the complete solution will change with time, and static nonuniform strain and temperature fields will arise. Naturally, without determining the expansion coefficients from the initial conditions it is difficult to relate the sizes of the experimentally observed ring-shaped structure[6] to the characteristics of silicon; they can only be estimated. It is known from experiment that the minimum radius of the ring-shaped structure is $r_{\min}\simeq 3\times 10^{-3}$ cm, whence it follows that the maximum value of q is $q_{\max}\approx 3.83/r_{\min}\simeq 1.3\times 10^3$cm. According to Fig. 2, reasonable values of ω and E correspond to this value.

It should be noted that the nonuniformity of the strain and temperature fields in this case encompasses the entire region of the near-surface space charge, though it can be observed visually on the surface, and since α' appears in the boundary conditions, the external conditions (illumination, ultrasonic irradiation) can be expected to influence the formation of the structures considered.

[1] I. Prigogine and G. Nicolis, *Exploring Complexity* (W. H. Freeman, San Francisco, 1989; Russian translation, Mir, Moscow, 1990).

[2] V. I. Emel'yanov and I. F. Uvarova, Izv. Akad. Nauk SSSR, Ser. Fiz. **50**, 1214 (1986).

[3] I. O. Efimov, A. G. Krivenko, and V. A. Benderskiĭ, Élektrokhimiya **25**, 1587 (1989).

[4] V. I. Emel'yanov and A. A. Sumbatov, Poverkhnost' **7**, 122 (1988).

[5] A. V. Prokaznikov, S. F. Maslenitsyn, A. A. Svyatchenko, and S. T. Pavlov, Solid State Commun. **90**, 217 (1994).

[6] A. V. Prokaznikov, N. E. Mokrousov, A. L. Vinke, and S. T. Pavlov, Phys. Low-Dim. Struct. **2**, 87 (1994).

[7] E. Scholl, *Nonequilibrium Phase Transitions in Semiconductors* (Springer, New York, 1987; Russian translation, Mir, Moscow, 1991).

[8] V. V. Gafaĭchuk, B. I. Datsko, B. S. Kerner, and V. V. Osipov, Fiz. Tekh. Poluprovodn. **24**, 1282 (1990) [Sov. Phys. Semicond. **24**, 806 (1990)].

[9] L. D. Landau and E. M. Lifshitz, *Theory of Elasticity* (Pergamon Press, N. Y.; Russian original, Nauka, Moscow, 1965).

[10] S. M. Sze, *Physics of Semiconductor Devices* (Wiley, New York; Russian original, Energiya, Moscow, 1973).

Translated by M. E. Alferieff

Role of the pinch effect in a high-velocity metallic contact with a high current

É. M. Drobyshevskiĭ, B. G. Zhukov, R. O. Kurakin, S. I. Rozov, M. V. Beloborodyĭ,
and V. G. Latypov

A. F. Ioffe Physicotechnical Institute, Russian Academy of Sciences, 194021 St. Petersburg, Russia

(Submitted August 18, 1998)
Pis'ma Zh. Tekh. Fiz. **25**, 89–94 (March 26, 1999)

Experimental evidence is presented in support of the hypothesis that the main factor determining the flow of physical processes on the interface of a sliding solid-state contact carrying a $\sim 0.1-1$ MA/cm^2 current is the sausage-type MHD pinch instability. It leads to the appearance and explosive destruction of tightening (quasi) liquid constrictions connecting the contact surfaces, so that under magnetic-suspension conditions the sliding of the latter relative to one another is virtually contact-free on the greater portion of their area. © *1999 American Institute of Physics.* [S1063-7850(99)03203-6]

The electromagnetic acceleration of electrically conducting bodies (armatures) in a Reltron is limited by the transition of a sliding solid-state contact (SSC) into an arc regime at $V \sim 1$ km/s.[1] It is believed that here the destruction of the SSC is due to melting of the armature surface followed by removal by the rails of the melt attached to them, which produces a gap in the SSC. The following basic reasons for the melting of the surface have been considered thus far: 1) local energy release as a result of current concentration in small zones where the best contact occurs (*a* spots),[2] 2) dry friction,[3] and 3) the velocity skin effect (VSE).[4] On account of the finite rate of the penetration of the magnetic field into the rails and armature, as the armature velocity increases, the velocity skin effect concentrates the current toward the back edge of the armature, causing melting of the armature and removal of the melt from this location. As a result, a wave of melting propagates along the contact surface toward the front edge of the armature, ultimately destroying the SSC.

The experiment described below shows that a much more efficient mechanism leading to the destruction of the SSC than the mechanisms named above operates in Reltron acceleration of bodies. This mechanism, the pinch effect, is due to the three-dimensionality of real configurations and the nature of the ampere forces employed for electromagnetic acceleration (we note that friction can be treated one-dimensionally, the *a* spots can be treated in the one- or two-dimensional approximation, and the VSE is ordinarily investigated in the planar approximation).

To reveal the effect experimentally in its purest form we employed a very simple armature in the form of an aluminum cube with $d_0 = 1$ cm. The cube was accelerated from a state of rest in the gap between two rails with a *T*-shaped cross section. Plexiglass, 12 mm thick, was present between the back side of the 28 mm wide rails secured by steel plates. The current increased to $I = 550$ kA in $\sim 25\ \mu$s and remained almost constant for the next 150 μs. We note as a point of reference that the thickness of the skin layer $l \approx (\tau/\pi\mu_0\sigma)^{1/2}$ over $\tau = 25\ \mu$s will be $l_{\mathrm{Al}} \approx 0.6$ mm $\ll d_0$ in Al ($\sigma = 1.17 \cdot 10^7$ mho/m at $t = 300\,^\circ$C) and $l_{\mathrm{Cu}} \approx 0.5$ mm in Cu ($\sigma = 2.8 \cdot 10^7$ mho/m at $t = 300\,^\circ$C). Then the magnetic pressure acting on the face of a linear conductor with a square cross section with $d = 1$ cm and $I = 550$ kA will reach $p_B = B^2/2\mu_0 \approx 200$ MPa, and for $d = d_0 - 2l_{\mathrm{Al}} \approx 8$ mm $p_B \approx 240$ MPa. Some of the skin layer then melts. The force accelerating the cube in a Reltron is $F = L' I^2/2 \approx 30$ kN (here $L' \approx 0.25\mu$H/m is the inductance per unit length of the rails), so that in 150 μs it should acquire a velocity $V \approx 1.7$ km/s over a 13 cm path. Initially, it moves over a distance $d \approx 1$ cm in $\sim 50\ \mu$s.

In this case the phase of the displacement of the armature from the rest position, when the velocity is still low, is of diagnostic value, important for understanding processes in SSCs. Here we call attention to two basic features, which are immediately evident on examining the rails (Fig. 1). First, nearly square impressions from the cube to a depth $\Delta \approx 300\ \mu$m are present at the locations of initial contact on both rails. Second, two converging surface tracks, outside of which indications of melting of copper can be seen in the rails, emerge from the corners of the back edge of the impression at an angle of $42 \pm 2°$ with respect to the generatrices of the rails. Rounded depressions are present at the locations where these tracks converge. On one electrode the convergence still occurred within the impression made by the cube, near its front edge, and the diameter of the depression is ~ 2.5 mm. On the other electrode the convergence occurs in ~ 12–15 mm outside the front edge of the track of the cube, but the depressions (there are two of them) are ≈ 0.6–0.8 mm in diameter and they are located ~ 7–8 nm behind the front edge of the cube track. Outside the cube track, downwards in the direction of motion of the cube, the entire surface of the electrodes shows numerous indications of melting and erosion of the copper.

Let us try to understand the reasons for the apperance of the two features described above. The impression on both rails can be attributed only to the pinch effect, i.e., an axial expansion of the cube as a result of the compression of its side faces by the magnetic pressure p_B. The latter was more than five times greater than the yield stress in Al $\sigma_{0.2} \approx 30$ MPa. This is also supported by a comparison of the depth of the impression in the surface of a rail due to the static pres-

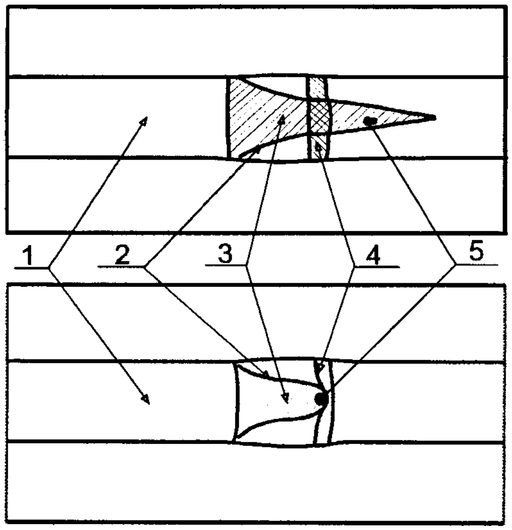

FIG. 1. Schematic diagram of the tracks left on copper rails by an Al cube accelerated between them by ponderomotive forces: 1 — Working surface of the *T*-shaped rails; 2 — converging tracks; 3 — erosion-free zone; 4 — front edge of the impression; 5 — depression.

sure of the cube with the observed values of Δ (Fig. 2) (it makes sense to compare with static experiments because the distance traversed by sound in copper in the time the cube moves from its initial position is much greater than the thickness of a rail). The force press the cube into the rail to depth $\Delta \approx 300\,\mu$m corresponds precisely to the pressure ≈ 200 MPa. On this basis it also follows that there is no particular point to using a *C*-shaped armature, which is often employed to provide the best contact due to the magnetic pressure pressing its ''tails'' to the rails,[1] since the magnetic pressure, as we can see, presses the armature to the rails anyway because of the isotropic deformation of its material.

The effect of the magnetic pressure (the pinch effect) also explains the origin of the converging tracks on the contact surfaces of the rails. The point is that on the armature–rails contact surfaces there is no resistance to shear due to the strength of the material. As is well known,[5] one of the characteristic MHD instabilities typical of easily deformable current-carrrying conductors is the sausage instability. It is due to the increase in p_B as the radius of the conductor decreases $(p_B \sim r^{-2})$.

The weakest point in this sense is the point of contact of the surfaces of the armature and a rail. Here a thin (heated) layer of the armature is progressively compressed by the magnetic field, sliding along the surface of the rail, so that ultimately the armature–rail contact occurs through a thin metallic neck. The displacement of the bridge along the rail under the action of the force F together with the thinning of the neck produce the converging tracks observed on the rails. It turns out that for a substantial time the armature moves along the rails on a ''magnetic cushion,'' while the current flows not through the entire initial contact surface (or its extended peripheral part, bearing in mind the skin effect), but rather through a relatively thin (and becoming continuously thinner) neck. Ultimately the neck explodes, producing a depression in the rail. The current is interrupted and a metallic contact is once again restored on the greater area on account of the elastic expansion of the armature and rail materials. This process repeats right up to establishment of a completely arc regime, for example, as a result of a decrease in the armature dimensions because of erosion.

We note two circumstances: 1) It is obvious that the time-averaged resistance of such a contact with necks should be appreciably greater than the resistance of an ideal continuous surface contact and 2) the change in the properties of a real contact (appearance and development of necks, fluctuations of the resistance, and so on) should be modulated by the elastic oscillations of the system, primarily, the armature. These conclusions remove the dilemma stated by R. Marshall,[1] the doyen of Reltron acceleration, concerning the fact that the voltage and its fluctuations on a real contact are almost two times greater than for a uniform metallic contact at the stage when the rails still do not show traces of a developed arc regime. He also noted that the physics of the phenomena on the contact surfaces in Reltrons is still not understood.

The results presented above show why the earlier theoretical ideas about the reasons for the transition of the SSC

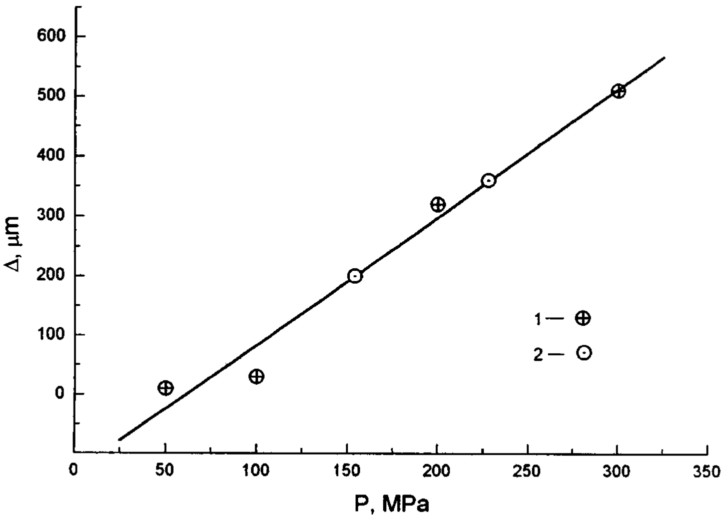

FIG. 2. Size Δ of the impression in the rails versus the static pressure P acting on the Al cube being pressed in — $\oplus$; initial impressions produced in the rails during electromagnetic acceleration of a cube — $\odot$.

into the arc regime are inadequate. It turns out that it is important to take account of the effects due to the third dimension (transverse relative to the Reltron channel and the flowing current). Doing so greatly increases our understanding of the processes occurring on contact surfaces, leading to catastrophic erosion of these surfaces and destruction of the SSC. It could be that the suppression, in one way or another, of the sausage MHD instability in the SSC zone will make it possible to increase substantially the velocity at which the SSC still operates reliably.

This work was supported by a CRDF grant RE2-138.

[1] R. A. Marshall, IEEE Trans. Magn. **31**, 209 (1995).

[2] R. Holm, *Electric Contacts, Theory and Application* (Springer-Verlag, N. Y., 1967).

[3] B. A. Uryukov, A. D. Lebedev, and K. K. Milyaev, in *Proceedings of the 2nd All-Union Seminar on the Dynamics of a High-Current Discharge in a Magnetic Field*, Novosibirsk, 1991, pp. 33–71.

[4] P. B. Parks, J. Appl. Phys. **67**, 3511 (1990).

[5] B. P. Peregud, ''Magnetohydrodynamic instabilities of condensed current-carrying conductors'' (Doctoral Dissertation, Leningrad, 1981).

Translated by M. E. Alferieff